Astronomy Letters, Vol. 31, No. 1, 2005, pp. 1–6. Translated from Pis'ma v Astronomicheskiĭ Zhurnal, Vol. 31, No. 1, 2005, pp. 3–9.

Influence of Cosmological Expansion on the Threshold Effects in the Annihilation Reaction of Hard Photons with CMB Photons

Yu. S. Grishkan[1,2*] and A. A. Pershin[2]

[1] *Institute for Nuclear Research, Russian Academy of Sciences, pr. Shestidesyatiletiya Oktyabrya 7a, Moscow, 117312 Russia*

[2] *Rostov State University, Rostov, Russia*

Received May 31, 2004

Abstract—The redshift (z) dependence of the dispersion relations for free particles is analyzed by taking into account the Lorentz invariance violation. A nonlinear algebraic equation is derived for the momenta of the particles involved in the annihilation reaction of a hard photon from a γ-ray source with a soft cosmic microwave background (CMB) photon near the threshold of this reaction. The solutions of this threshold equation are constructed and analyzed as a function of the redshift. We show that the threshold of the reaction under consideration tends to decrease with increasing z; the energy spectra of γ-ray sources at energies of $\sim$10 TeV must be cut off in accordance with the calculated z dependence. We also calculate the time delay of the light signals from γ-ray sources that corresponds to the Lorentz invariance violation for photons. We discuss the possibility of improving the standard constraints on the Lorentz invariance violation parameters for fields of various physical natures. © *2005 Pleiades Publishing, Inc.*

Key words: *theoretical and observational cosmology, γ-ray bursts, blazars, Lorentz invariance violation.*

INTRODUCTION

In recent years, the hypotheses that the Lorentz invariance, the LI symmetry in particle physics, is approximate and may be violated at high energies $E_0 \sim 10$ TeV in the center-of-mass frame have been suggested and widely discussed (Coleman and Glashow 1999; Amelino-Camelia and Piran 2001). These hypotheses are based mainly on astronomical observations: the γ-ray emission from blazars and nebulae and the cosmic-ray spectrum at very high energies. The hypothesis of LI violation allows such phenomena as the absence of the Greisen–Zatsepin–Kuzmin cutoff (Greisen 1996; Zatsepin and Kuzmin 1966) in the cosmic-ray spectrum at energies $E_0 \geq 10^{19}$ eV (Tanimori *et al.* 1998) and the observations of 20-TeV photons in the spectra of certain Markarian galaxies (Aharonian *et al.* 1999; Aharonian and Coppi 1999) to be linked. As was pointed out in these works, photons with energies of up to 17 and 24 TeV were detected from the blazars MK 421 ($z = 0.031$, $l = 143$ Mpc) and MK 501 ($z = 0.034$, $l = 157$ Mpc), respectively. In contrast, in the standard field theory with exact Lorentz invariance, a cutoff at energies above E_0 should be observed in the spectra of γ-ray sources due to the interaction of hard γ rays with cosmic microwave background (CMB) photons (Steker *et al.* 1992). There are also other astronomical observations that could be interpreted in terms of the LI-violation hypothesis (Biller *et al.* 1999). Recently, the HEGRA collaboration reported the discovery of a new generation of blazars (Aharonian *et al.* 2002, 2003) among which the object H1426+428 with a significant redshift ($z = 0.129$) stands out. According to the cited papers, the cutoff in the γ-ray spectrum of this object occurs at about 12 TeV. These data may be indicative of a change in the threshold energies in the spectra of BL Lac objects with their redshift.

There is also another group of objects with which the hopes for gathering such information could be associated. Cosmological γ-ray bursts are potential suppliers of data on the absorption of γ-ray emission from distant sources. Indeed, we know reports on the observation of emission from γ-ray bursts in the high-energy spectral range from 100 MeV to 18 GeV based on EGRET data (Dingus *et al.* 1998) and in the range 1–10 TeV based on MILAGRO data (Atkins *et al.* 2000, 2004). Here, we focus our attention on the implications for the boundary of the hard spectrum of distant cosmological objects associated with the LI-violation hypothesis where the influence of the expansion of the Universe on the physical processes in it cannot be ignored.

*E-mail: ugrish@yandex.ru

1063-7737/05/3101-0001$26.00

DISPERSION RELATIONS FOR PARTICLES IN THE THEORY WITH VIOLATED LORENTZ INVARIANCE

According to one hypothesis, the LI-symmetry violation may be related to the effect of the space-time foam of quantum fluctuations on the free particles that propagate in space-time. Quantum fluctuations modify their dispersion relations, which take the form (Coleman and Glashow 1999; Steker and Glashow 2001; Amelino-Camelia 2002)

$$E^2(p) = p^2 + m^2 + (\eta p^n)/M_g^{n-2}, \qquad (1)$$

where $p = |\mathbf{p}|$ is the magnitude of the particle momentum, M_g is the Planck mass scale, and η is a dimensionless numerical parameter.

Below, we use a rational system of units with $\hbar = c = 1$. The dimensionless constant η in the third term of the dispersion relation (1) determines the low-energy violation threshold of the dispersion relation for free particles. The unknown integer parameter n, along with the fundamental constant M_g, determines the momentum range in which the quantum effects for particles of a given type are significant. Clearly, modifying the dispersion relation using the Planck parameters must lead to a dependence of the speed of light in space-time as it propagates from the source to the observer on the parameters η, n, and M_g. This dependence can be established when high-energy (hard γ-ray) photons propagate to cosmological distances, since it leads to nonsimultaneous reception of the signals from the same source (Ellis *et al.* 2000). In addition, when the Planck terms become equal to the Lorentz terms in order of magnitude, the energy thresholds of the reactions with elementary particles can shift and new threshold effects can appear in the energy ranges that are generally forbidden for a given reaction (Jacobson *et al.* 2002).

THRESHOLD ENERGY RELATIONS FOR THE PHOTON ANNIHILATION REACTION TO PRODUCE AN ELECTRON–POSITRON PAIR

As the γ-ray emission from an object propagates to large distances, a high-energy photon must interact with an infrared (IR) photon of the CMB radiation in the reaction

$$\gamma + \gamma_{\rm IR} = e^+ + e^-. \qquad (2)$$

In the standard theory with exact LI symmetry at IR photon energy ε and electron mass m, this reaction has the threshold $k_{\rm th0} = m^2/\varepsilon$. In the theory with violated LI symmetry in flat space-time, this threshold rises (Jacobson *et al.* 2002). Let us analyze the propagation of the emission from sources in an expanding Universe to the observer. In this case, the scale factor of the Universe depends on redshift z, while the linear scale changes during the cosmological expansion as $l \sim a \sim (1+z)^{-1}$. The photon wave number at early expansion phases is $k' = k(1+z)$, and the photon energy is $\omega' = \omega(1+z)$. The momentum and energy variables in the dispersion relations for free massive particles (below, we discard the prime on the modified energy and momentum variables) are modified in a similar way and take the form

$$E^2(1+z)^2 = p^2(1+z)^2 + m^2 + \eta p^n (1+z)^n / M_g^{n-2}. \qquad (3)$$

We see from Eq. (3) that when the linear scales change simultaneously and when the energy scales m and M_g are constant, the Lorentz invariance violation threshold depends on z as the momentum p increases. Consequently, the thresholds of the reactions with elementary particles also depend on z. Thus, the following dispersion relations are valid for the photon, the electron, and the positron in reaction (2):

$$\omega^2(k) = k^2 + \xi k^n / M_{gz}^{n-2}, \qquad (4)$$

$$E^2(p) = p^2 + m_z^2 + \eta p^n / M_{gz}^{n-2}, \qquad (5)$$

$$E^2(q) = q^2 + m_z^2 + \eta p^n / M_{gz}^{n-2}, \qquad (6)$$

where $m_z = m/(1+z)$; $M_{gz} = M_g/(1+z)$; η and ξ are dimensionless numerical parameters; k, p, q are the magnitudes of the particle momenta; and $\omega(k), E(p), E(q)$ are the particle energies. We see from Eqs. (4)–(6) that the particle mass m_z and the Planck energy scale M_{gz} effectively decrease with increasing z and at fixed momenta k and p due to the cosmological expansion. Therefore, one might expect these parameters to depend on z in the momentum and energy relations that fix the typical threshold values of $k_{\rm th}, \omega_{\rm th}$ in the reactions with elementary particles. Consequently, observations of hard γ-ray sources in an expanding Universe can be used as a test for choosing η, ξ, and n. It is convenient to analyze the momentum relations for the reactions between particles in the metric of an expanding Universe,

$$ds^2 = a^2(\tau)(d\tau^2 - dl^2), \qquad (7)$$

in flat space-time by substituting the energy scales $m \to m_z$ and $M_g \to M_{gz}$ in the dispersion relations (4)–(6). The energy ε of the CMB IR photon $\gamma_{\rm IR}$ is negligible compared to the energy ω of the hard photon. Therefore, following Jacobson *et al.* (2003a), we first construct the vertex of the interaction $\gamma \to e^+e^-$ and then correct it for the CMB photon energy, thereby reproducing the balance energy relation

for reaction (2). The law of conservation of the 4-momentum $k_i = p_i + q_i$ (below, the Latin indices are $i = 0, 1, 2, 3$, and the Greek indices are $\alpha = 1, 2, 3$) must hold at the reaction vertex under consideration. The covariant law of conservation of energy–momentum at the vertex under consideration is

$$(p_i - k_i)(p^i - k^i) = q_i q^i. \quad (8)$$

Since the indices in metric (7) are raised by the metric tensor $g^{ik} \propto 1/a^2$, the law of conservation of energy–momentum in $(3+1)$-dimensional form follows from (8),

$$(E(p) - \omega(k))^2 - (p_\alpha - k_\alpha)^2 = q_0^2 - q_\alpha^2. \quad (9)$$

Combining (4)–(6) and (9) yields an equation that explicitly relates the particle energy and momenta at the vertex under consideration:

$$\frac{\xi k^n}{M_{gz}^{n-2}} + \frac{\eta p^n}{M_{gz}^{n-2}} + \frac{\eta q^n}{M_{gz}^{n-2}} = 2(E(p)\omega(k) - pk\cos\theta), \quad (10)$$

where θ is the angle between the vectors p and k. Near the threshold of the reaction with two particles being in its final ($|\text{out}\rangle$) state, the particle momenta are parallel if the function $E(p)$ is monotonic (Mattingly *et al.* 2003). Therefore, $\theta = 0$ and relation (10) takes the form

$$\frac{\xi k^n}{M_{gz}^{n-2}} + \frac{\eta p^n}{M_{gz}^{n-2}} - \frac{\eta q^n}{M_{gz}^{n-2}} = 2pk\left(\frac{E(p)}{p}\frac{\omega(k)}{k} - 1\right). \quad (11)$$

In the energy range for reaction (2) of interest, the particle momenta are relativistic, and the LI-violating terms are negligible:

$$m_z/p \ll 1,$$
$$\xi\,(k/M_{gz})^{n-2} \ll 1,$$
$$\eta\,(p/M_{gz})^{n-2} \ll 1.$$

Expanding (11) in terms of these parameters yields the threshold relation between the particle momenta at the reaction vertex

$$\frac{\xi k^n}{M_{gz}^{n-2}} + \frac{\eta p^n}{M_{gz}^{n-2}} - \frac{\eta q^n}{M_{gz}^{n-2}} = 2pk\left(\frac{m_{gz}^2 M_{gz}^{n-2}}{2p^2} + \frac{\xi k^{n-2}}{2} + \frac{\eta p^{n-2}}{2}\right). \quad (12)$$

Let us now take into account the fact that two photons, one of which is the soft CMB IR photon, are involved in the initial ($|\text{in}\rangle$) state of reaction (2). In this case, the threshold equation (12) changes only slightly. In a situation dynamically equivalent to (9), the initial momentum $k_{i,|\text{in}\rangle}$ of the hard γ-ray photon is

$$k_{i,|\text{in}\rangle} = (\omega + \varepsilon, k - \varepsilon, 0, 0) = (\omega_1, k_1),$$

where the energy of the soft photon $\varepsilon \ll \omega, k$. Expanding the frequency

$$\omega(k_1) = \omega(k_1 + \varepsilon) + \varepsilon$$

in a power series of ε/k_1, we can easily reduce the dispersion relation (4) for the hard photon to

$$\omega(k_1) = k_1 + \xi_1\left(\frac{{k_1}^{n-1}}{2M_{gz}^{n-2}}\right), \quad (13)$$

where

$$\xi_1 = \xi + \frac{4\varepsilon M_{gz}^{n-2}}{k_1^{n-1}}$$

is a new (shifted compared to ξ) constant; the shift of the ξ scale is proportional to the energy ε of the γ_{IR} photon. Therefore, to include the IR photon in the $|\text{in}\rangle$ state of the reaction under consideration, it will suffice to make the substitution of the momenta $k \Rightarrow k_1$ and the threshold constant of the hard γ-ray photon as $\xi \Rightarrow \xi_1$. In relation (12), it is assumed that $k_1 > p$. (Below, we omit the subscript 1 on the momentum variables and the constant ξ_1 for convenience.) To analyze the physical processes near the reaction threshold, it is convenient to introduce the dimensionless momentum variable $y = p/k$, whose value is limited above. Given the small shift of the threshold constant ξ in (13), Eq. (12) for the particle momenta can be rewritten as

$$\frac{M_{gz}^{n-2} m_z^2}{k^n} = \left(\xi + \frac{4\varepsilon M_{gz}^{n-2}}{k^{n-1}}\right) y(1-y) - \eta y(1-y)\left[y^{n-1} + (1-y)^{n-1}\right].$$

When the scale factor $1+z$ is explicitly separated out from the mass scales, the latter equation takes the form

$$\left[\frac{\xi k^n}{M_g^{n-2} m^2} + \frac{4\varepsilon k}{m^2(1+z)^{n-2}}\right] \times y(1-y) - \eta y(1-y) \times \left[y^{n-1} + (1-y)^{n-1}\right] \times \frac{k^n}{M_g^{n-2} m^2} - \frac{1}{(1+z)^n} = 0. \quad (14)$$

In this algebraic equation, it is convenient to introduce the dimensionless momentum of the hard photon $\beta = k\varepsilon/m^2$ and the new dimensionless threshold constants (see Jacobson *et al.* 2003b)

$$\tilde{\eta} = \frac{m^{2n-2}\eta}{M_g^{n-2}\varepsilon^n}, \quad \tilde{\xi} = \frac{m^{2n-2}\xi}{M_g^{n-2}\varepsilon^n}.$$

With these quantities, the threshold equation (14) takes a form convenient for an algebraic analysis:

$$G(\beta, y, z, n) = \alpha_n(y)\beta^n + \gamma_n(y, z)\beta - (1+z)^{-n} = 0, \quad (15)$$

where we use the notation

$$\alpha_n(y) = y(1-y)\left\{\tilde{\xi} - \tilde{\eta}\left[y^{n-1} + (1-y)^{n-1}\right]\right\},$$

$$\gamma_n(y, z) = 4y(1-y)/(1+z)^{n-2}.$$

The case of $n = 3$, which can be directly derived, for example, from the equations of the generalized string σ-model for massless and low-mass particles (Ellis *et al.* 2002a) and in the five-dimensional effective quantum theory of gauge fields (Myers and Pospelov 2003), is most commonly invoked to explain the absence of threshold effects in the spectra of blazars at $k_{\text{th0}} \sim 10$ TeV. In this case, Eq. (15) takes the form

$$G(\beta, y, z, 3) = y(1-y)\beta^3 \quad (16)$$
$$\times \left\{\tilde{\xi} - \tilde{\eta}\left[y^2 + (1-y)^2\right]\right\}$$
$$+ \frac{4\beta}{1+z}y(1-y) - (1+z)^{-3} = 0.$$

Let us introduce the new momentum variable $w = (2y-1)^2$. This variable $w = 0$ when the magnitudes of the momenta of the escaping particles in the $|\text{out}\rangle$ state are numerically equal ($y = 1/2$). Using it, we can easily separate this symmetric case of particle production near the threshold of reaction (2) from the asymmetric case where the particle momenta differ ($y \neq 1/2$). Equation (16) transforms to

$$G(\beta, w, z, 3) = \frac{\beta^3}{4} \quad (17)$$
$$\times \left\{\left[\tilde{\xi} + \frac{4}{\beta^2(1+z)}\right](1-w) - \frac{\tilde{\eta}(1-w^2)}{2}\right\}$$
$$\times -(1+z)^{-3} = 0.$$

If the reaction under consideration has the symmetric threshold $w = 0$, then the relation for the dimensionless momenta of hard photons near the threshold of reaction (2) follows from (17):

$$\beta = (1+z)^{-2} + \frac{(\eta - 2\xi)\beta^3(1+z)}{8}. \quad (18)$$

Reaction (2) for nonviolated LI symmetry and $z = 0$ reaches its threshold at the hard-photon momenta $k_{\text{th0}} = m^2/\varepsilon$.

At the energy of the IR photon $\varepsilon = 0.025$ (a wavelength $\lambda \sim 50$ μm), the high-energy photons with $k_{\text{th0}} \sim \omega_{\text{th0}} \sim 10$ TeV that interact with it must be completely absorbed. However, this threshold is absent in the spectra of known blazars. Therefore, let us attempt to relate the scale k_{th0} to the possible LI-violation scale $k_{\text{th0}} \simeq k_{\text{LI}}$ and to study the implications of this assumption. Since the correction to the dispersion relation for a free photon is (see (4) and (13))

$$\frac{\Delta\omega(k)}{k} \sim \xi\left(\frac{k}{M_{gz}}\right)^{n-2} \ll 1,$$

substituting (4) in the left-hand side of Eq. (18) yields the ratio of the photon energy ω_{th} to the threshold energy ω_{th0} of the theory with nonviolated LI symmetry. We normalize the nonlinear expression (18) to the assumed momentum near the LI-violation threshold $k_{\text{th0}} = 10$ TeV. With the mass scales $M_g \sim 10^{19}$ GeV and $m \sim 0.5$ MeV, this yields

$$\frac{\omega_{\text{th}}}{\omega_{\text{th0}}} = (1+z)^{-2} + \frac{(\eta - 2\xi)}{20}\left(\frac{k}{k_{\text{th0}}}\right)^3(1+z). \quad (19)$$

In addition to the symmetric solution considered above, Eq. (17) also has an antisymmetric solution for the particle momenta near the threshold of reaction (2):

$$\eta\omega_a = \frac{4}{\beta^2(1+z)},$$

$$\beta = \frac{\left(\tilde{\eta} - \tilde{\xi}\right)\beta^3(1+z)}{4} + \frac{1}{4}\sqrt{-\frac{\eta}{(1+z)}\beta^3}.$$

The latter can be rewritten in a form similar to (19):

$$\frac{\omega_{\text{th}}}{\omega_{\text{th0}}} = \frac{(\eta - \xi)}{10}\left(\frac{k}{k_{\text{th0}}}\right)^3(1+z) \quad (20)$$
$$+ \sqrt{-\frac{\eta}{5(1+z)}\left(\frac{k}{k_{\text{th0}}}\right)^3}.$$

For $z \to 0$, relations (19) and (20) transform into the formulas from the paper of Jacobson *et al.* (2002). An analysis of polynomial (17) indicates that the symmetric threshold is reached at

$$\tilde{\xi} > -\frac{4}{\beta^2(1+z)}, \quad \beta < \frac{1.5}{(1+z)^2},$$

while the asymmetric threshold is reached for the inverse inequalities. Choosing the parameters η, ξ, and z in (19) and (20), we can make the lower threshold ω_{th} of reaction (2) lie above or below the threshold ω_{th0} in the theory with nonviolated Lorentz invariance. This combination of parameters proves to be nontrivial, because the threshold equation (17) is nonlinear. We see from (19) and (20) that the following quantity is a measure of the LI violation effect at high redshifts and high energies of hard photons:

$$R = \left(\frac{k}{k_{\text{th0}}}\right)^3(1+z).$$

This form of the expression for R stems from the quantum fluctuations of the geometry included in the phenomenological dispersion relation (4) increasing with k and z. Recent studies (Steker 2003a, 2003b; Jacobson *et al.* 2003c, 2003d) have shown that the polarization data and the spectrum fitting for known blazars probably impose stringent constraints on the parameters of the theory mentioned above: $|\eta| < 10^{-15}$, $-10^{-7} < \xi < 10^{-2}$. Summing up these constraints and the existence conditions for the threshold solutions (19) and (20) given above, we can note that the symmetric solution at energies above 10 TeV is realized at

$$0 < \frac{k}{k_{\rm th0}} < \frac{1.5}{(1+z)^2}.$$

The asymmetric LI violation threshold shifts to the range of energies of the order of several PeV and is currently inaccessible to observation. Therefore, the LI violation hypothesis can be tested by studying the spectra of γ-ray sources at photon energies $\omega_k \sim 10$ TeV. In this case, the z dependence of the threshold energy for reaction (2), to small terms of order $k/(10k_{\rm th0})$, is given by

$$\frac{\omega_{\rm th}}{\omega_{\rm th0}} \simeq \frac{1}{(1+z)^2}. \qquad (21)$$

It follows from (15) and (16) that this result remains valid for $k/k_{\rm th0} \to 0$, irrespective of n.

The z dependence of the absorption of emission in the annihilation reaction of hard photons with CMB photons was previously calculated, for example, by Steker *et al.* (1992). Steker (2003b) compared these calculations with the EGRET data for several known blazars extrapolated to energies of the order of several TeV and concluded that there is a significant discrepancy between the calculations and the experimental data. This conclusion leaves a freedom for theoretically interpreting the above effect.

The LI violation hypothesis suggests that the photons are quasi-particles with the nonlinear dispersion relation (4). The threshold effect must then be observed in the spectrum of the photons coming to the observer, while the spectra of cosmological radiation sources must be cut off at high energies with the characteristic z dependence (21). Note that this result is obtained with the currently known constraints on the LI violation parameters η and ξ.

DELAY OF THE SIGNALS FROM EXTRAGALACTIC GAMMA-RAY SOURCES

The signals of different energies from extragalactic sources that propagate in space with the nonlinear dispersion law (4) must reach the observer in different times. The time delay of the signal from an emitting source that arises from the path difference between the photons with velocities 1 and $1 - \Delta u$ is

$$\Delta t = \int_t^{t_0} \Delta u(\omega) dt.$$

It follows from the dispersion relationship (4) that this delay can be large for distant high-energy radiation sources, primarily for γ-ray bursts. Indeed, this dispersion relation yields the expression for the correction to the phase velocity of the light signal

$$\Delta u = \frac{n-2}{2}|\xi|\frac{\Delta\omega_\gamma}{\omega}\left(\frac{\omega}{M_{gz}}\right)^{n-2}, \qquad (22)$$

where $\Delta\omega_\gamma$ is the energy difference between the photons from two different energy channels in the detector.

Let Ω_Λ and Ω_m be the cosmological parameters that are the ratios of the vacuum energy and matter densities to the critical density, respectively, and H_0 be the Hubble constant. The delay of the emission from a distant cosmological source in the Universe (7) due to quantum-gravitational effects is given by (Vertogradova *et al.* 2003)

$$\Delta t = \frac{1}{H_0}\int_1^{z+1} \frac{\Delta u dx}{x\sqrt{\Omega_m x^3 + \Omega_\Lambda}}.$$

Given (22), the latter equation can be rewritten in explicit form:

$$\frac{\Delta t}{\Delta\omega_\gamma} = \frac{n-2}{2}\frac{|\xi|}{H_0 M_g^{n-2}}\int_1^{z+1} \frac{(x\omega)^{n-3}\,dx}{\sqrt{[\Omega_m x^3 + \Omega_\Lambda]}}. \qquad (23)$$

At $n = 3$, relation (23) matches the formula derived and analyzed by Vertogradova *et al.* (2003), to the factor $|\xi|/2$, and yields at $z \ll 1$

$$\frac{\Delta t}{\Delta\omega_\gamma} = \frac{|\xi|}{2H_0 M_g\sqrt{\Omega_\Lambda}}z.$$

A recent wavelet-based statistical analysis of the delay of the signals from γ-ray bursts qualitatively confirms this dependence for bursts with energies $\leq$0.2 MeV (Ellis *et al.* 2002b). This trend is probably also preserved for higher-energy γ-ray bursts (up to energies of $\sim$15 MeV), as suggested by the analysis of IPN (InterPlanet Network) data on the GRB 021206 (Boggs *et al.* 2003).

CONCLUSIONS

The most recent observations of new blazars with relatively high redshifts $z \sim 0.1$ for these objects (Aharonian *et al.* 2002, 2003) show that the energy at

which their γ-ray spectrum is cut off tends to decrease with increasing z, which is in qualitative agreement with the above conclusions (see (21)). However, a firm conclusion as to whether information about the LI violation at photon energies $\omega \sim 10$ TeV can be extracted from these observations can be reached only by analyzing a representative statistical sample of spectra for γ-ray sources at these energies. A parallel study of the delay of the emission from these objects would allow more stringent constraints to be imposed on the parameters η, ξ, and M_g. Only this comprehensive testing of the LI violation hypothesis will lead us to a firm conclusion about the validity of the underlying assumptions.

ACKNOWLEDGMENTS

This paper was supported by the Russian Foundation for Basic Research (no. 00-02-16096) and the Integration program (project nos. I0586 and F055). We wish to thank V.B. Petkov for his attention to this work and discussion of the results. We are also grateful to participants of the workshop at the Baksansk Neutrino Observatory (Nuclear Research Institute, Russian Academy of Sciences) for discussion of this work and their valuable remarks.

REFERENCES

1. F. A. Aharonian, A. G. Akhperjanian, J. A. Barrio, *et al.*, Astron. Astrophys. **349**, 11 (1999).
2. F. A. Aharonian, A. G. Akhperjian, J. A. Barrio, *et al.*, astro-ph/0202072 (2002).
3. F. A. Aharonian, A. G. Akhperjian, B. Beilike, *et al.*, astro-ph/0305275 (2003).
4. F. A. Aharonian and P. S. Coppi, Astropart. Phys. **11**, 35 (1999).
5. G. Amelino-Camelia, gr-qc/0204051 (2002).
6. G. Amelino-Camelia and T. Piran, Phys. Rev. D **64**, 036005 (2001).
7. R. Atkins, W. Benbow, D. Berley, *et al.*, astro-ph/0001111 (2000).
8. R. Atkins, W. Benbow, D. Berley, *et al.*, astro-ph/0403097 (2004).
9. S. D. Biller, A. S. Breslin, J. Buckley, *et al.*, Phys. Rev. Lett. **83**, 2108 (1999).
10. S. E. Boggs, C. B. Wunderer, K. Hurley, *et al.*, astro-ph/0310307 (2003).
11. S. Coleman and S. L. Glashow, Phys. Rev. D **59**, 116008 (1999).
12. B. L. Dingus, J. R. Catelli, and E. J. Schneid, AIP Conf. Proc. **428**, 349 (1998).
13. J. Ellis, K. Farakos, N. E. Mavromatos, *et al.*, Astrophys. J. **535**, 139 (2000).
14. J. Ellis, E. Gravanos, and N. E. Mavromatos, gr-qc/0209108 (2002a).
15. J. Ellis, N. E. Mavromatos, and D. V. Nonopoulos, astro-ph/0210124 (2002b).
16. K. Greisen, Phys. Lett. **16**, 748 (1996).
17. T. Jacobson, S. Liberatty, and D. Mattingly, Phys. Rev. D **66**, 081302 (2002).
18. T. Jacobson, S. Liberatty, and D. Mattingly, gr-qc/0303001 (2003a).
19. T. Jacobson, S. Liberatty, and D. Mattingly, hep-ph/0209264 (2003b).
20. T. Jacobson, S. Liberatty, D. Mattingly, and F. W. Steker, astro-ph/0309681 (2003c).
21. T. Jacobson, S. Liberatty, and D. Mattingly, Nature **424**, 1019 (2003d).
22. D. Mattingly, T. Jacobson, and S. Liberatty, Phys. Rev. D **67**, 124 012 (2003).
23. R. C. Myers and M. Pospelov, Phys. Rev. Lett. **90**, 211601 (2003).
24. F. W. Steker, astro-ph/0304527 (2003a).
25. F. W. Steker, astro-ph/0309027 (2003b).
26. F. W. Steker and S. L. Glashow, Astropart. Phys. **16**, 97 (2001).
27. F. W. Steker, O. C. De Jager, and M. H. Solomon, Astrophys. J. Lett. **390**, L49 (1992).
28. T. Tanimori, Y. Hayami, and S. Kamei, Astrophys. J. Lett. **492**, L33 (1998).
29. E. G. Vertogradova, Yu. S. Grishkan, and V. B. Petkov, Pis'ma Astron. Zh. **29**, 83 (2003) [Astron. Lett. **29**, 65 (2003)].
30. G. T. Zatsepin and V. A. Kuz'min, Pis'ma Zh. Éksp. Teor. Fiz. **4**, 114 (1966) [JETP Lett. **4**, 78 (1966)].

Translated by V. Astakhov

Astronomy Letters, Vol. 31, No. 1, 2005, pp. 15–29. Translated from Pis'ma v Astronomicheskiĭ Zhurnal, Vol. 31, No. 1, 2005, pp. 17–32.

Bending Instability of Stellar Disks: The Stabilizing Effect of a Compact Bulge

N. Ya. Sotnikova* **and S. A. Rodionov**

Astronomical Institute, St. Petersburg State University, Universitetskiĭ pr. 28, Petrodvorets, St. Petersburg, 198904 Russia

Received January 19, 2004

Abstract—The saturation conditions for bending modes in inhomogeneous thin stellar disks that follow from an analysis of the dispersion relation are compared with those derived from N-body simulations. In the central regions of inhomogeneous disks, the reserve of disk strength against the growth of bending instability is smaller than that for a homogeneous layer. The spheroidal component (a dark halo, a bulge) is shown to have a stabilizing effect. The latter turns out to depend not only on the total mass of the spherical component, but also on the degree of mass concentration toward the center. We conclude that the presence of a compact (not necessarily massive) bulge in spiral galaxies may prove to be enough to suppress the bending perturbations that increase the disk thickness. This conclusion is corroborated by our N-body simulations in which we simulated the evolution of near-equilibrium, but unstable finite-thickness disks in the presence of spheroidal components. The final disk thickness at the same total mass of the spherical component (dark halo + bulge) was found to be much smaller than that in the simulations where a concentrated bulge is present. © *2005 Pleiades Publishing, Inc.*

Key words: *galaxies, stellar disks, bending instabilities.*

INTRODUCTION

A peculiarity of the disks in spiral galaxies is that these are rather thin objects. Their thickness is several times smaller than the radial scale length. How far stars can go from the principal galactic plane due to their vertical random velocity component determines the disk thickness at fixed star surface density. The larger the velocity dispersion, the thicker the disk. The random velocities of young stars are known to be low, but the stellar ensemble can subsequently heat up through various relaxation processes; i.e., the random velocity dispersion can increase. Thus, the stellar disk thickness depends on how effective the relaxation processes are in galaxies, and it is ultimately determined by the factors that suppress or trigger the various heating mechanisms. Three basic stellar disk heating mechanisms are commonly discussed in the literature: the scattering of stars by giant molecular clouds (Spitzer and Schwarzschild 1951, 1953), the scattering by transient spiral density waves (among the first results of numerical simulations are those obtained by Sellwood and Carlberg (1984)), and the heating of the ensemble of stars that constitute the disks of spiral galaxies as they interact with external sources, for example, with low-mass satellites (see, e.g., Walker *et al.* 1999; Velasquez and White 1999).

A second remarkable peculiarity of the stellar disks is that their structure is unusually "fragile." This peculiarity was revealed by a linear analysis of the collisionless Boltzmann equation and has been repeatedly illustrated by N-body simulations. Numerous studies have shown that the initially regular structure of the stellar disks can change radically due to the growth of various instabilities, which give rise to large-scale structures both in the disk plane (bars, spiral arms, rings) and in the vertical direction (warps). The analytically and numerically obtained saturation conditions for unstable modes impose the most severe restrictions on the global structural and dynamical parameters of the stellar disks.

A local analysis suggests that the stars at a given distance R from the disk center must have a radial velocity dispersion $\sigma_R(R)$ larger than some minimum critical value $\sigma_R^{\rm cr}(R)$ (Toomre 1964) for the disk to be gravitationally stable in the region under consideration (at least against the growth of axisymmetric perturbations). In addition, for the disk to be stable against the growth of bending perturbations, the ratio of the vertical and radial velocity dispersions σ_z/σ_R must also be larger than some value approximately equal to 0.29–0.37 (Toomre 1966; Kulsrud *et al.* 1971; Polyachenko and Shukhman 1977; Araki 1985). The latter quantity determines the minimum thickness of the galactic disk, and its compar-

*E-mail: nsot@ursa.astro.spbu.ru

1063-7737/05/3101-0015$26.00

ison with the observed value allows the contribution of the bending instability to the vertical disk heating to be estimated and compared with the contribution of other relaxation mechanisms.

On the other hand, if we exclude the heating mechanisms mentioned above from our analysis and take, as is commonly done, the condition for marginal disk stability against the growth of bending modes by fixing σ_z/σ_R at a level of the linear approximation, 0.29–0.37, then the velocity dispersion σ_z at the same star surface density will decrease with decreasing σ_R (see, e.g., Zasov *et al.* 1991). In this case, the disk will have a smaller thickness.

The presence of a spheroidal component (for example, a dark halo) is known to produce a stabilizing effect and to decrease the minimum value of $\sigma_R^{\rm cr}$ required for gravitational stability. Consequently, the disks embedded in a massive halo, on average, must have low values of σ_z and be, on average, thinner. Based on similar reasoning, Zasov *et al.* (1991, 2002) showed that the relative disk thickness z_0/h (z_0 is the half-thickness of the disk, and h is the radial exponential scale length) is proportional to $M_{\rm d}/M_{\rm t}$, where $M_{\rm d}$ and $M_{\rm t}$ are, respectively, the mass of the disk and the total mass of the galaxy within a fixed radius. These authors also concluded that a small disk thickness suggests the existence of a massive dark halo in the galaxy. Moreover, based on N-body simulations, Zasov *et al.* (1991) and Mikhailova *et al.* (2001) constructed a dependence that allows the relative mass of the dark halo $M_{\rm h}/M_{\rm d}$ to be estimated from z_0/h. However, as we show below, the relationship between the relative disk thickness and the mass of the spheroidal component is more complex.

In this paper, we numerically analyze the saturation conditions for bending instability in inhomogeneous three-dimensional stellar disks at nonlinear stages in the presence of a spheroidal component of different nature (a stellar bulge and a dark halo) and the constraints imposed on the final disk thickness.

PECULIARITIES OF THE GROWTH OF BENDING INSTABILITY IN INHOMOGENEOUS THIN STELLAR DISKS

Global Modes

To understand how the growth of bending instability in inhomogeneous disks differs from that in homogeneous disks, let us first turn to the results obtained by Toomre (1966). Toomre was the first to derive the dispersion relation for long-wavelength bending perturbations in an infinitely thin gravitating layer with a nonzero velocity dispersion

$$\omega^2 = 2\pi G\Sigma|k| - \sigma_x^2 k^2, \qquad (1)$$

where Σ is the star surface density of the layer, and σ_x^2 is the velocity dispersion along a particular coordinate axis in the plane of the layer. It follows from Eq. (1) that the perturbations with a wavelength $\lambda = 2\pi/k > \lambda_J = \sigma_x^2/G\Sigma$ are stable, since $\omega^2 > 0$ in this range.

Relation (1) was derived for an infinitely thin disk and, when applied to finite-thickness disks, is valid only for perturbations with a wavelength longer than the vertical scale height of the system, i.e., for $\lambda \gg z_0$, where z_0 is the half-thickness of the layer. It can be shown from general considerations that the longest wavelength perturbations in finite-thickness disks with a wavelength $\lambda < \lambda_2 \approx z_0\sigma_x/\sigma_z$ are stable, since they are smeared by thermal motions in the plane of the layer (see, e.g., Polyachenko and Shukhman 1977). Having derived the corresponding dispersion relation, Polyachenko and Shukhman (1977) were the first to find the exact location of the stability boundary in the short wavelength range for a homogeneous flat finite-thickness layer. Araki (1985) (see also Merritt and Sellwood 1994) obtained a similar result for a homogeneous layer with a vertical density profile close to the observed one in real galaxies[1] $\rho(R,z) = \rho(R,0)\mathrm{sech}^2(z/z_0)$. As regards the intermediate wavelength ($\lambda_2 < \lambda < \lambda_J$) perturbations, they are unstable, as follows from the results of the studies mentioned above.

As the disk thickness z_0 increases, the wavelength λ_2 increases and tends to λ_J. When $\lambda_2 = \lambda_J$, the disk is stabilized against bending perturbations of any wavelengths. The following analytical estimate in the linear approximation obtained both from qualitative considerations (Toomre 1966; Kulsrud *et al.* 1971) and from an accurate analysis of the dispersion relation for a finite-thickness layer (Polyachenko and Shukhman 1977; Araki 1985) is valid:

$$(\sigma_z/\sigma_x)_{\rm cr} \approx 0.29\text{–}0.37. \qquad (2)$$

The instability is completely suppressed if $\sigma_z/\sigma_x > (\sigma_z/\sigma_x)_{\rm cr}$ and grows if $\sigma_z/\sigma_x < (\sigma_z/\sigma_x)_{\rm cr}$.

As regards the inhomogeneous models, the first thing that radically distinguishes the growth of bending instability in inhomogeneous disks from that in a homogeneous layer is the existence of global unstable bending modes with a wavelength longer than the disk scale length. This conclusion follows from an analysis of the equation that describes the evolution of long wavelength bending perturbations in an infinitely thin disk with a radially decreasing density (Polyachenko and Shukhman 1977; Merritt and Sellwood 1994). For special disk models, it was shown

[1] This profile corresponds to the model of an isothermal layer (Spitzer 1942) and describes well the vertical density variations observed in galaxies (van der Kruit and Searle 1981).

that the region of stable long wavelength perturbations narrows significantly in this case (see, e.g., Fig. 2 from Merritt and Sellwood (1994)). This is attributed to the fact that the restoring force from the perturbation that grows in an inhomogeneous disk (Merritt and Sellwood 1994) or in a radially bounded disk (Polyachenko and Shukhman 1977) is always weaker than the corresponding restoring force in a homogeneous infinite layer. This fact was demonstrated more clearly by Sellwood (1996), who noted that the dispersion relation (1) could be used to analyze the bending instability in inhomogeneous disks (at least qualitatively) if another term related to the restoring force from the unperturbed disk is added to it:

$$\omega^2 = \nu_\mathrm{d}^2 + 2\pi G\Sigma|k| - \sigma_x^2 k^2, \tag{3}$$

where $\nu_\mathrm{d} = \sqrt{\partial^2\Phi_\mathrm{d}(R,z)/\partial z^2}$ is the vertical oscillation frequency of the stars, and $\Phi_\mathrm{d}(R,z)$ is the potential of the disk.

For disks with a nonflat rotation curve, the additional term ν_d^2 can play a destabilizing role. As was noted by Sellwood (1996), for an infinitely thin inhomogeneous disk,

$$\nu_\mathrm{d}^2 = \left.\frac{\partial^2\Phi_\mathrm{d}(R,z)}{\partial z^2}\right|_{z=0+} \tag{4}$$
$$= -\frac{1}{R}\frac{\partial}{\partial R}\left(R\frac{\partial^2\Phi_\mathrm{d}}{\partial R}\right)\Bigg|_{z=0} = -\frac{1}{R}\frac{dv_\mathrm{c,d}^2}{dR}$$

($v_\mathrm{c,d}$ is the circular rotational velocity of the disk), and $\nu_\mathrm{d}^2 < 0$ for $dv_\mathrm{c,d}^2/dR > 0$.

Thus, an additional expulsive force from the unperturbed disk emerges in the central regions where the rotation curve rises. The destabilizing effect of the disk in the central regions gives rise to another region at small wave numbers (long λ) where $\omega^2 < 0$. This region is responsible for the growth of large-scale bending instability and the emergence of global modes. In this case, one might expect a larger disk thickness and a larger value of σ_z/σ_x (or σ_z/σ_R) than those in homogeneous models to be required to suppress the instability.

Applying all of this reasoning to finite-thickness disks is not quite obvious. On the one hand, it may be assumed that the restoring force from the unperturbed disk $F_z = -\partial\Phi_\mathrm{d}/\partial_z$ for $R \to 0$ behaves as $F_z \simeq -GM_\mathrm{d}z/|z|^3$ (here, M_d is the total mass of the disk) starting from some z, i.e., decreases (in magnitude) with increasing z. Consequently, $\nu_\mathrm{d}^2 = \partial^2\Phi_\mathrm{d}/\partial z^2 = -\partial F_z/\partial z$ becomes negative (Sellwood 1996).

On the other hand, we can calculate exactly the z dependence of ν_d^2 for a given R from the general formula

$$\nu_\mathrm{d}^2(\mathbf{r}) = -\partial F_z/\partial z \tag{5}$$
$$= -\frac{\partial}{\partial z}\int\frac{G\rho_\mathrm{d}(\mathbf{r}')(z'-z)}{|\mathbf{r}'-\mathbf{r}|^3}d^3\mathbf{r}'$$

for the density profile that is commonly used to describe the disks of spiral galaxies:

$$\rho_\mathrm{d}(R,z) = \frac{M_\mathrm{d}}{4\pi h^2 z_0}\exp\left(-\frac{R}{h}\right) \tag{6}$$
$$\times\,\mathrm{sech}^2\left(\frac{z}{z_0}\right),$$

where h is the exponential scale length of the disk, z_0 is the vertical scale height, and M_d is the total mass of the disk. The derived dependence[2] for various R is shown in Fig. 1b. Figure 1a shows the z dependence of the vertical force F_z, which necessarily has an extremum at some z. In the central regions, ν_d^2 is negative at $z \gtrsim 2z_0$ (on the periphery, the passage to the negative region occurs at even larger z/z_0). This implies that all of the above reasoning for finite-thickness disks is directly applicable only to large-amplitude perturbations. It is also clear that the bell-shaped (or axisymmetric) mode with the azimuthal number $m = 0$ must be most unstable in the central regions. If the amplitude of the axisymmetric bend increases significantly during the growth of bending instability, then it can raise the central stars above the plane of the disk and bring them into a "dangerous" zone where $\nu_\mathrm{d}^2 < 0$; subsequently, the self-gravity of the disk itself will contribute to the growth of a bend to the point of saturation.

The Central Regions of Hot Infinitely Thin Disks

The second peculiarity of the growth of bending instability in inhomogeneous infinitely thin disks is as follows. The degree of disk instability against bending perturbations depends on the degree of disk "heating" in the plane. Exact and approximate analyses of the dispersion relation for an inhomogeneous infinitely

[2] We see from Eq. (5) that triple integrals over infinite intervals must generally be calculated to determine ν_d^2. This can be easily done by using adaptive algorithms for calculating the integrals. In our integration, we used the gsl library (information about the gsl (GNU Scientific Library) project can be found at http://sourses/redhat/com/gsl). For models with known analytical density–potential pairs, for example, the Miyamoto–Nagai disk (see Binney and Tremaine (1987), p. 44), a comparison of the analytical z dependence of ν_d^2 at a given R with that calculated numerically by triple integration yielded a close match.

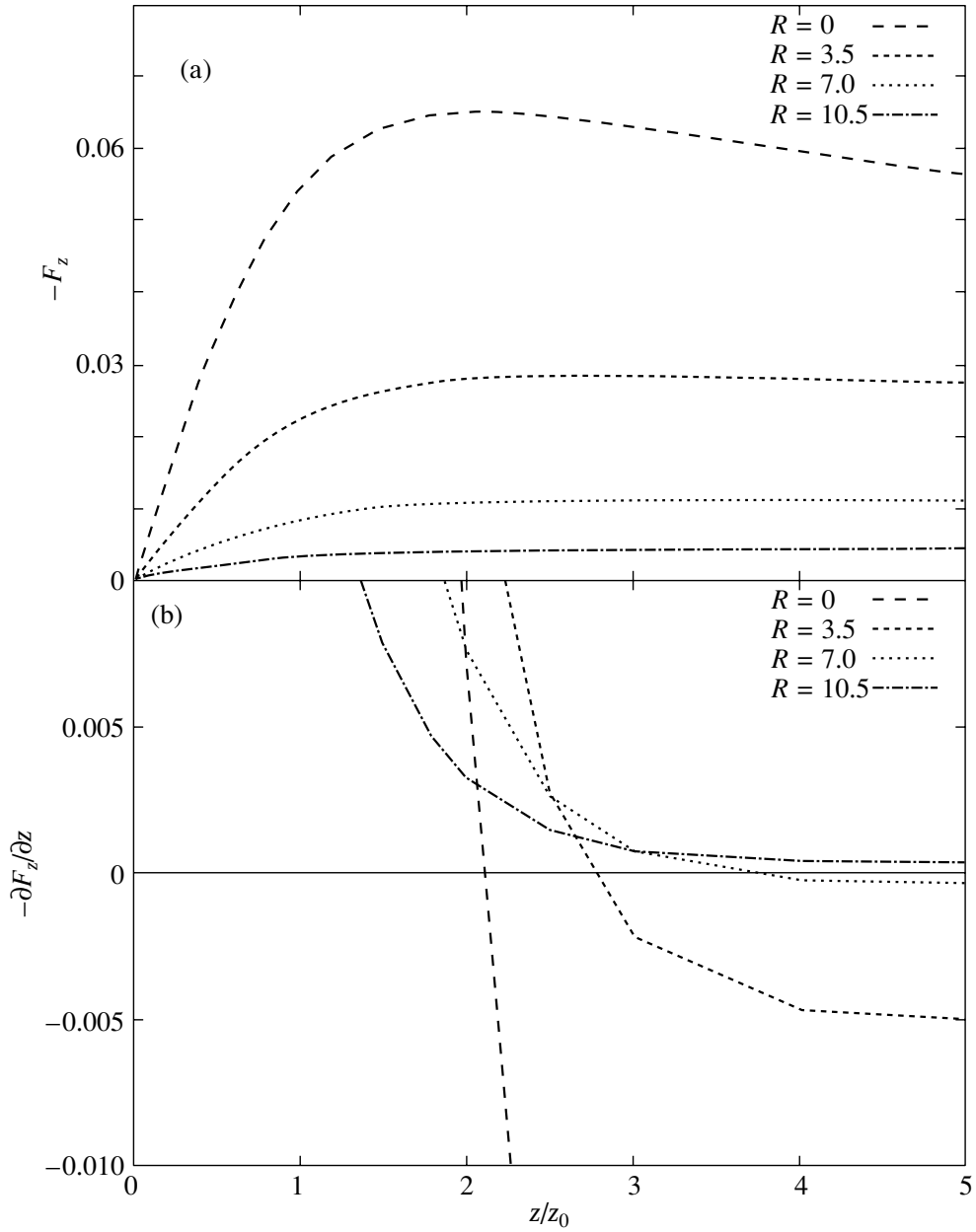

Fig. 1. (a) Magnitude of the vertical gravitational force ($-F_z$) versus z at various distances R from the disk center; (b) the square of the vertical oscillation frequency $\nu_{\rm d}^2 = -\partial F_z/\partial z$ versus z for various R. We took $G = 1$ and the disk parameters $M_{\rm d} = 1$ (the total disk mass), $h = 3.5$, and $z_0 = 0.1$.

thin disk (Polyachenko and Shukhman 1977; Merritt and Sellwood 1994) show that the modes with increasingly large azimuthal numbers in the central regions become unstable for all wavelengths as the fraction of the kinetic energy contained in the random motions in the disk plane increases. The conclusion about the existence of a Toomre parameter $Q_{\rm T}$ (Toomre 1964), which characterizes the degree of heating of the stellar disk in the plane at which the disk cannot be stabilized against bending perturbations of any wavelengths, can also be drawn from Eq. (3), i.e., the equation written for long-wavelength perturbations in a homogeneous layer, but "rectified" by the term $\nu_{\rm d}^2$ to include the inhomogeneity effects.

Indeed, $\omega^2 < 0$ for any k if

$$\nu_{\rm d}^2 + \frac{(\pi G\Sigma)^2}{\sigma_x^2} < 0.$$

Given (4),

$$\nu_{\rm d}^2 = 2\Omega_{\rm d}^2 - \kappa_{\rm d}^2,$$

where $\Omega_{\rm d}^2 = \dfrac{v_{\rm c,d}}{R}$ is the angular velocity, and

$$\kappa_{\rm d}^2 = \frac{v_{\rm c,d}^2}{R^2}\left(1 + \frac{R}{v_{\rm c,d}}\frac{dv_{\rm c,d}}{dR}\right)$$

is the square of the epicyclic frequency. Then,

$$\omega^2 < 0 \quad \text{for} \quad 2\Omega_{\rm d}^2 - \kappa_{\rm d}^2 + \frac{(\pi G\Sigma)^2}{\sigma_x^2} < 0. \qquad (7)$$

For the central regions of a rigidly rotating disk ($\kappa_{\rm d}^2 = 4\Omega_{\rm d}^2$), we obtain from (7)

$$\omega^2 < 0 \quad \text{at} \quad \sigma_x > \sqrt{2}\frac{\pi G\Sigma}{\kappa_{\rm d}} \approx \sqrt{2}\sigma_R^{\rm cr}$$

or

$$\omega^2 < 0 \quad \text{at} \qquad (8)$$
$$Q_{\rm T} > \sqrt{2} \quad \text{for any wavelengths,}$$

where $Q_{\rm T} = \sigma_x/\sigma_R^{\rm cr}$ is the Toomre parameter[3] (Toomre 1964).

Condition (8) is not an exact criterion; it is only an estimation relation. However, it shows that the central regions of hot stellar disks ($Q_{\rm T} \gg 1$) with a large reserve of strength against the growth of instabilities in the plane of the disk (bars, spiral arms) cannot be stabilized against the growth of bending perturbations of any wavelengths. The theory constructed for a homogeneous infinitely thin layer does not yield this regime. It should be borne in mind, however, that the contribution of the destabilizing term ($\nu_{\rm d}^2$) must decrease with increasing disk thickness; therefore, the instability will be saturated at a large, but finite disk thickness. However, the following might be expected: other things being equal, the hotter the initial model in the plane, i.e., the larger the Toomre parameter $Q_{\rm T}$, the higher the saturation level.

BENDING INSTABILITY: NUMERICAL SIMULATIONS OF THREE-DIMENSIONAL DISKS

The nonlinear growth stages of bending instability in inhomogeneous finite-thickness stellar disks have been extensively investigated by numerically solving the gravitational N-body problem for various stellar disk models. Raha *et al.* (1991) first observed the bending instability of bars in their numerical simulations; Sellwood and Merritt (1994) and Merritt and Sellwood (1994) studied the nonlinear regime of bending instability in nonrotating disks with the radial density profiles that corresponded to the Kuzmin–Toomre model (see, e.g., Binney and Tremaine (1987), p. 43); Griv and Chiuek (1998) numerically analyzed the development of a bend in a layer of newly formed stars; Tseng (2000) simulated the evolution of the vertical structure of a homogeneous, initially thin disk of finite radius; Sotnikova and Rodionov (2003) considered a rotating disk with an exponential density profile along the R axis and assumed the presence of a dark halo in the system. The latter authors analyzed the question of how the evolution of initially equilibrium thin disks depends on the governing parameters of the bending instability, which include the initial disk half-thickness z_0, the Toomre parameter $Q_{\rm T}$, and the relative mass of the dark halo $M_{\rm h}/M_{\rm d}$ within a fixed radius. Below, we list the most important conclusions that follow from the N-body simulations described in the literature. These conclusions agree in many respects with those given in the section entitled "Peculiarities of the growth of bending instability..." of this paper for inhomogeneous infinitely thin disks.

(1) In inhomogeneous models, all of the experimentally observed modes are global, i.e., the scale length of the unstable perturbations is larger than the disk scale. The linear theory constructed for homogeneous models yields no such result.

(2) The saturation level for the bending instability depends on σ_R (or $Q_{\rm T}$). The larger the reserve of disk strength against perturbations in the disk plane, the greater the difficulty to stabilize the disk against the growth of bending perturbations. A rapid and significant (occasionally catastrophic) increase in the disk thickness, particularly in the central regions, to values that are severalfold larger than those yielded by a linear analysis for homogeneous, moderately hot models (Toomre 1966; Kulsrud *et al.* 1971; Polyachenko and Shukhman 1977; Araki 1985) was observed in all of the simulations with initially hot disks (Sellwood and Merritt 1994; Tseng 2000; Sotnikova and Rodionov 2003). This mechanism may be responsible for the formation of central bulges in spiral galaxies, at least it can feed the spherical component with new objects.

(3) The central regions of the disk are most unstable (Sellwood and Merritt 1994; Merritt and Sellwood 1994; Griv and Chiueh 1998; Griv *et al.* 2002; Sotnikova and Rodionov 2003). It is here that the bending modes are formed. Subsequently, their amplitude increases, sometimes significantly. This is particularly true for the perturbations with $m = 0$. The nonaxisymmetric modes (with the azimuthal numbers $m = 1$ and 2) drift to the disk periphery, temporarily creating the effect of a large-scale warp

[3] Actually, the Toomre parameter should have been defined as $\sigma_R/\sigma_R^{\rm cr}$, but the difference does not matter in our case.

of the entire galaxy, and are then damped[4]. The instability in the central regions of the stellar disks is saturated at (Sotnikova and Rodionov 2003)

$$\sigma_z/\sigma_R \approx 0.75{-}0.8.$$

(4) The presence of a massive dark halo, which was included in the models by Sotnikova and Rodionov (2003), has always been a stabilizing factor that suppresses the growth of bending modes. This effect appears to have been first described qualitatively by Zasov *et al.* (1991).

THE STABILIZING EFFECT OF THE SPHEROIDAL COMPONENT: A QUALITATIVE ANALYSIS

The remarkable agreement (at least on a qualitative level) between the conclusions that follow from the analysis of the dispersion relation for an infinitely thin disk and the results of numerical simulations with three-dimensional disks allows us to analyze the applicability of yet another conclusion that can be drawn from Eq. (3) to finite-thickness disks. Since the central regions of the disk are most unstable, it is important to separate out the factors that have a stabilizing effect precisely on these regions. An additional spherical component (a dark halo, a bulge) can be such a stabilizing factor. In this case, another term related to the restoring force exerted from the spherical component appears in Eq. (3), with

$$\nu_{\rm sph}^2 = \left.\frac{\partial^2\Phi_{\rm sph}(r)}{\partial z^2}\right|_{z=0} > 0. \qquad (9)$$

This term was also introduced by Sellwood (1996) when analyzing the dispersion relation for the long-wavelength bending perturbations of an infinitely thin disk, but its role was not studied.

Zasov *et al.* (1991, 2002) and Mikhailova *et al.* (2001) concluded that the minimum possible relative thickness of an equilibrium stellar disk, z_0/h, decreases with increasing relative mass of the dark halo. Let us consider the relationship between the stellar disk thickness and the mass of the spheroidal component in terms of the stabilization conditions for the bending modes in inhomogeneous thin disks.

We take specific bulge and halo models (these models were subsequently used in our numerical calculations). A Plummer sphere is taken as the bulge model. Its potential is (see, e.g., Binney and Tremaine (1987), pp. 42–43)

$$\Phi_{\rm b}(r) = -\frac{GM_{\rm b}}{(r^2+a_{\rm b}^2)^{1/2}}, \qquad (10)$$

where $M_{\rm b}$ is the total mass of the bulge, and $a_{\rm b}$ is the scale length of the matter distribution. We describe the potential of the dark halo in terms of the logarithmic potential (see, e.g., Binney and Tremaine (1987), p. 46)

$$\Phi_{\rm h}(r) = \frac{v_\infty^2}{2}\ln(r^2+a_{\rm h}^2), \qquad (11)$$

where $a_{\rm h}$ is the scale length, and v_∞ is the velocity of a particle in a circular orbit of infinite radius. The parameter v_∞ is related to the mass of the halo with a sphere of given radius r by $M_{\rm h}(r) = \frac{v_\infty^2}{G}\frac{r^3}{r^2+a_{\rm h}^2}$.

For the additional stabilizing term in the dispersion relation, the models of the spherical components (the bulge and the halo) that we used yield

$$\nu_{\rm b}^2 = \frac{GM_{\rm b}}{(R^2+a_{\rm b}^2)^{3/2}}, \quad \nu_{\rm h}^2 = \frac{v_\infty^2}{R^2+a_{\rm h}^2}.$$

The stabilizing effect of the spherical component weakens at large R, but the disk itself in the peripheral regions has a stabilizing effect: $F_z \approx -GM_{\rm d}z/R^3$ at $|z| \ll R \Rightarrow \nu_{\rm d}^2 = -\partial F_z/\partial z > 0$. On the other hand, the strength of the effect increases in the central (most unstable) regions (i.e., for $R \to 0$); this strength depends not only on the total mass of the spherical component ($M_{\rm b}$ or v_∞), but also on the degree of matter concentration toward the center, $a_{\rm b}$ and $a_{\rm h}$. It thus follows that the presence of a compact (not necessarily massive) bulge in galaxies may prove to be enough to suppress the bending perturbations. This implies that the disks of galaxies with compact bulges can be as thin as the disks embedded in a massive dark halo.

To test our conclusion, we carried out a series of numerical simulations.

THE STABILIZATION OF BENDING PERTURBATIONS BY A COMPACT BULGE: N-BODY SIMULATIONS

The Method

We used an algorithm based on the hierarchical tree construction method (Barnes and Hut 1986) to simulate the evolution of a self-gravitating stellar disk. In our calculations, we always included the quadrupole term in the Laplace expansion of the potential produced by groups of distant bodies. The parameter θ (Hernquist 1993) that is responsible for

[4] In contrast to the result of Griv *et al.* (2002), the large-scale S-shaped or U-shaped warp of the galactic edge always disappeared on long time scales (>5 Gyr) in all of the simulations by Sotnikova and Rodionov (2003).

the accuracy of calculating the gravitational force was chosen to be 0.7 in all our simulations. The NEMO software package (http://astro.udm.edu/nemo; Teuben 1995) was taken as the basis. We enhanced the capabilities of this package by including several original codes for specifying the equilibrium initial conditions in a flat stellar system[5] and supplemented it with new models that allow us to easily analyze the data obtained and to present them in convenient graphic and video formats.

The Numerical Model

When constructing the galaxy model, we separated two components in it: a self-gravitating stellar disk and a spherically symmetric component that was described in terms of the external static potential, which is a superposition of two potentials, (10) for the bulge and (11) for the dark halo. At large distances R from the center of the stellar system, in the region where the halo dominates, potential (11) yields a flat rotation curve. The disk was represented by a system of N gravitating bodies with the density profile (6).

The initial conditions in the N-body problem suggest specifying the mass, position in space, and three velocity components for each particle. The particle coordinates are naturally determined in accordance with the disk matter density profile (6); the distant regions of the disk are disregarded. We took only those particles for which the cylindrical radius $R < R_{\max}$ and $|z| < z_{\max}$. The mass of all particles was assumed to be the same. The total mass of the particles was equal to the mass of the disk region under consideration (i.e., the disk region for which $R < R_{\max}$ and $|z| < z_{\max}$). The particle velocities were specified, using the equilibrium Jeans equations, by the standard technique (see, e.g., Hernquist (1993), Section 2.2.3).

Specifying the Velocity Field in the Model Galaxy

To specify the initial particle velocities for a disk that is in equilibrium in the plane and in the vertical direction, we make the following assumptions:

(1) The velocity distribution function is the Schwarzschild function; in other words, the particle velocity distribution function has only four nonzero moments: the mean azimuthal velocity $\bar{v}_\varphi$, the radial velocity dispersion σ_R, the azimuthal velocity dispersion σ_φ, and the vertical velocity dispersion[6] σ_z.

(2) All four moments depend only on the cylindrical radius R and do not depend on z.

(3) The epicyclic approximation is valid[7] .

(4) σ_R^2 is proportional to the surface density of the stellar disk, i.e., $\sigma_R \propto \exp(-R/2h)$ (this assumption agrees well with the observational data; see, e.g., van der Kruit and Searle 1981).

The following relations for the moments (in which the R dependence was omitted for simplicity) can then be derived from the Jeans equations (see, e.g., Binney and Tremaine 1987):

$$\begin{cases} \bar{v}_\varphi^2 = v_\mathrm{c}^2 + \sigma_R^2 - \sigma_\varphi^2 + \dfrac{R}{\Sigma_\mathrm{d}}\dfrac{\partial \Sigma_\mathrm{d}\sigma_R^2}{\partial R}, \\ \sigma_\varphi = \sigma_R \dfrac{\kappa}{2\Omega}, \\ \sigma_z^2 = \pi \Sigma_\mathrm{d} z_0, \end{cases} \tag{12}$$

where v_c is the circular velocity of a particle placed in the total potential of the disk and the spherical component, the bulge and the halo, ($v_\mathrm{c}^2 = v_{\mathrm{c,d}}^2 + v_{\mathrm{c,b}}^2 + v_{\mathrm{c,h}}^2$, $v_{\mathrm{c,b}}^2 = R\partial\Phi_\mathrm{b}/\partial R$, $v_{\mathrm{c,h}}^2 = R\partial\Phi_\mathrm{h}/\partial R$), $\Omega = v_\mathrm{c}/R$ is the angular velocity, and

$$\kappa = \sqrt{2\frac{v_\mathrm{c}^2}{R^2} + \frac{1}{R}\frac{dv_\mathrm{c}^2}{dR}}$$

is the epicyclic frequency.

The circular velocities for the bulge (10) and the halo (11) have analytical expressions. The circular velocity for the disk (6) can be determined by numerical integration (see the section entitled "Global modes") using the general formula

$$v_{\mathrm{c,d}}^2(\mathbf{r}) = \int G\rho_\mathrm{d}(\mathbf{r}')\frac{(\mathbf{r}'-\mathbf{r})\cdot\mathbf{R}}{|\mathbf{r}'-\mathbf{r}|^3}d^3\mathbf{r}', \tag{13}$$

where $\mathbf{R}$ is the projection of the vector $\mathbf{r}$ onto the disk plane.

The Jeans equations that are used to derive relations (12) are known to provide no exact disk equilibrium (see, e.g., Binney and Tremaine 1987). Moreover, the last relation in (12), which follows from the vertical equilibrium condition for a disk with the density profile (6) and a z-independent σ_z, was written without including the influence of the additional spheroidal components. The adjustment to equilibrium occurs on time scales of the order of several

[5] The mkexphot code for specifying equilibrium stellar disk models from the NEMO package has limitations on the parameters of the outer halo and does not enable the gravitational field of the bulge to be specified. The models constructed using our codes closely agree with those obtained using the mkexphot code for identical parameters.

[6] As do many members of the astronomical society, we have the bad habit of calling the standard of the distribution function the dispersion.

[7] In the central regions of the disk, this approximation breaks down.

vertical oscillation times $1/\nu_{\rm d}$. This time was always no longer than 100–120 integration time steps for the equations of motion (the thinner the disk, the shorter this time) and much shorter than the instability growth time scale in the disk. Moreover, in the context of the problem of the growth and saturation of unstable modes, a small deviation of the disk from equilibrium at the initial time may be treated as an additional initial perturbation.

The fourth assumption (see above) about the radial velocity dispersion $\sigma_R^2(R)$ causes difficulties in calculating $\bar{v}_\varphi$ in the central regions. In the first equation of system (12), $\bar{v}_\varphi^2$ is occasionally negative at small R (since $\sigma_R^2(R)$ rapidly increases toward the center, the last term on the right-hand side can make a large negative contribution). For this reason, the dependence for σ_R was reduced at the center (Hernquist 1993):

$$\sigma_R \propto \exp\left(-\sqrt{R^2-2a_{\rm s}^2}/2h\right). \qquad (14)$$

If the parameter $a_{\rm s}$ is taken to be $h/4-h/2$, then this proves to be enough to properly calculate $\bar{v}_\varphi$. In the central regions of the disk, σ_z adjusted to σ_R in such a way that the ratio σ_z/σ_R was constant at a given half-thickness $z_0 = {\rm const}$ in the initial model throughout the disk.

The proportionality factor in (14) can be determined via the Toomre parameter $Q_{\rm T}$ at some radius $R_{\rm ref}$:

$$\sigma_R(R_{\rm ref}) = Q_{\rm T}\sigma_R^{\rm cr}(R_{\rm ref}) = Q_{\rm T}\frac{3.36\Sigma_{\rm d}(R_{\rm ref})}{\kappa(R_{\rm ref})}. \qquad (15)$$

The sought proportionality factor can be obtained from (14) and (15). Specifying $Q_{\rm T}$, which ensures disk stability in the plane, at $R_{\rm ref}\approx 2.5h$ yields the condition $Q_{\rm T}(R)\geq Q_{\rm T}(R_{\rm ref})$ (Hernquist 1993). The latter, in turn, ensures a stability level against perturbations in the disk plane no lower than that at $R_{\rm ref}$. The initial half-thickness z_0 for the adopted $Q_{\rm T}(R_{\rm ref})$ was chosen in such a way that σ_z/σ_R was less than 0.3–0.4, which ensured initial instability against the growth of bending modes.

Parameters of the Problem

All of the results discussed below are presented in the following system of units: the gravitational constant is $G=1$, the unit of length is $R_u = 1$ kpc, and the unit of time is $t_u = 1$ Myr. The unit of mass is then $M_u = R_u^3/Gt_u^2 = 22.2\times 10^{10}\ M_\odot$, and the unit of velocity is $v_u = R_u/t_u = 978$ km s^{-1}.

The number of bodies in the simulations was $N=$ 300 000 (in several cases, 500 000 and 600 000). The force of interaction between two particles with coordinates $\mathbf{r}_i$ and $\mathbf{r}_j$ and masses m_i and m_j was modified, as is commonly done, as follows:

$$\mathbf{F}_{ij} = Gm_im_j\frac{\mathbf{r}_j-\mathbf{r}_i}{(|\mathbf{r}_j-\mathbf{r}_i|^2+\epsilon^2)^{3/2}},$$

where ϵ is the softening bength of the potential produced by an individual particle. When collisionless systems are simulated, this parameter is introduced for two reasons. First, the divergence of the interaction force in close particle–particle encounters must be avoided when integrating the equations of motion. Second, when the phase density of a collisionless system is represented by a finite number of particles, the inevitable fluctuations in the particle distribution must be smoothed in such a way that the forces acting in the system being simulated are close to those acting between the particles in a system with a smoother density profile. The potential softening length ϵ was chosen to be 0.02. This value is approximately a factor of 2 or 3 smaller than the mean separation between the particles (at $N=300\,000$) within the region containing half of the disk mass. On the one hand, it matches the criterion for choosing ϵ based on minimization of the mean irregular force (Merritt 1996) and, on the other hand, allows the vertical structure of thin disks to be adequately resolved.

To integrate the equations of motion for particles in the self-consistent potential of the disk and the external field produced by the spheroidal component, we used a leapfrog scheme that ensured the second order of accuracy in time step t. The time step was 0.5 (in several models, 0.25)[8].

We constructed a total of about 60 models. The entire set of models can be arbitrarily divided into two classes: the models with and without bulges. The scale length of the density distribution in the bulge $a_{\rm b}$ was assumed to be equal to 0.5 almost for all of the models with bulges. In several models without bulges, we chose a concentrated halo ($a_{\rm h}=2$). In all of the remaining cases, the halo was "looser" ($a_{\rm h}=10$). The total relative mass of the spheroidal components $\mu = M_{\rm sph}(4h)/M_{\rm d}(4h)$ was varied over the range 0.25 to 3.5

The disk in our models has the following parameters[9]: $h=3.5$ and the disk mass (in dimensional units) is $M_{\rm d}(4h) = (4–8)\times 10^{10}\ M_\odot$. The initial thickness was varied over the range $z_0 = 0.1–0.5$. In order not to abruptly cut off the model disk at the radius corresponding to the optical radius ($\sim 4h$), we chose $R_{\rm max}=25$, with $z_{\rm max}=5$. The smoothing

[8] The choice of the time step is limited above by ϵ; the particle must take at least one step on the softening length.

[9] These parameters are close those of the disk in our Galaxy.

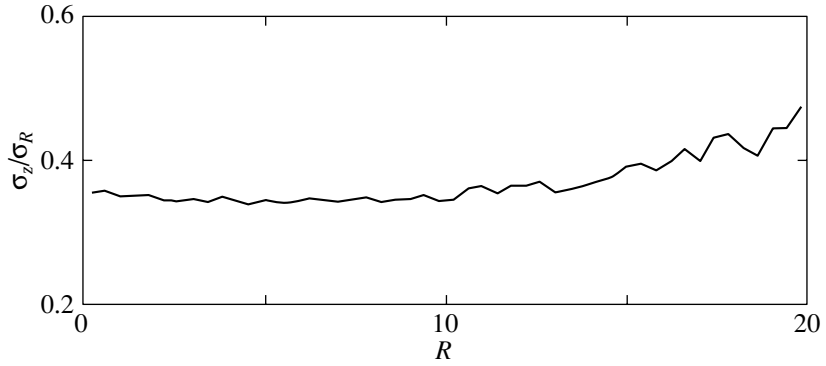

Fig. 2. Ratio σ_z/σ_R versus R for the time $t = 3000$ (model 12 with a massive halo: $\mu = 3.0$, $\mu_b = 0$).

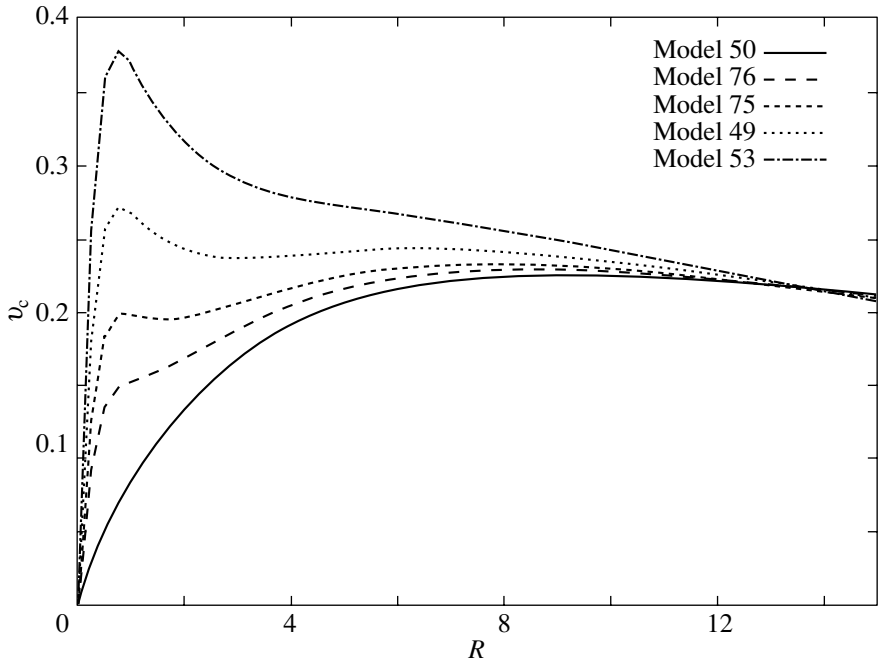

Fig. 3. Initial rotation curves for models 50, 76, 75, 49, and 53. The ratio of the total mass of the spherical component to the mass of the disk within a radius of $4h$ is the same for all models, $\mu = 0.5$; $\mu_b = 0$ for model 50, $\mu_b = 0.0625$ for model 76, $\mu_b = 0.125$ for model 75, $\mu_b = 0.25$ for model 49, and $\mu_b = 0.5$ for model 53. The unit of velocity is 978 km s^{-1}.

parameter of the initial radial profile of the velocity dispersion σ_R is $a_s = 1$. The parameter Q_T in the discussion of our simulations is given for the radius $R_{ref} = 8.5$.

Simulation Results

Previously (Sotnikova and Rodionov 2003), we showed that there are two distinct vertical stellar disk relaxation mechanisms related to bending instability: the bending instability of the entire disk and the bending instability of the bar forming in the disk. The former mechanism dominated in galaxies that are hot in the plane ($Q_T \gtrsim 2.0$), and the bar formation was suppressed in this case; the latter mechanism dominated in galaxies with a moderate Toomre parameter Q_T (such galaxies were unstable against the growth of a bar mode). In the simulations whose results are presented and analyzed below, we also considered two distinct cases: hot disks ($Q_T = 2.0$) in which only bending instability developed, and cooler models ($Q_T = 1.5$); here, we observed the combined effect of the two types of instability.

Hot disks. For hot (in the plane) disks ($Q_T = 2.0$), we revealed distinct patterns of growth and saturation of bending perturbations that are consistent with the conclusions following from a qualitative analysis of the dispersion relation (3).

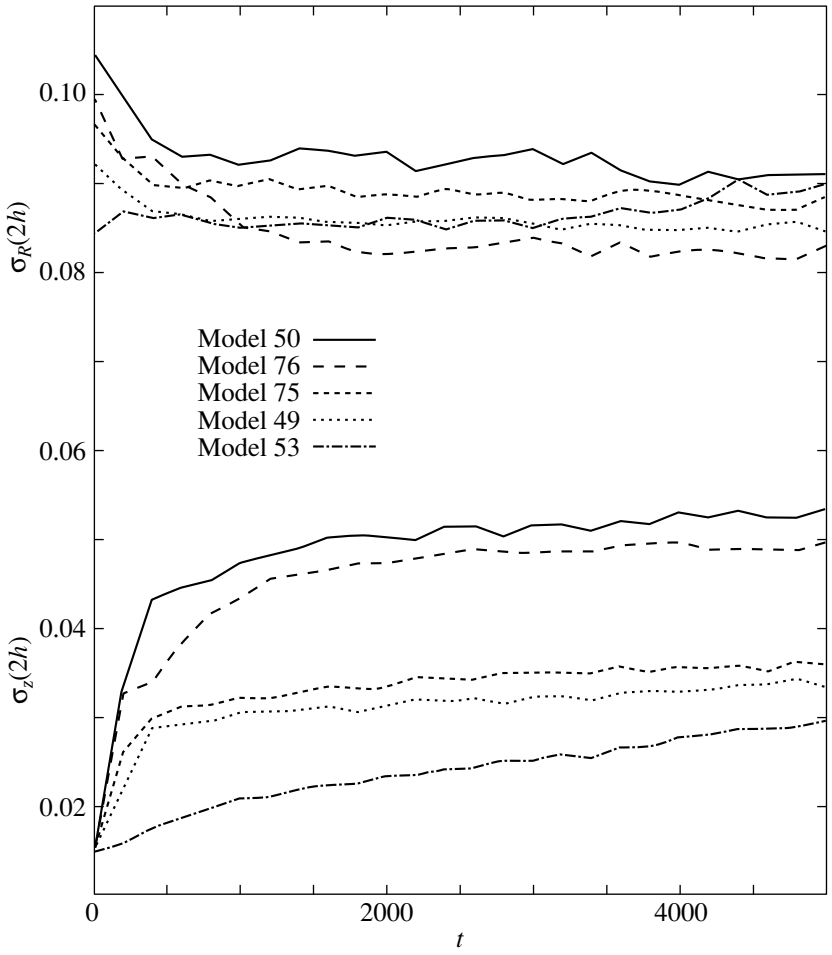

Fig. 4. Evolution of the velocity dispersions σ_R and σ_z at $R = 2h$ for the same models as those in Fig. 3.

The stabilizing effect from the presence of a massive spherical component that was discussed in the section entitled "The Stabilizing Effect of the Spheroidal Component..." is clearly seen in Fig. 2. This figure shows the radial profile of σ_z/σ_R for model 12 with $M_\mathrm{b} = 0$ and $\mu = 3.0$. Throughout the disk, σ_z/σ_R was set at $\approx$0.37 and was determined not by the bending instability, but by the disk heating through the scattering of stars by inhomogeneities related to the different disk thickness in the spiral arms and in the interarm space (Sotnikova and Rodionov 2003).

We will demonstrate the stabilizing effect of a compact (not necessarily massive) bulge comparable to the effect of a massive dark halo with a broader density profile using the results obtained for the following group of models as an example: 50, 76, 75, 49, and 53. In all five models, the total mass of the spheroidal component is the same and accounts for half of the disk mass within four exponential disk scale lengths, $\mu = 0.5$, but it is differently distributed between the two spherical subcomponents. In model 50, all of the mass is contained in the halo ($\mu = \mu_\mathrm{h} = M_\mathrm{h}(4h)/M_\mathrm{d}(4h)$); in model 53, only a compact bulge is present[10] ($\mu = \mu_\mathrm{b} = M_\mathrm{b}(4h)/M_\mathrm{d}(4h)$). The remaining models are intermediate between the two extreme models. The initial thickness for all of the models was chosen to be the same, $z_0 = 0.1$. The rotation curves for these models are shown in Fig. 3. The variety of the shown curves to some extent reflects the actual variety of rotation curves for spiral galaxies.

We traced the evolution of these models up to $t = 5000$. Figure 4 illustrates the variations in the dynamical parameters of the disk σ_R and σ_z—the radial and vertical velocity dispersions calculated at $R = 2h$. All of the models demonstrate an initial increase in σ_z

[10] In model 53, a bulge with a mass equal to half of the disk mass and a scale length of 500 pc is atypical of real galaxies. We consider this as a limiting case.

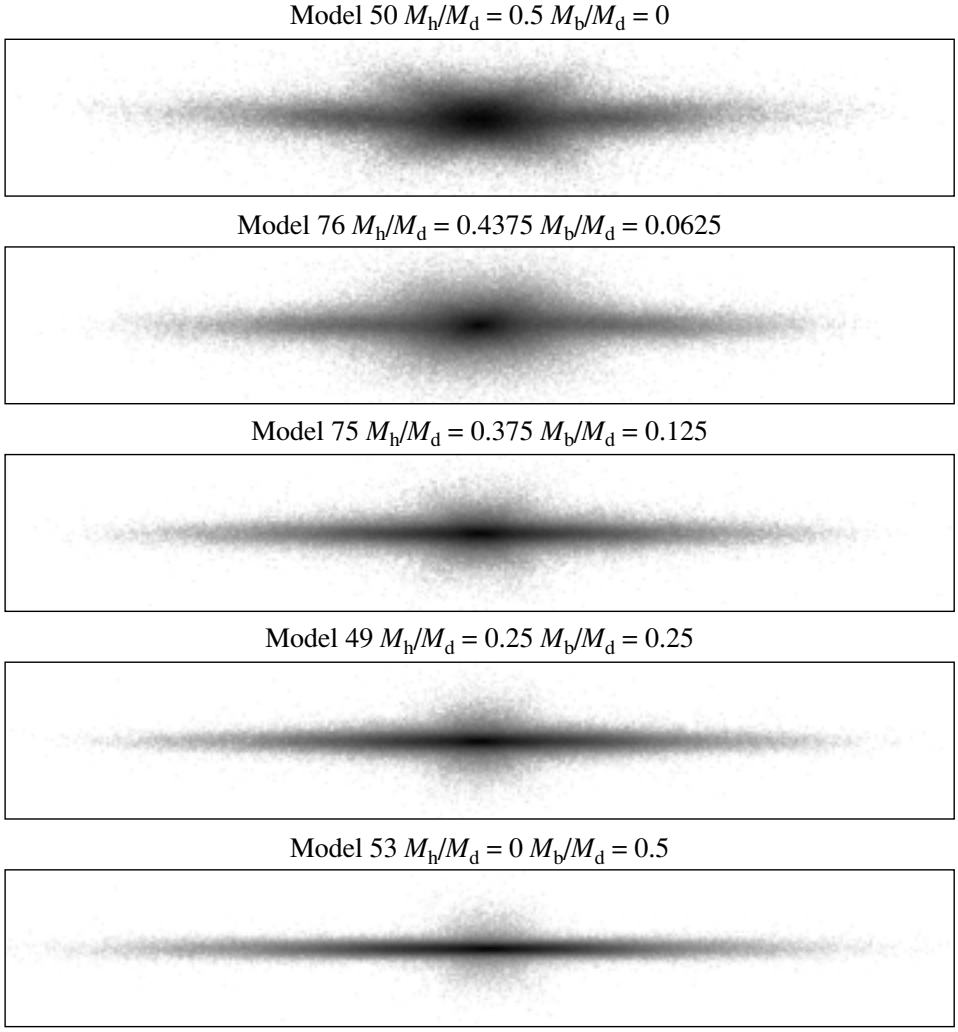

Fig. 5. Edge-on view of the galaxy at the time $t = 3000$ for models 50, 76, 75, 49, and 53. The image blackening strength corresponds to the logarithm of the particle number per pixel. The horizontal and vertical scales are 60 and 10, respectively. The ratio of the total mass of the spherical component to the mass of the disk within a radius of $4h$ is the same for all models, $\mu = 0.5$.

and a decrease in σ_R. Subsequently (after $t \approx 1000$), the latter parameter reaches an approximately constant value, while σ_z for some of the models (this is primarily true for the model with a massive bulge) continues to slowly increase. The number of particles in our models and the potential softening length were chosen in such a way that the two-body time was much longer than the time scale on which we considered the evolution of our numerical models. The absence of heating related to numerical relaxation is confirmed by the behavior of σ_R and the preservation of the pattern of evolution of the system as the number of particles increases to $N = 600\,000$. The continuing small secular increase in the vertical velocity dispersion probably reflects the fact that some of our models did not reach a steady state[11] .

Figure 5 shows five frames that correspond to the late evolutionary stages of our model disks. As expected, the saturation level for the bending instability in model 50 was very high and did not match the standard linear criterion. The galaxy greatly thickened at the final evolutionary stages. However, when we transferred 50% of the mass from the halo to the bulge (model 49: $\mu_h = \mu_b = 0.25$), the picture changed. The saturation level for the bending instability became much lower. At the final evolutionary stages, the disk

[11] If the system has no third integral of motion, then its evolution to equilibrium must eventually lead to the relation $\sigma_z = \sigma_R$.

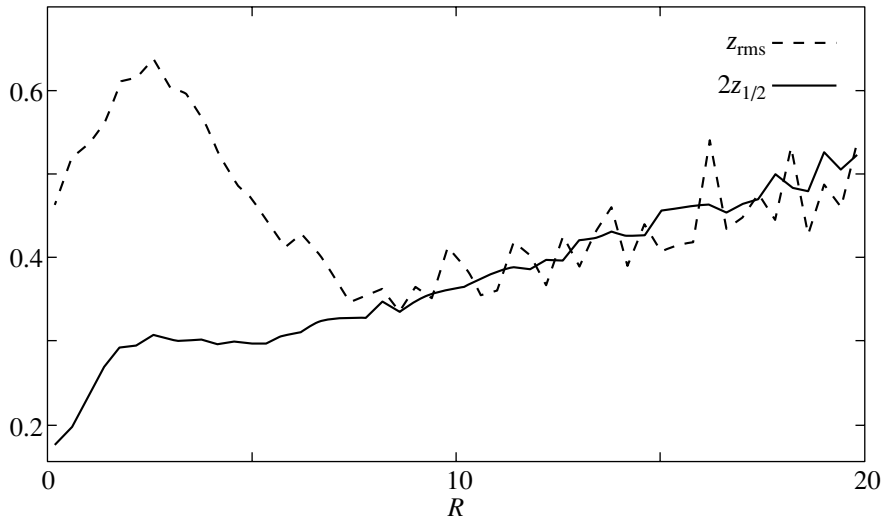

Fig. 6. Radial thickness profiles for the galaxy at the time $t = 3000$ for model 53. The thickness was determined by two methods: as the rms value of the z coordinates of the disk particles, $z_{\rm rms}$, and as twice the median of $|z|$, $2z_{1/2}$.

was much thinner than that in model 50. In model 53, when we placed all of the mass of the spherical component in the bulge, the amplitude of the observed bend was very low, and the galaxy remained quite thin even at the late evolutionary stages.

The disk thickness can be quantitatively estimated as the root-mean-square (rms) value of the z coordinates of the disk particles, $z_{\rm rms} = \sqrt{\langle z^2\rangle - \langle z\rangle^2}$. This estimate is commonly encountered in the literature. It can be shown that for the vertical density profile (6), the relationship between this parameter and z_0 is given by $z_{\rm rms} = \pi/2\sqrt{3}z_0 \approx 0.91z_0$. In practice, however, this parameter proved to be a not very good characteristic of the thickness. First, the fluctuations in this parameter along R were found to be great even when using a large number of particles if only no averaging is performed in concentric rings of large width. Second, the thickness calculated in this way turns out to be systematically overestimated due to the existence of a significant tail of the particles that went far from the disk plane. For these reasons, we estimated the disk thickness at a given distance R through the median of the absolute value of z that was designated as $z_{1/2}$. Twice the value of $z_{1/2}$ is nothing other than the disk thickness within which half of the particles is contained. For the density profile (6), $2z_{1/2} = z_0 \ln 3 \approx 1.1z_0$. Figure 6 shows the differences between the radial disk thickness profiles for model 53 obtained by the two described methods (the averaging was performed in concentric rings; the ring width was $\Delta R = 0.4$). We see that $z_{1/2}$ behaves much more smoothly (we have in mind the overall monotonic dependence of the density and the fluctuation level) than does the rms value of the z coordinate commonly used to estimate the disk thickness in N-body simulations.

Figure 7 shows the radial disk thickness profile for models 50, 76, 75, 49, and 53 at the time $t = 3000$. Note that the thickness profile for model 50 is rather unusual in shape. This shape is most likely attributable to the existence of X-shaped stationary orbits in the central regions that arise at a certain disk thickness when there are conditions for the resonance between the stellar oscillation frequencies in the disk plane and in the vertical direction (see, e.g., Patsis *et al.* 2002). We see the following from Fig. 7, as well as from Fig. 5, which show the edge-on views of the model galaxies: the thinner the galactic disk, the larger the mass of the spheroidal component contained in a compact bulge. Since not all of our models reached a steady state, their thickness continues to slowly increase (Fig. 8), but the differences in thickness are always preserved. Similar results were obtained for all of the remaining such models with the same mass of the spherical component in the range $M_{\rm sph}(4h) = 0.25M_{\rm d}(4h)$ to $M_{\rm sph}(4h) = 2.0M_{\rm d}(4h)$. The stabilizing effect of a bulge was particularly pronounced in those cases where the bulk of the galactic mass was contained in the disk.

The final disk thickness at fixed initial $Q_{\rm T}$ was determined only by the relative mass of the spheroidal component and the contribution of the bulge to this mass and did not depend on how far from stability the initial state of the disk was chosen. The start from different initial disk thicknesses led to models without any systematic differences between them. Figure 9 illustrates this result, which is similar to that obtained in their numerical simulations by Sellwood and Merritt (1994).

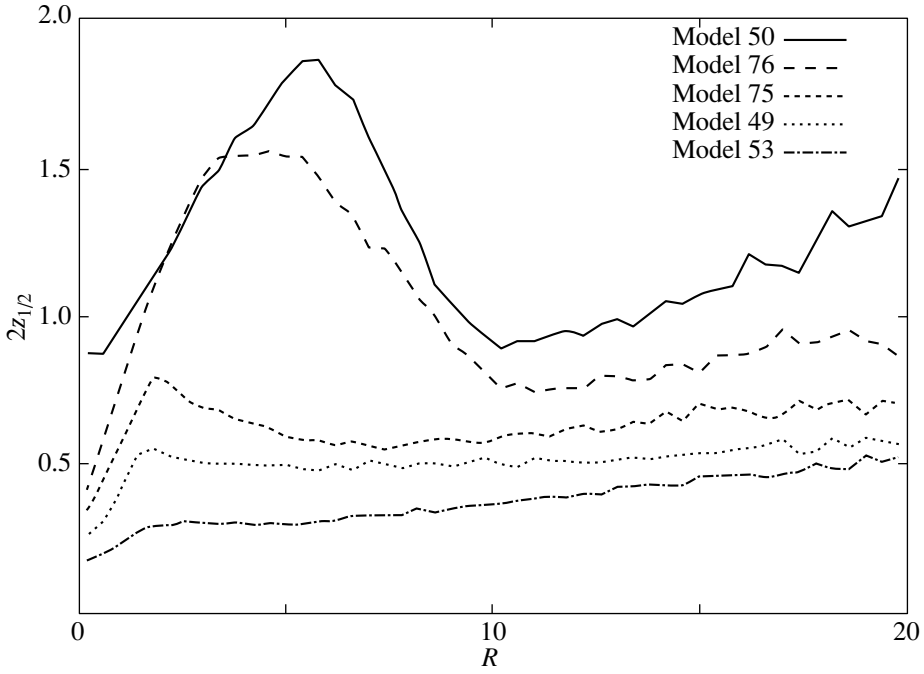

Fig. 7. Radial thickness profiles for the galaxy ($2z_{1/2}$) at the time $t = 3000$ for models 50, 76, 75, 49, and 53.

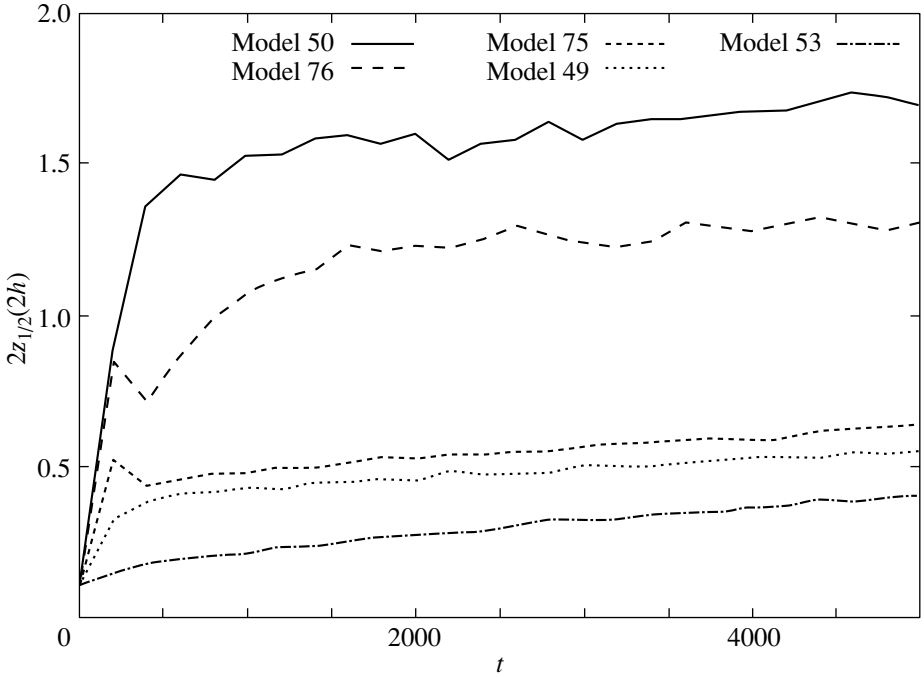

Fig. 8. Evolution of the disk thickness ($2z_{1/2}$) at $R = 2h$ for models 50, 76, 75, 49, and 53 (see the caption to Fig. 3).

Thus, our three-dimensional calculations are in good agreement with the conclusion following from our analysis of the dispersion relation for a thin disk that a bulge is an effective stabilizing factor during the growth of bending instability. Moreover, since the initial bend is formed in the most unstable central part of the galaxy (Sotnikova and Rodionov 2003), it is the central regions that must be stabilized. This does not require a massive dark halo; the presence of a compact spherical component like a bulge will suffice. This suggests that the final thickness of the model galaxy depends not only on the total mass of the spherical component, but also on the mass distribution in it.

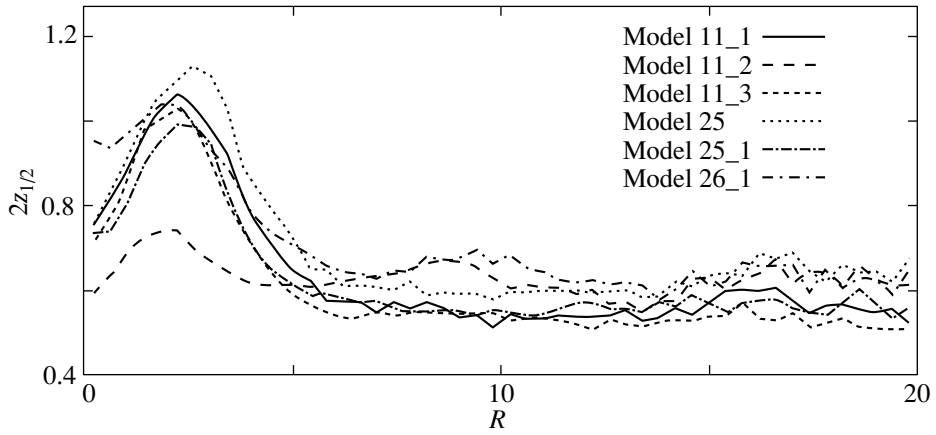

Fig. 9. Radial thickness profiles for the galaxy ($2z_{1/2}$) at the time $t = 3000$ for models that differ only by the initial thickness. For all of the models, $\mu = 0.6$ and $\mu_b = 0$. Models 11_1, 11_2, and 11_3 are different random realizations of a stellar system with $z_0 = 0.1$; models 25 and 25_1 are different random realizations of a system with $z_0 = 0.2$; model 26_1 is for $z_0 = 0.3$.

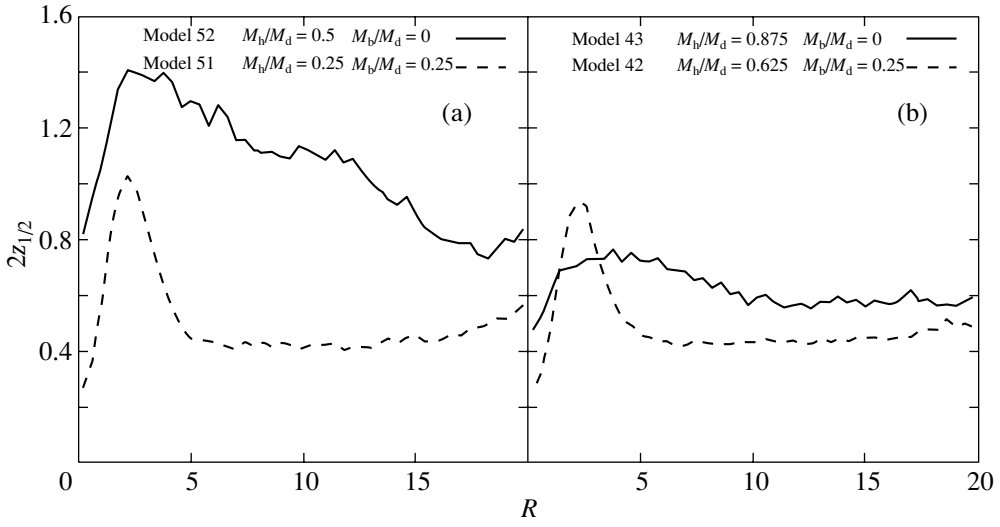

Fig. 10. Radial thickness profile for the galaxy ($2z_{1/2}$) at the time $t = 3000$ for models unstable against the growth of a bar mode ($Q_T = 1.5$): (a) models with $\mu = 0.5$ (model 52 with $\mu_b = 0$, model 51 with $\mu_b = 0.25$), (b) models with $\mu = 0.875$ (model 43 with $\mu_b = 0$, model 42 with $\mu_b = 0.25$); the initial half-thickness for all of the models is $z_0 = 0.1$.

Barred galaxies. The bending instability of bars is an effective vertical disk heating mechanism for galaxies unstable against the formation of a bar (Raha *et al.* 1991; Sotnikova and Rodionov 2003). In contrast to the warp in the entire disk, the warp in the bar is formed not in the central regions, but in the entire bar simultaneously (this is seen particularly clearly in our color two-dimensional histograms of the warp accessible at http://www.astro.spbu.ru/staff/seger/articles/warps_2002/fig6_web/html and http://www.astro.spbu.ru/staff/seger/articles/warps_2002/fig7_web/html). Therefore, the conclusion that a compact bulge during the growth of bending instability in a bar will have the same effective stabilizing effect as that for hot stellar disks is not obvious in advance.

In our simulations with $Q_T = 1.5$ and $\mu \lesssim 1.0$, the warp in the bar was formed early, at $t \approx 800$. The presence of a compact bulge eventually led to the formation of thinner disks, although the effect itself was fairly complex.

Within $R < 1.5h$, the most prominent features of the bars at late evolutionary stages were X-shaped structures. If the disk is viewed edge-on, they manifest themselves as a bulge with an appreciable extent in the z direction with boxy isophotes. In the region $R < 1.5h$ where the bar dominated, we failed to reveal any distinct patterns in the model disk thickness variations with increasing contribution of the bulge to the total mass of the spheroidal component. In general, the presence of a bulge "pushed forward" the bar formation time and caused the saturation level for the bending instability of a bar to lower. However, further analysis is required to completely understand the

processes during the interaction between a compact bulge and a bar.

As regards the peripheral regions of the disks ($R > 1.5h$), they were always appreciably thinner in the models with a compact bulge at late evolutionary stages. Figure 10 demonstrates this effect for two groups of models with different bulge contributions: models 52 and 51 with $\mu = 0.5$ and models 43 and 42 with $\mu = 0.875$. The differences in thickness show up most clearly in the models with a small relative mass of the spheroidal component. When μ increases, the disk becomes very thin, as might be expected, and its thickness ceases to depend on how the mass is distributed between the halo and the bulge.

CONCLUSIONS

A comparison of the conclusions that follow from a linear analysis with the results of numerical simulations for three-dimensional disks shows that, in contrast to homogeneous models, global bending modes with a wavelength longer than the disk scale length can arise in inhomogeneous disks. If the amplitude of the waves during the growth of instability increases significantly, they heat it significantly in the vertical direction as they pass through the entire disk. Hot disks are most unstable against the growth of bending perturbations. An additional spheroidal component (e.g., a dark halo) is a factor that stabilizes the bending perturbations.

Our additional qualitative analysis of the dispersion relation for inhomogeneous models led us to new conclusions regarding the stabilization conditions for the bending modes in stellar disks. These conclusions were confirmed in our numerical simulations.

(1) Since the central regions of the disk (particularly if the disk is hot) are most unstable, the conditions under which the growth of perturbations is suppressed are determined not only by the mass of the spherical component, but also by the density distribution in it. The suppressing effect is enhanced with increasing concentration toward the center.

(2) The presence of a compact and moderately massive bulge in a galaxy effectively prevents the growth of bending perturbations.

(3) It follows from an analysis of our results that a more accurate approach to estimating the dark halo mass from the observed relative thickness of the stellar disk z_0/h in spiral galaxies is required.

ACKNOWLEDGMENTS

This work was supported by the Russian Foundation for Basic Research (project no. 03-02-1752), the Federal Astronomy Program (project no. 40.022.1.1.1101), and an RF Presidential Grant for Support of Leading Scientific Schools (NSh-1088.2003.2).

REFERENCES

1. S. Araki, Ph. D. Thesis (Massachus. Inst. Tech., 1985).
2. J. Barnes and P. Hut, Nature **324**, 446 (1986).
3. J. Binney and S. Tremaine, *Galactic Dynamics* (Princeton Univ. Press, Princeton, 1987).
4. E. Griv and M. Gedalin, Astrophys. J. **580**, L27 (2002).
5. E. Griv and Tzihong Chiueh, Astrophys. J. **503**, 186 (1998).
6. L. Hernquist, Astrophys. J., Suppl. Ser. **86**, 389 (1993).
7. P. C. van der Kruit and L. Searle, Astron. Astrophys. **95**, 105 (1981).
8. R. M. Kulsrud, J. W.-K. Mark, and A. Caruso, Astrophys. Space Sci. **14**, 52 (1971).
9. D. Merritt, Astron. J. **111**, 2462 (1996).
10. D. Merritt and J. A. Sellwood, Astrophys. J. **425**, 551 (1994).
11. E. A. Mikhailova, A. V. Khoperskov, and S. S. Sharpak, *Stellar Dynamics—from Classic to Modern*, Ed. by L. P. Ossipkov and I. I. Nikiforov (St. Petersburg State Univ. Press, St. Petersburg, 2001), p. 147.
12. P. A. Patsis, E. Athanassoula, P. Grosbol, and Ch. Skokos, Mon. Not. R. Astron. Soc. **335**, 1049 (2002).
13. V. L. Polyachenko and I. G. Shukhman, Pis'ma Astron. Zh. **3**, 254 (1977) [Sov. Astron. Lett. **3**, 134 (1977)].
14. N. Raha, J. A. Sellwood, R. A. James, and F. D. Kahn, Nature **352**, 411 (1991).
15. J. A. Sellwood, Astrophys. J. **473**, 733 (1996).
16. J. A. Sellwood and R. G. Carlberg, Astrophys. J. **282**, 61 (1984).
17. J. A. Sellwood and D. Merritt, Astrophys. J. **425**, 530 (1994).
18. N. Ya. Sotnikova and S. A. Rodionov, Pis'ma Astron. Zh. **29**, 367 (2003) [Astron. Lett. **29**, 321 (2003)].
19. L. Spitzer, Astrophys. J. **95**, 325 (1942).
20. L. Spitzer and M. Schwarzshild, Astrophys. J. **114**, 385 (1951).
21. L. Spitzer and M. Schwarzshild, Astrophys. J. **118**, 106 (1953).
22. P. J. Teuben, Astron. Soc. Pac. Conf. Ser. **77**, 398 (1995).
23. A. Toomre, Astrophys. J. **139**, 1217 (1964).
24. A. Toomre, Geophys. Fluid Dyn., No. 66–46, 111 (1966).
25. Yao-Huan Tseng, Chin. J. Phys. **38**, 111 (2000).
26. H. Velasquez and S. D. M. White, Mon. Not. R. Astron. Soc. **304**, 254 (1999).
27. I. W. Walker, J. Ch. Mihos, and L. Hernquist, Astrophys. J. **460**, 121 (1996).
28. A. V. Zasov, D. V. Bizyaev, D. I. Makarov, and N. V. Tyurina, Pis'ma Astron. Zh. **28**, 527 (2002) [Astron. Lett. **28**, 527 (2002)].
29. A. V. Zasov, D. I. Makarov, and E. A. Mikhaĭlova, Pis'ma Astron. Zh. **17**, 884 (1991) [Sov. Astron. Lett. **17**, 374 (1991)].

Translated by V. Astakhov

Astronomy Letters, Vol. 31, No. 1, 2005, pp. 30–36. Translated from Pis'ma v Astronomicheskiĭ Zhurnal, Vol. 31, No. 1, 2005, pp. 33–38.

Two-Frequency Timing of the Pulsar B1937+21 in Kalyazin and Kashima in 1997–2002

Yu. P. Ilyasov[1*], M. Imae[2], Y. Hanado[3], V. V. Oreshko[1], V. A. Potapov[1***], A. E. Rodin[1], and M. Sekido[4]**

[1] *Pushchino Radio Astronomy Observatory, Astrospace Center, Lebedev Institute of Physics, Russian Academy of Sciences, Pushchino, Moscow oblast, 142292 Russia*

[2] *National Metrology Institute of Japan, Tsukuba Central 3, Umezono 1-1-1, Tsukuba, Ibaraki 305-8563, Japan*

[3] *National Institute of Information and Communications Technology, 4-2-1 Nukui-Kita, Koganei, Tokyo, 184-8795 Japan*

[4] *National Institute of Information and Communications Technology, Kashima Space Research Center, 893-1 Hirai, Kashima, Ibaraki 314, Japan*

Received May 26, 2004

Abstract—We present the results from our timing of the millisecond pulsar B1937+21, performed jointly since 1997 on two radio telescopes: the RT-64 in Kalyazin (Russia) at a frequency of 0.6 GHz and RT-34 in Kashima (Japan) at a frequency of 2.15 GHz. The rms value of the pulse time of arrival (TOA) residuals for the pulsar at the barycenter of the Solar system is 1.8 μs (the relative variation is $\approx 10^{-14}$ over the observing period). The TOA residuals are shown to be dominated by white phase noise, which allows this pulsar to be used as an independent time scale keeper. The upper limit for the gravitational background energy density $\Omega_g h^2$ at frequencies $\approx 6.5 \times 10^{-9}$ Hz is estimated to be no higher than 10^{-6}. Based on the long-term timing of the pulsar, we have improved its parameters and accurately determined the dispersion measure and its time variation over the period 1984–2002, which was, on average, $-0.00114(3)$ pc cm^{-3} yr^{-1}.

Key words: *pulsars, neutron stars, and black holes, timing, gravitational waves, dispersion measure.*

INTRODUCTION

As is well known, the timing of pulsars allows their main parameters to be accurately determined: the observed spin period and its derivatives, the coordinates and proper motions, and, for binary pulsars, the Keplerian orbital and relativistic parameters of the binary system. The pulsar signals recorded as pulses with a highly stable repetition period propagate in the interstellar medium, the interplanetary medium, and the ionosphere, and their arrival time varies. The latter allows us to study the properties of the propagation medium, including the disturbances in the interstellar medium; the passage near the line of sight of gravitating masses; and the presence of gravitational-wave radiation. The fastest pulsar, B1937+21, with a spin period of about 1.56 ms, was discovered in 1982 (Backer *et al.* 1982). A large body of observational data, including those accessible via the Internet (Kaspi *et al.* 1994), has been accumulated since its discovery. Their analysis performed by different authors show that the spin period of B1937+21 is highly stable on long time scales, making it one of the best pulsar time scale keepers (Il'in *et al.* 1984).

The timing of millisecond pulsars allows their astrometric parameters to be determined with high accuracy. In particular, the coordinates and proper motions of the pulsar B1937+21 can be determined with errors of about 10^{-4} arcsec and 10^{-5} arcsec yr^{-1}, respectively (Kaspi *et al.* 1994).

The dispersion measure can be determined by measuring the pulse time of arrival (TOA) delay t between frequencies f_1 and f_2 ($f_1 > f_2$) due to the passage through ionized interstellar plasma:

$$DM = 2.410 \times 10^{-16} t \left(\frac{1}{f_2^2} - \frac{1}{f_1^2} \right)^{-1} \text{ pc cm}^{-3}. \quad (1)$$

*E-mail: ilyasov@prao.psn.ru
**E-mail: yuko@nict.go.jp
***E-mail: potap@prao.psn.ru

1063-7737/05/3101-0030$26.00

Clearly, the measurement error in the dispersion measure δDM is determined by the limiting accuracy of measuring the TOA difference δt at these frequencies. Substituting the frequencies of observations in Kalyazin and Kashima into Eq. (1) yields a simple relation: $\delta DM \approx 94\delta t_{[0.6-2.15]\ \mathrm{GHz}}$ pc cm^{-3}, where δt is in seconds. Thus, for a typical $\delta t \approx 1$ μs, the error in the dispersion measure is ≈ 0.000094 pc cm^{-3} in our case. Since we compare the TOAs reduced to the barycenter of the Solar system, observations can be performed both on the same telescope or (as in our case) on different telescopes.

OBSERVATIONS AND DATA ANALYSIS

As we noted above, the pulsar B1937+21 was observed as part of a joint timing program with the RT-64 radio telescope at the Kalyazin Radio Astronomy Observatory (Astrospace Center, Lebedev Institute of Physics, Russian Academy of Sciences) and the RT-34 radio telescope at the Kashima Space Research Center (National Institute of Information and Communications Technology, Japan) at frequencies of 0.6 and 2.15 GHz, respectively. Below, we present the results from our reduction of the data obtained over five years, from June 1997 through June 2002.

In Kalyazin, we used the AS-0.6 pulsar complex of the Pushchino Radio Astronomy Observatory (Astrospace Center, Lebedev Institute of Physics, Russian Academy of Sciences) (two circular polarizations, 80 receiving channels in each polarization, 40 kHz in each channel) (Ilyasov *et al.* 2000). Each observing session lasted about two hours. The signal was accumulated in channels during the synchronous summation with the pulsar period over a 3-min cycle. The delay in the receiving channels due to the dispersion in the interstellar medium was compensated for during the subsequent reduction. The channel sampling interval was 10 μs. The pulsar pulses obtained in individual observing cycles were added to increase the signal-to-noise ratio. To obtain the integrated profile, we added at least 10^5 pulses from the pulsar B1937+21. The instrumental measurement error of the TOAs was about 100 ns.

In Kashima, the observations were performed in a 200-MHz band using mostly right-hand circular polarization. The signal was divided into four 50-MHz-wide channels and recorded in four acoustooptic analyzers with 256 200-kHz channels. The sampling interval per channel was 15.6 μs (Hanado *et al.* 2002).

The TOAs on both telescopes were recorded on the local time scale determined from GPS signals and were reduced to the UTC scale. The rms deviation of the arrival times of 1-Hz GPS signals was 10–15 ns. The observations in Kalyazin were also reduced to the UTC(SU) scale using TV signals.

We determined the topocentric TOAs from the maximum of the cross correlation between the pulse profile obtained during a session and the template, the reference profile determined by adding the pulsar pulses using more than ten observing sessions. We computed the barycentric TOAs and their residuals and improved the parameters of the pulsar B1937+21 by the least-squares method using the TIMAPR (Doroshenko and Kopeĭkin 1990) and TEMPO (Taylor and Weisberg 1989) codes.

Figure 1 shows the systematic drift of the TOA residuals observed at 0.6 GHz relative to those observed at 2.15 GHz that was determined by assuming that $DM = \mathrm{const}$. This drift shows an additional delay in the signal propagation through the medium due to the change in the dispersion measure over the period of our simultaneous observations. Clearly, the variations in DM must be taken into account when reducing the TOA series. Otherwise, the least-squares estimates of the pulsar parameters become biased, and the rms value of the TOA residuals increases significantly.

In most cases, the behavior of the dispersion measure is well fitted by a time polynomial, which allows us to simultaneously reduce the multifrequency observations and to obtain a consistent series of TOA residuals with high accuracy. In our case, the behavior of DM is well described by a cubic time polynomial (fitting DM by higher-degree (up to the ninth degree inclusive) polynomials causes no significant change in the series of TOA residuals, suggesting that the chosen model is adequate). Figure 2 shows the series of TOA residuals in the frequency range 0.6–2.15 GHz obtained by fitting DM by a cubic polynomial (the rms value of the TOA residuals is $\approx$1.8 μs).

The table gives the parameters of the pulsar B1937+21 obtained after reducing the observational data using the TIMAPR and TEMPO code with allowance made for the variation in dispersion measure with time. The values in the third and fourth columns of the table agree, within the error limits, illustrating a weak dependence of the result on the algorithm used (the TIMAPR and TEMPO codes). The differences between the astrometric parameters given in the fourth and fifth columns are attributable to the rotation of the coordinate axes of the systems of DE200 and DE405 ephemerides and their rotation with respect to one another (Standish *et al.* 1995; Standish 1998).

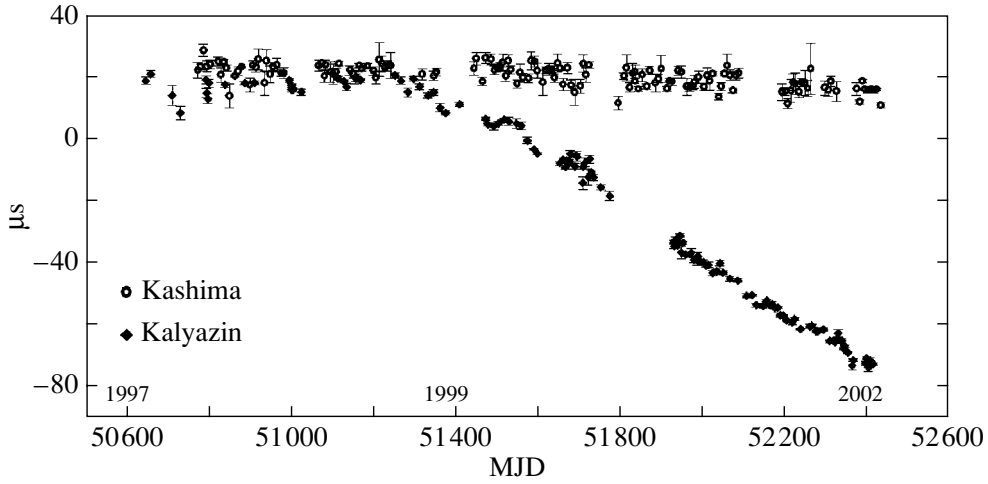

Fig. 1. TOA residuals for the pulsar B1937+21, estimated from the Kalyazin (0.6 GHz) and Kashima (2.15 GHz) observations. The dispersion measure is assumed to be constant and calculated at MJD = 51000.

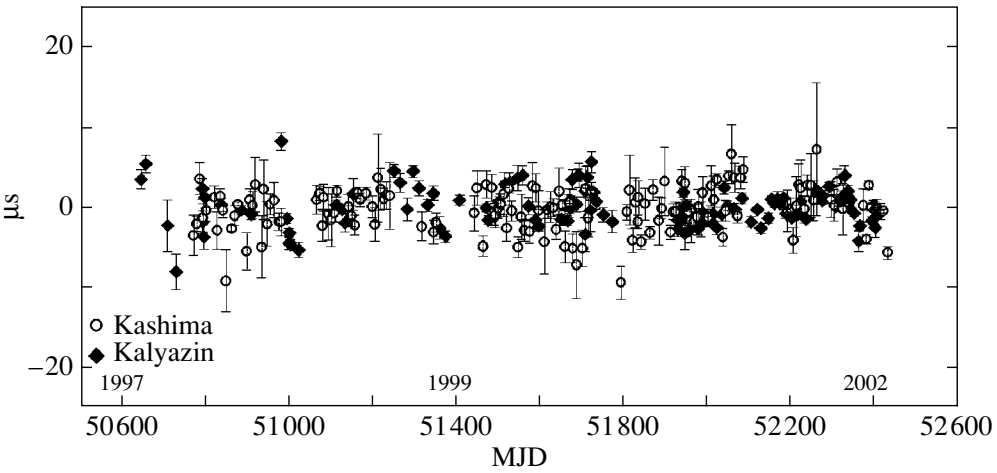

Fig. 2. TOA residuals for the pulsar B1937+21, estimated from the Kalyazin (0.6 GHz) and Kashima (2.15 GHz) observations.

RELATIVE SPIN INSTABILITY OF THE PULSAR AND ESTIMATING THE GRAVITATIONAL WAVE BACKGROUND

The pulsar spin instability in the time domain can be estimated by using the variance σ_z^2 (Taylor 1991), an extension of the concept of Allan variance σ_y^2 (Allan 1966).

The introduction of the variance σ_z^2 is necessitated by the peculiarities of the timing data reduction; more specifically, when the pulsar parameters are improved by the least-squares method, the series of TOA residuals is fitted by a time polynomial specified by the pulsar spin rate and its derivative. To avoid the ambiguity caused by this procedure, we introduce a statistic for estimating the σ_z^2 frequency instability by calculating the third differences of the TOA residuals (related to the second derivative of the frequency). The algorithm of its calculation for unevenly spaced series (which is typical for pulsar observations) was described by Matsakis *et al.* (1997).

Note that σ_z can also be calculated directly using finite differences if the series of TOA residuals are first reduced to evenly spaced series, for example, by spline interpolation. This procedure results in a difference between the σ_z estimates on short time intervals τ and is in close agreement, within the error limits, with the procedure suggested by Matsakis *et al.* (1997) on the long time intervals that are of greatest interest to us.

Figure 3 shows the dependence of σ_z calculated from the TOA residuals for the pulsar B1937+21

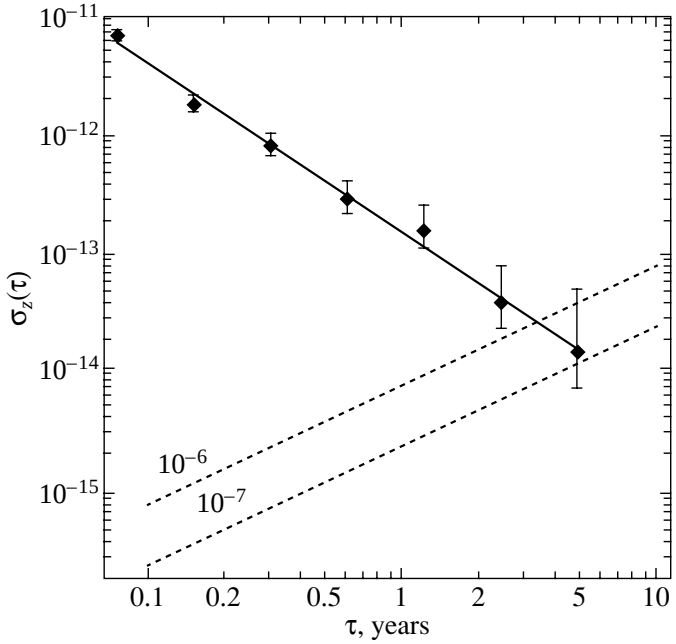

Fig. 3. Fractional spin instability $\sigma_z(\tau)$ of the pulsar PSR B1937+21 calculated from the Kalyazin and Kashima data averaged over a one-day interval. The dots with error bars indicate $\sigma_z(\tau)$ calculated on the nonoverlapping τ intervals that are multiples of the entire observing time τ ($T/64 < \tau < T$). The solid line represents the regression straight line with a logarithmic slope of $-1.43(2)$. The dashed straight lines correspond to the gravitational wave background energy densities $\Omega_g h^2 = 10^{-6}$ and 10^{-7}.

on the time interval τ. It shows σ_z calculated on nonoverlapping subintervals $\tau = T, T/2, T/4, \ldots, T/64$ in duration, where T is the total duration of the series of observations.

By theoretically modeling the behavior of σ_z for the series of TOA residuals perturbed by a stochastic gravitational wave background with the relative logarithmic density

$$\Omega_g(f) = \frac{f}{\rho_c}\frac{d\rho_g(f)}{df},$$

where f is the radiation frequency, ρ_c is the critical density of the Universe, and ρ_g is the energy density of the gravitational wave background, we can estimate its upper limit (Kopeikin 1997; Ilyasov *et al.* 1998). Figure 3 shows the straight lines that represent the theoretical plots of the behavior of $\sigma_z(\tau)$ attributable to the TOA phase perturbations only by the background gravitational wave radiation with $\Omega_g h^2 = 10^{-6}$ and 10^{-7}. Here, $h = H_0/(100\ \mathrm{km\ s^{-1}\ Mpc^{-1}})$ and H_0 is the Hubble constant. The σ_z curve is seen to cross the $\Omega_g h^2 = 10^{-6}$ straight line.

The dependence $\sigma_z(\tau)$ can be well fitted by a straight line with a logarithmic slope of about $-1.43(2)$, which is closest to the model of white phase noise (a slope of $-3/2$). The lowest value of $\sigma_z(\tau)$ is $\approx 2 \times 10^{-14}$. Since as yet no positive derivative has been observed in the behavior $\sigma_z(\tau)$, further observations could allow us to reach lower values of $\sigma_z(\tau)$ and to lower the upper limit for $\Omega_g h^2$.

LONG-TERM VARIATION OF THE DISPERSION MEASURE

Several authors (Cordes and Stinebring 1984; Rawley *et al.* 1988; Cordes *et al.* 1990; Backer *et al.* 1993; Kaspi *et al.* 1994; Cognard *et al.* 1995; Lestrade *et al.* 1998) have pointed out the variations in dispersion measure toward the pulsar B1937+21 previously. The dispersion measure was measured by the method of multifrequency timing. Two approaches are possible: in the first approach, the difference between the barycentric TOAs at different frequencies is directly measured during each observing session, and the correction to the dispersion measure for the time of the session under consideration is calculated from this difference using Eq. (1). The value of DM calculated in this way can be used to further improve the parameters of the pulsar by the least-squares method at the subsequent iteration steps. In the second approach to the problem, a global improvement of the parameters of the multifrequency observations of pulsars, including DM and its derivatives, is made by the least-squares method. The time boundaries of the series of TOA residuals must not necessarily coincide

Parameters of the millisecond pulsar B1937+21, improved by the timing method

Parameter	TIMAPR(DE200) 600 MHz	TIMAPR(DE200)	TEMPO(DE200)	TEMPO(DE405)
Epoch T_0(MJD)	51000.0	51000.0	51000.0	51000.0
$\alpha(J2000)$h:m:s	19:39:38.56010(2)	19:39:38.56010(1)	19:39:38.560093(5)	19:39:38.561257(5)
$\delta(J2000)$ °:′:″	21:34:59.1378(3)	21:34:59.1379(2)	21:34:59.1382(1)	21:34:59.1322(1)
μ_α 0.001″ yr^{-1}	−0.21(7)	−0.2(1)	−0.18(3)	0.02(3)
μ_δ 0.001″ yr^{-1}	−1.09(9)	−1.1(1)	−1.07(4)	−1.01(4)
P, ms	1.55780650060606(4)	1.55780650060595(7)	1.557806500605933(5)	1.557806500606535(6)
$\dot{P}$, s s^{-1}	$1.05100(3)\times10^{-19}$	$1.05134(3)\times10^{-19}$	$1.051358(5)\times10^{-19}$	$1.051368(6)\times10^{-19}$
$\ddot{P}$, s^{-2}	$-1.1(2)\times10^{-30}$	$-1.3(1)\times10^{-30}$	$-1.3(2)\times10^{-30}$	$-1.3(2)\times10^{-30}$
DM, pc cm^{-3}	71.0307	71.03046(6)	71.03034(2)	71.03034(2)
$DM1$, pc cm^{-3} yr^{-1}	–	$2.1(1)\times10^{-4}$	$2.4(4)\times10^{-4}$	$2.4(4)\times10^{-4}$
$DM2$, pc cm^{-3} yr^{-2}	–	$-1.13(8)\times10^{-3}$	$-1.16(3)\times10^{-3}$	$-1.16(3)\times10^{-3}$
$DM3$, pc cm^{-3} yr^{-3}	–	$1.4(1)\times10^{-4}$	$1.46(5)\times10^{-4}$	$1.46(6)\times10^{-4}$

Note. The parameters of the millisecond pulsar B1937+21 were determined from the single-frequency observations in Kalyazin (column 2) and the two-frequency observations in Kalyazin and Kashima (columns 3–5). The parameters $DM1$, $DM2$, and $DM3$ are the coefficients of the terms of the expansion of DM into a power series of $(t - T_0)$ up to the third power inclusive. We used the DE200 and DE405 ephemerides and the TOA series averaged over a one-day interval. As the zero approximation for improving the parameters, we took the coordinates, the period, and the dispersion measure from the paper by Lange *et al.* (2000). The parameter DM in the first column is assumed to be constant.

in this case. The series themselves can be obtained at different observatories, and observing sessions can be conducted at different times. Note once again that, if we disregard the variation in DM, the reduction of the series of single-frequency TOAs will result in a redetermination of the observed barycentric pulsar period and its derivatives:

$$\frac{d^{(n-1)}P}{dt^{n-1}} \propto \frac{d^n DM}{dt^n}.$$

In addition, ignoring the short-term variations in DM will cause the estimated variance of the TOA residuals to increase.

Figure 4 shows the variation in the dispersion measure toward PSR B1937+21 over 20 years obtained from published data and from the Kalyazin and Kashima observations over the period 1997–2002.

We calculated the rate of decrease of the dispersion measure for the entire series during the period from 1984.5 until 2002.5, which in the linear approximation is −0.00114(3) pc cm^{-3} yr^{-1}.

Slow variations of the dispersion measure, although not on such long time intervals, were also reported for other pulsars (e.g., PSR B1821–24 and J1855+09, Backer *et al.* (1993), and PSR B1821–24, Cognard and Lestrade (1997)). This behavior of the dispersion measure can be qualitatively explained by the crossing of the line of sight by layers of the interstellar medium with different densities due to the relative motion of the pulsar, the observer, and the interstellar medium itself; the crossing of the line of sight by compact regions of ionized plasma (an extreme scattering event—ESE) (Lestrade *et al.* 1998; Maitia *et al.* 2003); and the dissipation of the cloud of ionized gas surrounding the pulsar, including the cloud remaining from the companion of the pulsar B1937+21 that possibly existed earlier.

The noticeable (in Fig. 4) discrepancy between the DM values obtained from the observations at different pairs of frequencies can be explained by several factors (Cordes *et al.* 1990):

(1) The effect of the change in pulse shape at different frequencies due to interstellar scattering;

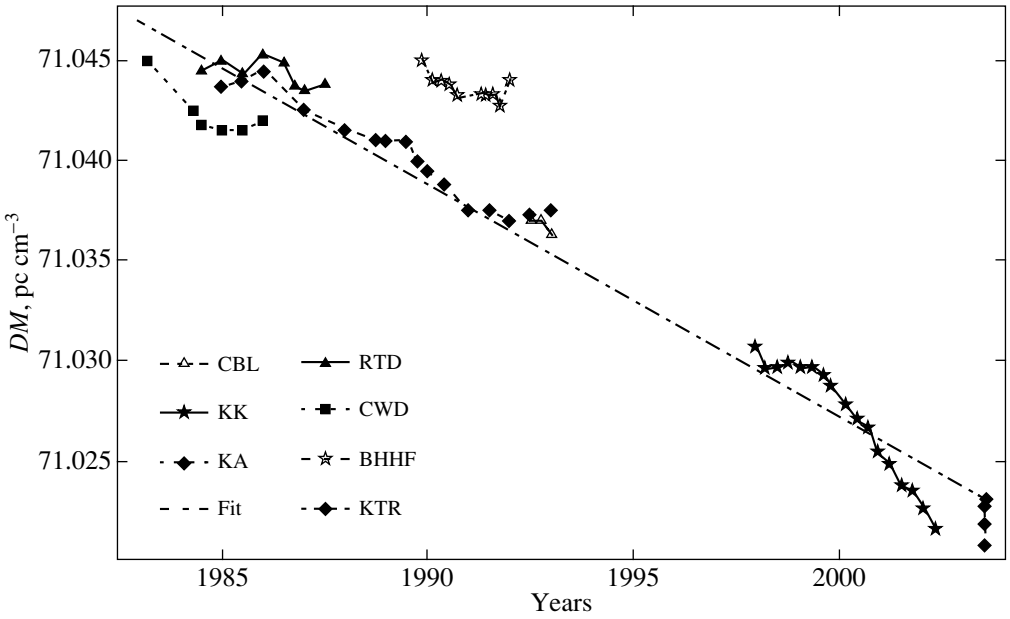

Fig. 4. Variation in the dispersion measure of the pulsar B1937+21 for the period 1984–2003: RTD—Rawley *et al.* (1988), frequency range 1.4–2.4 GHz; CWD—Cordes *et al.* (1990), 0.43–1.4 GHz; BHHF—Backer *et al.* (1993), 0.8–1.33 GHz; KTR—Kaspi *et al.* (1994), 1.4–2.4 GHz; CBL—Cognard *et al.* (1995), 1.41–1.68 and 1.28–1.7 GHz; KK—Kalyazin and Kashima, 0.6–2.15 GHz; KA—Kalyazin, direct DM measurements, 0.6–1.4 GHz (Esepkina *et al.* 2003); Fit—regression straight line drawn using all of the data.

(2) The frequency dependence of the pulse shape;

(3) The pulse delay due to the frequency dependence of the radiation direction;

(4) The effect of factors that differ from the simple model of the delay of the propagation of electromagnetic radiation in the interstellar medium on the signal propagation.

CONCLUSIONS

The observations performed on the RT-64 (Kalyazin, Russia) and RT-34 (Kashima, Japan) radio telescopes allowed the spin and astrometric parameters of the millisecond pulsar B1937+21 to be improved over a five-year time interval with allowance made for the variation in DM. The observations with two independent receiving systems yielded a consistent result. The rms value of the TOA residuals does not exceed 1.8 μs over the entire period of observations.

We calculated the variance σ_z^2, which characterizes the fractional instability of the pulsar spin rate. A minimum value of $\sigma_z \approx 2 \times 10^{-14}$ is reached over the entire interval of our simultaneous observations.

Based on the shape of the time dependence of σ_z, we showed that the timing noise is dominated by white phase noise. Thus, a further decrease in σ_z is expected as the duration of the observations increases, which allows us to consider the pulsar as a pulsar time scale keeper on time scales of 10 years or more.

We used the behavior of σ_z to estimate an upper limit for the energy density of the stochastic gravitational wave background, $\Omega_g h^2 \leq 10^{-6}$ at a frequency of $\approx 6.5 \times 10^{-9}$ Hz.

We obtained an accurate value of the dispersion measure toward the pulsar B1937+21 over the entire interval of our simultaneous observations (for epoch MJD = 51000 $DM = 71.0304(1)$) and found it to have decreased at a rate of about $-0.00114(3)$ pc cm^{-3} yr^{-1} in the period 1984–2002.

ACKNOWLEDGMENTS

This work was supported by the Ministry of Education and Science of Russian Federation and by the Russian Foundation for Basic Research (project no. 03-02-16911). Rodin thanks the INTAS for support (grant no. 01-0669).

REFERENCES

1. D. W. Allan, Proc. IEEE **54**, 221 (1966).
2. D. C. Backer, S. Hama, S. van Hook, and R. S. Foster, Astrophys. J. **404**, 636 (1993).
3. D. C. Backer, S. R. Kulkarni, M. M. Davis, and W. M. Goss, Nature **300**, 615 (1982).
4. I. Cognard, G. Bourgois, J.-F. Lestrade, *et al.*, Astron. Astrophys. **296**, 169 (1995).

5. I. Cognard and J.-F. Lestrade, Astron. Astrophys. **323**, 211 (1997).
6. J. M. Cordes and D. R. Stinebring, Astrophys. J. **277**, L53 (1984).
7. J. M. Cordes, A. Wolszczan, R. J. Dewey, *et al.*, Astrophys. J. **349**, 245 (1990).
8. O. V. Doroshenko and S. M. Kopeĭkin, Astron. Zh. **67**, 986 (1990) [Sov. Astron. **34**, 496 (1990)].
9. N. A. Esepkina, Yu. P. Il'yasov, A. P. Lavrov, *et al.,* Pis'ma Zh. Tekh. Fiz. **29**, 32 (2003).
10. Y. Hanado, Y. Shibuya, M. Hosokawa, *et al.*, Publ. Astron. Soc. Jpn. **54**, 305 (2002).
11. V. G. Il'in, Yu. P. Il'yasov, A. D. Kuz'min, *et al.,* Dokl. Akad. Nauk SSSR **275**, 835 (1984).
12. Yu. P. Ilyasov, B. A. Poperechenko, and V. V. Oreshko, Tr. FIAN **229**, 44 (2000).
13. Yu. P. Ilyasov, S. M. Kopeĭkin, and A. E. Rodin, Pis'ma Astron. Zh. **24**, 275 (1998) [Astron. Lett. **24**, 228 (1998)].
14. V. M. Kaspi, J. H. Taylor, and M. F. Ryba, Astrophys. J. **428**, 713 (1994).
15. S. M. Kopeikin, Phys. Rev. D **56**, 4455 (1997).
16. Ch. Lange, N. Wex, and M. Kramer, *IAU Colloq. No. 177: Pulsar Astronomy—2000 and Beyond*, Ed. by M. Kramer, N. Wex, and R. Wielebinski; ASP Conf. Ser. **202**, 117 (2000).
17. J.-F. Lestrade, B. J. Rickett, and I. Cognard, Astron. Astrophys. **334**, 1068 (1998).
18. V. Maitia, J.-F. Lestrade, and I. Cognard, Astrophys. J. **582**, 972 (2003).
19. D. N. Matsakis, J. H. Taylor, and T. M. Eubanks, Astron. Astrophys. **326**, 924 (1997).
20. L. A. Rawley, J. H. Taylor, and M. M. Davis, Astrophys. J. **326**, 947 (1988).
21. E. M. Standish, JPL Interoffice Memorandum IOM 312.F-98-048 (1998).
22. E. M. Standish, X. X. Newhall, J. G. Williams, and W. M. Folkner, JPL Interoffice Memorandum IOM 314.10-127 (1995).
23. J. H. Taylor, Proc. IEEE **79**, 1054 (1991).
24. J. H. Taylor and J. M. Weisberg, Astrophys. J. **345**, 434 (1989).

Translated by A. Dambis

Astronomy Letters, Vol. 31, No. 1, 2005, pp. 37–56. Translated from Pis'ma v Astronomicheskiĭ Zhurnal, Vol. 31, No. 1, 2005, pp. 39–58.

Extreme Vacuum Ultraviolet Solar Spectra Obtained during the SPIRIT Experiment aboard CORONAS-F: A Catalog of Lines in the Range 280–330 Å

I. A. Zhitnik[1], S. V. Kuzin[1], A. M. Urnov[1,2*], I. L. Beigman[1,2], S. A. Bozhenkov[1,2], and I. Yu. Tolstikhina[1]

[1] *Lebedev Institute of Physics, Russian Academy of Sciences, Leninskiĭ pr. 53, Moscow, 119991 Russia*

[2] *Moscow Physicotechnical Institute, Dolgoprudnyi, Moscow oblast, 141700 Russia*

Received June 15, 2004

Abstract—We present a catalog of 100 lines in the wavelength range 280–330 Å detected by the RES-C spectroheliograph in solar active regions and flares during the SPIRIT experiment aboard the CORONAS-F orbital station. We identified 54 lines. The line intensities recorded during the X3.4 (GOES) solar flare of December 28, 2001, are given. The data reduction procedure is discussed. © *2005 Pleiades Publishing, Inc.*

Key words: *CORONAS-F, catalog of lines in solar flares and active regions.*

INTRODUCTION

Extreme vacuum ultraviolet (XUV) solar spectra are of great interest and are widely used to solve many problems in astrophysics and the spectroscopy of multiply charged ions. The spectral range 180–330 Å contains intense ionic lines of almost all of the abundant (in astrophysical plasma) elements excited over a wide temperature range, 10^5–10^7 K. In contrast to X-ray spectra, the XUV spectra of a hot plasma are not affected by nonthermal (beam) electrons due to the relatively low line excitation thresholds and are effectively used to study the differential emission measure (DEM), the abundances of various elements, etc. The sensitivity of the relative intensities of XUV lines to the electron temperature and density allows the plasma structures in the solar atmosphere to be diagnosed (Jordan 1974, 1979; Doschek 1991; Zhitnik *et al.* 1999). This is necessary for modeling its structure and solving fundamental problems: the heating of the solar corona, the origin of the solar wind, etc. Apart from important information about the energy accumulation, transfer, and release, high-resolution spectra for the coronal plasma of active regions and flares also make it possible to experimentally refine the wavelengths and to identify the lines that correspond to both optically allowed and forbidden transitions in multiply charged ions. Elucidating the physical conditions for the generation of solar XUV lines and compiling the catalogs of these lines are inextricably linked with one another and represent two aspects of the same problem aimed at studying their excitation mechanism under typical conditions in the solar atmosphere. By now, a series of catalogs have been compiled using spectra both from the full solar disk (Malinovsky and Heroux 1973; Behring *et al.* 1972, 1976) and from separate areas of the quiet corona (Brooks *et al.* 1999) and active regions under flareless conditions (Thomas and Neupert 1994; Brosius *et al.* 1998, 2000). The published spectroscopic data on solar flares are much more scarce. Observational spectra are difficult to obtain for solar flares, because these events are relatively rare and because the size of the source is small. Regular observations with a wide-field instrument are required to obtain them. The main source of information about flare lines is the catalog compiled from the measurements performed with the S 80A spectroheliograph aboard the Skylab station (Dere 1978). This instrument recorded the spectral images of the Sun with high spatial (2″) and spectral (0.1 Å) resolutions. However, the large size of the Sun, which was 25 Å on the wavelength scale, led to an overlap of the spectral images and made it difficult to restore the spectra.

Regular observations of the full solar disk in monochromatic XUV spectral lines were performed with the RES-C spectroheliograph aboard CORONAS-I in 1994 (Sobel'man *et al.* 1996). A catalog of coronal plasma lines in the wavelength range 177–207 Å was compiled from these observations (Zhitnik *et al.* 1998), and a procedure for

* E-mail: urnov@sci.lebedev.ru

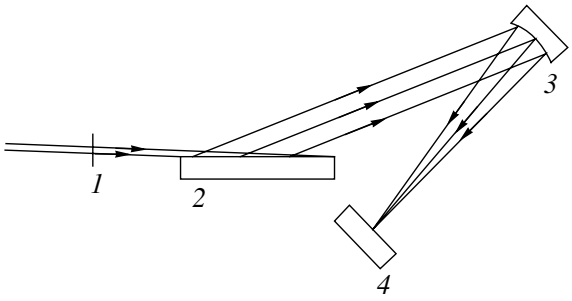

Fig. 1. Optical scheme of the spectroheliograph: (*1*) entrance filter, (*2*) diffraction grating, (*3*) multilayer X-ray mirror, and (*4*) detector.

determining the physical plasma parameters using these data was presented (Zhitnik *et al.* 1999). An outgrowth of this instrument is the XUV spectroheliograph for the wavelength ranges 180–210 and 280–330 Å that was part of the SPIRIT instrumentation aboard CORONAS-F (Oraevskiĭ and Sobel'man 2002). This station was placed in a near-Earth polar orbit with a height of ~500 km on July 31, 2001. Apart from the spectroheliograph, the SPIRIT instrumentation includes XUV telescopes for the wavelength range (171, 175, 195, 285, 304 Å) and a spectroheliometer to record the solar images in the Mg XII 8.42 Å line (Zhitnik *et al.* 2002). Regular SPIRIT observations began in August 2001 during the maximum of the solar cycle 23. More than 300 000 soft X-ray and XUV images and spectroheliograms of the Sun, including more than 1000 XUV spectroheliograms, have been obtained to date. In this paper, we analyze the spectra of solar flares and other active structures in the solar atmosphere taken with the RES-C spectroheliograph as part of the SPIRIT experiment. This instrument can simultaneously obtain about 150 images of the entire Sun in individual monochromatic lines in two spectral ranges: 180–210 and 280–330 Å. We present a complete catalog of lines in the range 280–330 Å that was compiled from the observations of the active region NOAA 9765 and the X3.4 solar flare of December 28, 2001 (20:02–21:32) (GOES). The spectrum of the flare was taken at 21:21:44 on December 28, 2001; the spectra of the active region were taken at the following times: 14:38:11 on December 29, 2001; 16:16:43 on December 29, 2001; and 04:52:44 on December 30, 2001. The exposure time for all of the frames used was 37 s. The lines recorded only during the flare are marked separately in the catalog. The relative line intensities and widths are given for the X3.4 flare of December 28, 2001. The spectroheliogram reduction procedures, including the wavelength and spectral sensitivity calibration, the analysis of the wavelength measurement accuracy, and the line identification procedure based on analysis of the relative line intensities of the multiplet structure, are described.

DESCRIPTION OF THE INSTRUMENT

The spectroheliograph was a slitless spectrometer with a flat objective reflecting diffraction grating at the entrance (Fig. 1). The grating was set at a small grazing angle, 1°–2°, which led to the "spectral compression" of the angular aperture of the Sun in the diffracted emission of an individual spectral line: the angular size of the image in the dispersion direction decreased proportionally to the ratio of the sines of the grazing and diffraction angles. The emission diffracted on the grating was focused by a normal-incidence multilayer mirror on the sensitive area of an imaging detector. Characteristics of the main optical elements used in the XUV RES-C spectroheliograph are given in Table 1.

The calibration procedure for the main optical elements and the entire spectroheliograph was described in detail by Kuzin *et al.* (1997).

DATA REDUCTION AND CALIBRATION

The spectroheliogram was a sequence of monochromatic images of the full Sun compressed in the dispersion direction. The initial spectroheliogram is illustrated by Fig. 2a. The data reduction procedure consisted in subtracting the background, constructing the one-dimensional spectrum, determining the observed line parameters, and calibrating the wavelengths and the spectral sensitivity of the instrument. The background intensity at observed peak line intensities from 20 to 16 000 counts was 50–300 counts and exhibited a significant gradient (below, counts are designated as arbitrary units). The background subtraction algorithm was refined on a large number of frames; the error of the algorithm was ~5 counts. The spectroheliograms before and after the background subtraction are compared in Fig. 2.

Constructing the One-dimensional Spectrum

The spectrum is a one-dimensional section of the spectroheliogram in the dispersion direction. The dispersion direction of the instrument does not coincide with the CCD rows. The slope is $\alpha = 27\overset{\circ}{.}63 \pm 0\overset{\circ}{.}02$, which corresponds to $\tan\alpha = 0.5234 \pm 0.0004$. The measurement error of the tangent allows the relative position of the region under study on the solar disk at the opposite ends of the spectroheliogram to be determined with an accuracy higher than $7''$. The position of a point on the dispersion axis is determined

Table 1. Elements of the spectroheliograph

Range	176–207 Å	280–330 Å
Diffraction grating		
Line frequency, lines mm^{-1}	3600	
Grazing angle, deg	1.2	1.4
Multilayer mirror		
Mirror shape	Sphere	Paraboloid
Focal length, mm	830	570
Coating	Mo–Si	
Peak reflectance, %	30	23
Entrance filter		
Material	Al 0.15 ± 0.05 μm in thickness	
Transmission in working range, %	12	11
Detector. Image tube (IT) with open solar-blind MCP + electrically cooled CCD array		
IT photocathode	MgF_2	
IT amplification	up to 10^5	
Number of CCD pixels	1024×1152	
Input pixel size, μm	20.8×20.8	
ADC width, bit	14	
Readout time, s	2	

by both the wavelength and the geometrical position on the Sun. However, the geometrical position is unimportant if the size of the emitting region $\leq \frac{1}{5} R_\odot$ (a flare or an active region). The size of the region in the image is smaller than the point spread function of the instrument due to the compression; i.e., the distance along the dispersion direction corresponds to the wavelength. The spectroheliogram compression in the dispersion direction causes the spectrum to be averaged over the extent of the region along the dispersion axis. For the spectra used here, the contribution of nearby regions is negligible, since for our analysis we selected regions close to or above the limb at the upper and lower edges of the spectroheliograms. All of the spectra used were averaged in a direction perpendicular to the dispersion axis over five pixels; one pixel corresponds to about 7″ on the solar disk, and the point spread function of the instrument is two pixels in width. As an example, Fig. 3 shows the position of the December 28, 2001 flare on the solar disk, the height at which the spectrum is viewed, and the spectrum averaging region.

Determining the Line Parameters

To determine the line positions and intensities, we used a method of fitting the emission intensity in the chosen narrow part of the spectrum by taking into account the expected number of lines and the local background. The latter may be represented as a constant or a linear function after the removal of the main

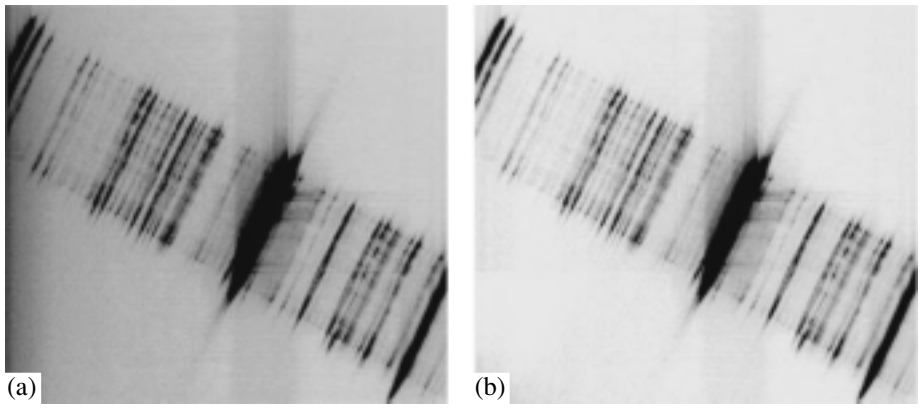

Fig. 2. Comparison of the spectroheliograms before and after applying the background subtraction procedure: (a) initial spectroheliogram; (b) reduced spectroheliogram.

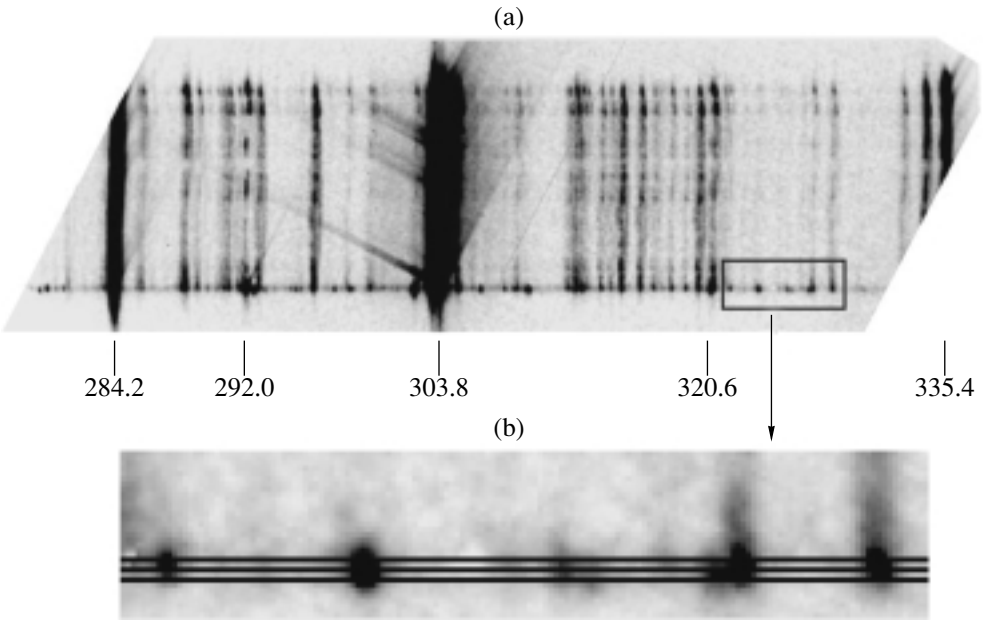

Fig. 3. (a) Position of the December 28, 2001 flare on the solar disk. The bright pointlike areas at the lower limb correspond to the flare images in individual lines. The rectangle highlights the region that is shown below on an enlarged scale. (b) The highlighted region of the spectrum: the middle straight line indicates the center of the flare; the upper and lower straight lines indicate the region of the spectrum averaging perpendicular to the dispersion axis, and the bright regions are the flare images.

gradients. The method proved an exceptionally useful tool for analyzing strongly blended spectra (Brooks *et al.* 1999; Thomas and Neupert 1994; Lang *et al.* 1990; Brosius *et al.* 1998, 2000). The line shape was assumed to be Gaussian. The parameters included the peak line intensities, widths, and positions. The lines were fitted by the χ^2 method (see, e.g., Press *et al.* 2001; Brandt 2003). The error distribution was assumed to be normal; the standard deviation for each point was given by the Poisson formula: $\sigma_i^I = \sqrt{I_i}$, where I_i is the intensity of point i. This method also allows the errors in the parameters to be estimated and yields an estimate for the quality of the fit. An example of a fit is shown in Fig. 4.

In most cases, the error in the peak intensity is determined precisely by the fitting procedure, despite the error introduced at the background subtraction step and the presence of detector noise. For some of the lines, the error can be slightly larger than that determined from the confidence interval, because the profile must be determined in narrow segments where the behavior of the background cannot always be predicted unambiguously. An analysis of the dependence of the line width on its position in the spectrum (Fig. 5) shows that the width in the interval under

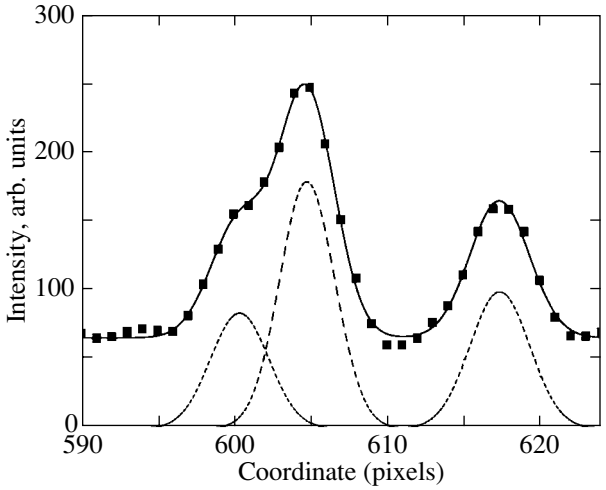

Fig. 4. An example of fitting the emission profile by minimizing the χ^2 value, $\chi^2 = 0.19$. The squares indicate the experimental data. The dashed curves represent three separate lines, and the solid curve represents the combined fit.

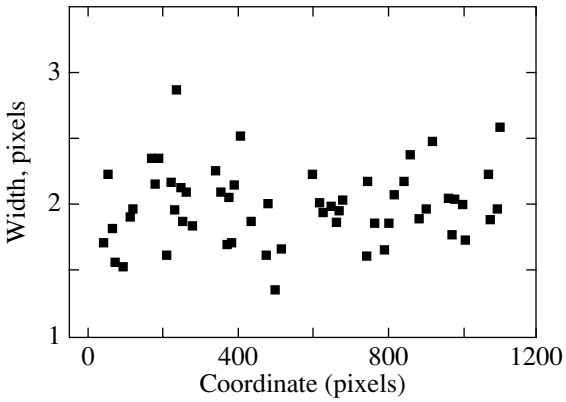

Fig. 5. Line width versus position in the spectrum.

consideration is almost constant and is determined by the point spread function and the Doppler broadening. The Doppler broadening is given by

$$\sigma_{\rm Dop} = \frac{\lambda}{c}\left(\frac{2kT}{M}\right)^{1/2}. \quad (1)$$

For an iron ion at temperature $T = 10^7$ K and $\lambda = 300$ Å, the Doppler width is $\sigma_{\rm Dop} \approx 0.05$ Å. The mean line width in the experimental spectrum is $\sigma \approx 0.1$ Å. Thus, the width is determined mainly by the point spread function. The total line flux is

$$I = \sqrt{2\pi}\sigma A, \quad (2)$$

where A is the peak line intensity. Since the line widths are constant, we compare below the peak intensities rather than the total fluxes.

Determining the Wavelengths

Based on reference lines, we calibrated the wavelength scale of the instrument using a quadratic polynomial. The sufficiency of the quadratic polynomial was checked in a geometrical model of the instrument. As the reference lines, we chose the lines that satisfied the following criteria: a sufficient intensity, observability in previous experiments, a high accuracy of determining the position, and coverage of the entire range by a complete set of lines.

We selected the following reference lines:

288.17 (Ni XVI $3s^2 3p \quad {}^2P_{1/2} - 3s3p^2 \quad {}^2D_{3/2}$),

288.42 (S XII $2s^2 2p \quad {}^2P_{1/2} - 2s2p^2 \quad {}^2D_{3/2}$),

291.98 (Ni XVIII $3s \quad {}^2S_{1/2} - 3p \quad {}^2P_{3/2}$),

315.02 (Mg VIII $2s^2 2p \quad {}^2P_{3/2} - 2s2p^2 \quad {}^2P_{3/2}$),

319.84 (Si VIII $2s^2 2p^3 \quad {}^4S_{3/2} - 2s2p^4 \quad {}^4P_{5/2}$),

327.03 (Fe XV $3s3p \quad {}^3P_2 - 3p^2 \quad {}^1D_2$).

The resulting polynomial is

$$\lambda = 262.571 + 0.043049P + 1.600 \times 10^{-6}P^2, \quad (3)$$

where P is the coordinate in pixels, and λ is the wavelength in Å. The calibration accuracy was checked by comparing the measured wavelengths with the wavelengths from the CHIANTI database for all of the reliably identified lines. We see from Fig. 6 that the difference does not exceed ±0.040 Å almost for all of the lines except the line corresponding to the Fe XIII $3s^2 3p^2 \, {}^3P_1 - 3s3p^3 \, {}^3P_1$ transition (the CHIANTI wavelength is 312.11 Å). The measured wavelength turns out to be closer to 312.2 Å, in agreement with the wavelength of 312.17 Å given by Thomas and Neupert (1994), within the adopted error limits of 40 mÅ.

Calibrating the Spectral Sensitivity of the Instrument

The wavelength dependence of the multilayer mirror reflectance makes a major contribution to the spectral sensitivity. When calibrating the instrument, we measured the angular dependence of the mirror reflectance at a fixed wavelength. The angular dependence was recalculated to the wavelength dependence using the Bragg condition

$$2d\cos\alpha = m\lambda,$$

where d is the period of the multilayer structure, m is the order of interference, and α is the angle of incidence. The recalculation result is shown in Fig. 7.

To check the calibration, we used the intensity ratios of the lines with a common upper transition

Table 2. Checking the calibration of the instrument

Lines	Without calibration	With calibration	Theory	Relative
Fe XIII 312.11/321.40	3.09 ± 0.11	2.42 ± 0.09	1.94	1.25 ± 0.05
Fe XIII 311.55/320.81	0.23 ± 0.02	0.18 ± 0.02	0.13	1.38 ± 0.15
Mg VIII 317.03/313.74	0.63 ± 0.03	0.67 ± 0.03	0.71	0.94 ± 0.04
Si VIII 314.36/319.84	0.36 ± 0.01	0.31 ± 0.01	0.35	0.89 ± 0.03
Si VIII 316.22/319.84	0.84 ± 0.02	0.75 ± 0.02	0.66	1.14 ± 0.03
S XI 285.59/281.40	0.73 ± 0.08	0.61 ± 0.07	0.49	1.24 ± 0.14
S XII 288.42/299.78	7.27 ± 0.45	8.61 ± 0.53	9.26	0.93 ± 0.06
Fe XV 327.03/312.57b	0.75 ± 0.03	1.22 ± 0.05	1.81	0.67 ± 0.03
Fe XV 307.75/321.77	1.04 ± 0.05	0.79 ± 0.04	0.69	1.14 ± 0.06
Fe XV 292.28/304.89b	0.26 ± 0.01	0.28 ± 0.01	0.35	0.80 ± 0.03
Ni XVIII 291.98/320.57	2.62 ± 0.16	2.24 ± 0.12	2.00	1.12 ± 0.06

Note. Lines—the intensity ratio under consideration; without calibration—the intensity ratio without the calibration factors; with calibration—the intensity ratio with the calibration factors; theory—the theoretical intensity ratio; relative—the experimental intensity ratio with the calibration factor (the column "With calibration") divided by the theoretical value (the column "Theory"); b—the line is blended.

level or other ratios that do not depend on the emitting plasma parameters. The results are summarized in Table 2. With the exception of the ratios that include blended lines, the experimental values agree with the theoretical values within 3σ, which corresponds to a calibration accuracy of about 20%.

RESULTS AND DISCUSSION

The identification was based on the following criteria:

(1) The coincidence of wavelengths with previously measured ones. The CHIANTI database was used as the source of wavelengths.

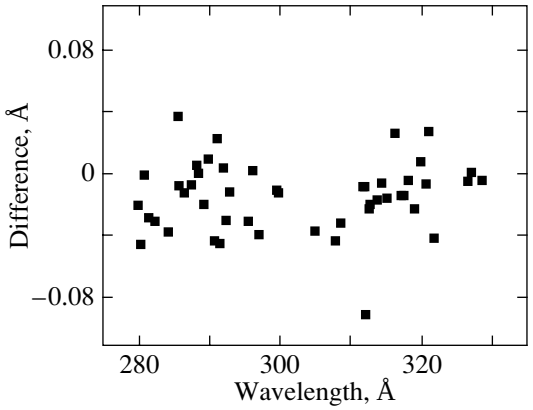

Fig. 6. Difference between the experimental and theoretical wavelengths for the December 28, 2001, flare.

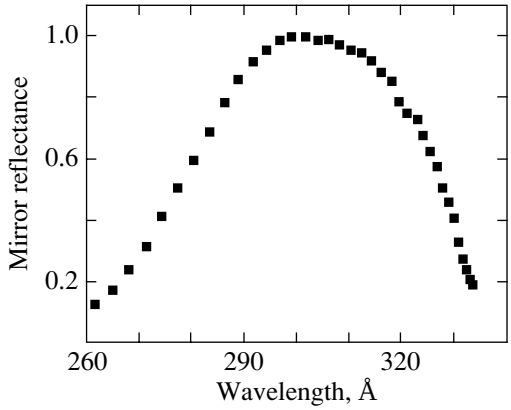

Fig. 7. Relative reflectance of the multilayer mirror versus wavelength.

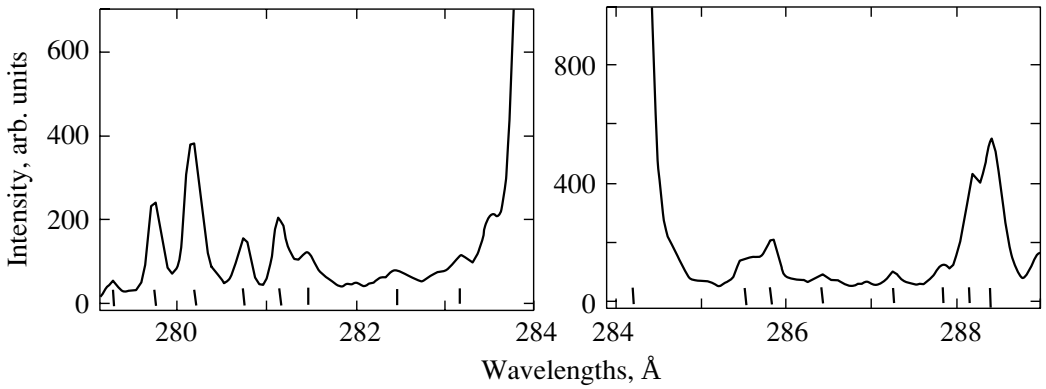

Fig. 8. Spectrum of the December 28, 2001, flare. The vertical bars mark the lines included in Table 3.

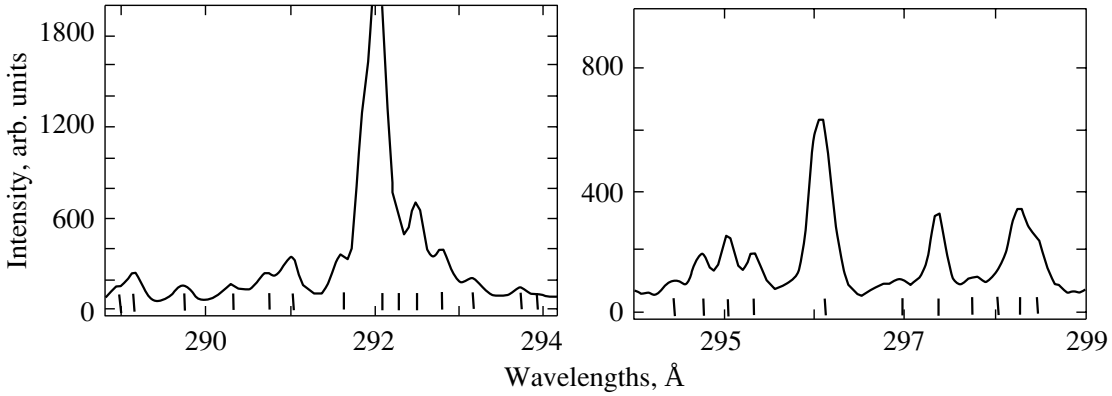

Fig. 9. Spectrum of the December 28, 2001, flare (the continuation of Fig. 8).

(2) The presence of multiplet lines in the experimental spectrum.

(3) The match between the experimental and theoretical intensity ratios of the lines with a common upper level.

In several cases where criteria 2 and 3 could not be used, we compared the line intensities in various areas on the Sun (flares, active regions, the quiet Sun) and the intensities of the lines belonging to the same isoelectronic sequence. In addition, we imposed the requirement on each line that it exceeded in amplitude a 3σ noise level ($\sim$10 counts).

The spectrum is shown in Figs. 8–14; the observed lines are marked by vertical bars. The identification results are presented in Table. 3. This table contains the following information: the line numbers; the measured wavelengths, the peak line intensities with errors and relative calibration of the instrument, the line widths with errors, the identified ions, the fractional parts of the CHIANTI wavelengths of the identified lines, the fractional parts of the line wavelengths from the spectral catalog of a flare (Dere 1978), the fractional parts of the line wavelengths from the spectral catalog of an active region by Thomas and Neupert (1994), and the fractional parts of the line wavelengths from the spectral catalog of an active region by Brosius *et al.* (2000); the lines observed only in the flare spectra are marked by "†." Below, we comment on the line identification with an indication of the transitions considered. The ions are arranged in order of increasing atomic number of the element and charge. For each ion, we gives the temperature of the maximum ion abundance (CHIANTI) and the terms between which the transitions are observed. The multiplet structure is presented in the form of tables that list the total angular momenta of the transitions and the corresponding CHIANTI wavelengths. When comparing the experimental line intensity ratios that are insensitive to the plasma parameters, we used the spectra of the December 28, 2001, flare and the limb active regions: at 14:38:11 on December 29, 2001; at 16:16:43 on December 29, 2001; and at 04:52:44 on December 30, 2001. In several cases, we compare the intensities of the line under discussion in the December 28, 2001, flare and in the

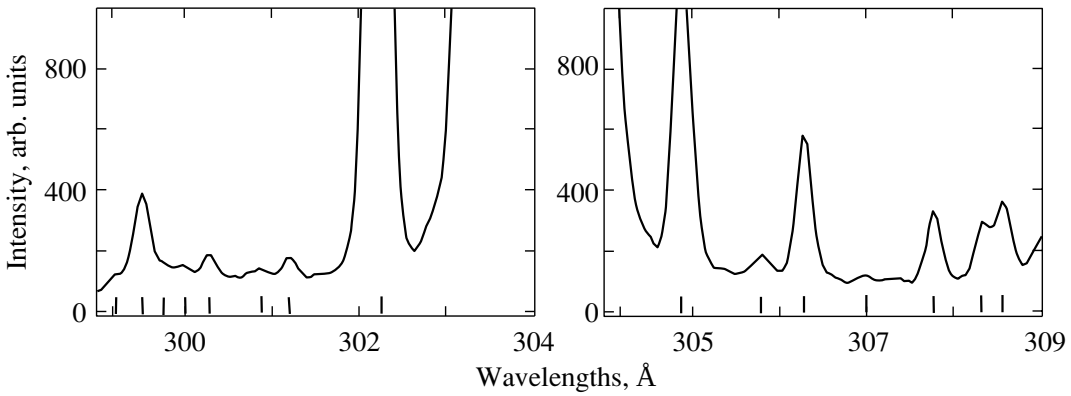

Fig. 10. Spectrum of the December 28, 2001, flare (the continuation of Fig. 9).

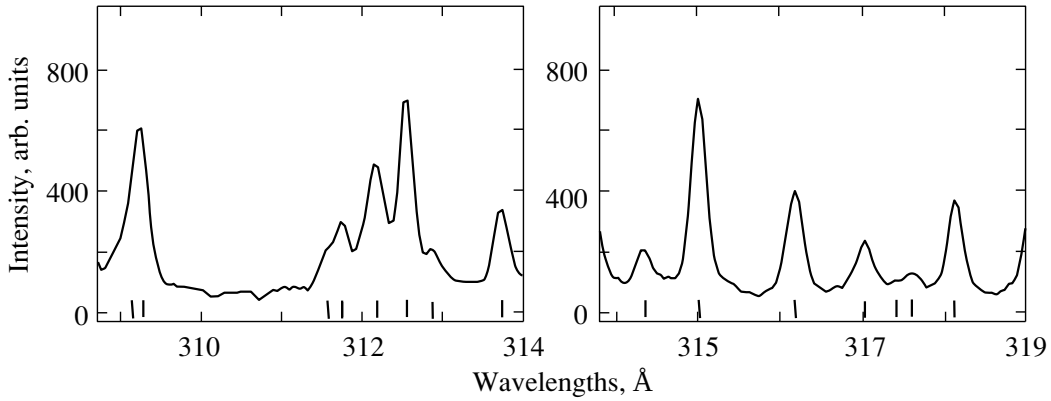

Fig. 11. Spectrum of the December 28, 2001, flare (the continuation of Fig. 10).

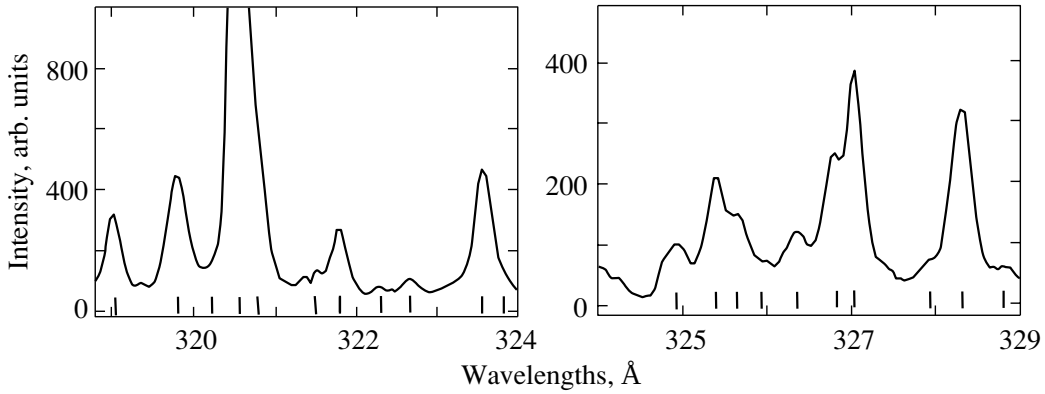

Fig. 12. Spectrum of the December 28, 2001, flare (the continuation of Fig. 11).

active region observed at 14:38:11 on December 29, 2001. Below, the following notation is used: "+"—the line is observed; "–"—the line is not observed; "b"—the line is blended; "l"—the line does not fall within the recorded wavelength range 279–330 Å; "u"—there are questions in the line identification that are discussed in the text.

He II ($\log T = 4.9$). $1s\,^2S - 2p\,^2P$.

$J_{\rm low} - J_{\rm up}$	λ, Å	Note
$1/2 - 1/2$	303.79	$+b$
$1/2 - 3/2$	303.78	$+b$

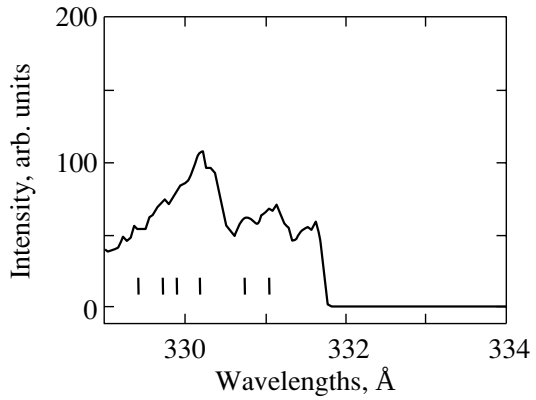

Fig. 13. Spectrum of the December 28, 2001, flare (the continuation of Fig. 12).

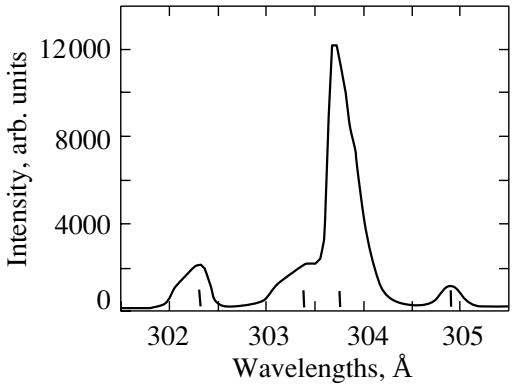

Fig. 14. Spectrum of the December 28, 2001, flare in the region of the resonance HeII line.

The doublet is not resolved. Since the image of the solar disk is very intense in the helium line, only the peak intensity was determined for it.

C IV ($\log T = 5.1$). $1s^2 2p\,^2P - 1s^2 4s\,^2S$.

$J_{\rm low} - J_{\rm up}$	λ, Å	Note
$1/2 - 1/2$	296.86	$+b$
$3/2 - 1/2$	296.91	$+b$

The doublet is not resolved, which leads to a large line width.

Mg VII ($\log T = 5.8$). $2s^2 2p^2\,{}^1D_2 - 2s2p^3\,{}^1D_2$.

The 319.02 Å line is blended with the Ni XV $3s^2 3p^2\,{}^3P_2 - 3s3p^3\,{}^3D_3$ line.

$2s^2 2p^2\,{}^1D_2 - 2s2p^3\,{}^1P_1$. The 280.74 Å line.

$2s^2 2p^2\,{}^1S_0 - 2s2p^3\,{}^1P_1$. The 320.52 Å line is blended with the Ni XVIII $3s\,^2S_{1/2} - 3p\,^2P_{1/2}$ line. The upper level of the $2s^2 2p^2\,{}^1S_0 - 2s2p^3\,{}^1P_1$ transition coincides with the upper level of the $2s^2 2p^2\,{}^1D_2 - 2s2p^3\,{}^1P_1$ (280.74 Å) transition. The intensity of the Mg VII 320.52 Å line was estimated from the intensity of the Mg VII 280.74 Å line and the branching ratio (CHIANTI):

$$I_{\rm Mg\,VII}(320.52) = 0.20 I_{\rm Mg\,VII}(280.74) = 38 \pm 3.$$

The total line intensity is $I_{\rm total}(320.52) = 1828 \pm 261$. The contribution of the Mg VII $2s^2 2p^2\,{}^1S_0 - 2s2p^3\,{}^1P_1$ transition to the total intensity is about 2% and is less than the measurement error of the total intensity. Therefore, the 320.52 Å line was identified as Ni XVIII $3s^2 S_{1/2} - 3p^2 P_{1/2}$.

Mg VIII ($\log T = 5.9$). $2s^2 2p\,^2P - 2s2p^2\,^2P$.

$J_{\rm low} - J_{\rm up}$	λ, Å	Note
$1/2 - 1/2$	313.74	+
$3/2 - 1/2$	317.03	+
$1/2 - 3/2$	311.77	+b
$3/2 - 3/2$	315.02	+

All multiplet components are observed. The Mg VIII 311.77 Å line is blended with the Ni XV $3s^2 3p^2\,{}^3P_1 - 3s3p^3\,{}^3D_2$ 311.76 Å line. The blending is confirmed by the difference between the experimental and theoretical intensity ratios $I(311.77)/I(315.02)$ by a factor of 1.6 (Table 4). The intensity of the blending line was estimated from the intensity of the Mg VIII 315.02 Å line and the branching ratio (CHIANTI):

$$I_{\rm NiXV}(311.77) = I_{\rm total}(311.77) - 0.19 I_{\rm MgVIII}(315.02) = 87 \pm 6.$$

The experimental intensity ratio $I(317.03)/I(313.74)$ is equal to its theoretical value within 1.33σ (Table 4).

Al VII ($\log T = 5.8$). $2s^2 2p^3\,{}^2D - 2s2p^4\,{}^2D$.

$J_{\rm low} - J_{\rm up}$	λ, Å	Note
$3/2 - 3/2$	309.02	+bu
$5/2 - 3/2$	309.09	+bu
$3/2 - 5/2$	309.06	+bu
$5/2 - 5/2$	309.13	+bu

The lines of this multiplet could have contributed to the observed unidentified 309.14 Å line.

Table 3. Parameters of the observed lines

N	λ, Å	*A*, arb. units	σ, pixels	Ion	λ_C, Å	I	II	III
1	279.27	50 ± 12	0.96 ± 0.26	...	...	0.21	...	–
2	279.76†	365 ± 17	1.76 ± 0.07	Cr XXII	0.74	0.70	...	–
3	280.19†	576 ± 19	2.22 ± 0.06	Fe XVII	0.14	0.14	...	–
	〃	〃	〃	Al IX	0.14	〃	〃	–
4	280.74	188 ± 13	1.74 ± 0.11	Mg VII	0.74	0.74	0.75	–
5	281.14†	259 ± 18	1.60 ± 0.11	...	0.09	...	...	–
6	281.43	121 ± 10	2.95 ± 0.38	S XI	0.40	0.42	0.44	–
7	282.45	42 ± 8	2.68 ± 0.70	Al IX	0.42	...	0.43	–
8	283.17	34 ± 15	1.33 ± 0.70	...	...	...	0.15	–
9	284.20	$13\,696 \pm 140$	$... \pm ...$	Fe XV	0.16	0.17	0.16	–
10	285.55	118 ± 11	2.33 ± 0.35	S XI	0.59	0.57	0.58	–
11	285.83	179 ± 12	2.08 ± 0.21	S XI	0.82	0.83	0.83	–
12	286.43	30 ± 9	1.91 ± 0.64	Fe XVII	0.42	...	...	–
	〃	〃	〃	AlIX	0.38	〃	〃	–
13	287.27	52 ± 9	1.55 ± 0.30	Fe XII	0.26	0.23	...	–
14	287.86	72 ± 8	2.11 ± 0.45	...	...	0.23	...	–
15	288.16	321 ± 29	1.97 ± 0.23	Ni XVI	0.17	0.14	0.16	–
16	288.42	546 ± 18	2.83 ± 0.16	S XII	0.42	0.40	0.40	–
17	288.96†	99 ± 17	1.92 ± 0.47	...	...	...	...	–
18	289.17	214 ± 19	1.95 ± 0.23	Fe XIV	0.15	0.15	0.17	–
19	289.74	116 ± 9	2.08 ± 0.21	Cr XIV	0.75	0.72	...	–
	〃	〃	〃	Mn XIII	0.72	〃	〃	–
20	290.32	110 ± 8	2.60 ± 0.30	...	...	...	...	–
21	290.73	194 ± 10	2.92 ± 0.49	Si IX	0.69	0.71	0.69	–
22	291.03	298 ± 20	2.10 ± 0.18	Fe XII	0.05	0.00	0.01	–
23	291.61	290 ± 13	2.07 ± 0.17	S XI	0.58	...	...	–
24	291.98	4605 ± 433	$... \pm ...$	Ni XVIII	0.98	0.98	0.99	–
25	292.31	357 ± 55	1.04 ± 0.18	Fe XV	0.28	0.26	0.31	–
26	292.51†	651 ± 18	2.14 ± 0.19	Fe XXII	0.49	0.48	...	–
27	292.82	311 ± 14	2.42 ± 0.26	Si IX	0.81	0.79	0.80	–
28	293.17	117 ± 10	2.13 ± 0.27	Cr XXI	0.11	0.15	...	–
29	293.75	54 ± 9	1.56 ± 0.48	...	...	0.78	...	–
30	293.94	17 ± 8	1.36 ± 1.12	...	...	...	...	–
31	294.46	47 ± 8	1.84 ± 0.47	...	...	0.47	...	–
32	294.78	137 ± 10	2.08 ± 0.26	...	...	0.72	...	–
33	295.07	199 ± 11	1.73 ± 0.18	...	...	0.01	...	–
34	295.32	136 ± 9	2.16 ± 0.24	...	...	...	...	–
35	296.11	586 ± 13	2.62 ± 0.05	Si IX	0.11	0.12	0.14	–
	〃	〃	〃	Si IX	0.21	〃	〃	–
36	296.99	46 ± 5	4.39 ± 0.80	C IV	0.86	...	...	–
	〃	〃	〃	CIV	0.95	...	...	–
37	297.39†	257 ± 12	1.91 ± 0.10	...	...	0.34	...	–
38	297.78†	52 ± 7	2.38 ± 0.79	...	...	...	...	–

Table 3. (Contd.)

N	λ, Å	A, arb. units	σ, pixels	Ion	λ_C, Å	I	II	III
39	298.10	75 ± 62	2.04 ± 1.95	Ni XV	0.15	...	0.12	–
40	298.27	218 ± 133	1.75 ± 0.76	...	...	...	0.20	–
41	298.46	176 ± 44	2.54 ± 0.62	...	...	...	...	–
42	299.28	60 ± 10	2.35 ± 0.78	...	...	...	...	–
43	299.55	300 ± 13	2.07 ± 0.25	S XII	0.54	0.50	0.53	0.55
44	299.79	71 ± 44	1.48 ± 0.80	S XII	0.78	...	...	...
45	300.00	90 ± 10	2.47 ± 1.45	...	...	...	...	...
46	300.32	121 ± 11	2.23 ± 0.52	...	...	...	0.25	...
47	300.89	22 ± 8	1.99 ± 0.90	...	...	...	...	...
48	301.23†	62 ± 10	1.55 ± 0.29	...	...	...	...	...
49	302.2	3212 ± 301	... ± ...	Ca XVIII	0.19	0.21	0.17	0.32
50	303.4	1614 ± 303	... ± ...	Si XI	0.33	0.33	0.32	0.32
51	303.8	$16\,468 \pm 505$	... ± ...	He II	0.78	0.79	0.78	0.79
52	304.93	972 ± 19	2.18 ± 0.43	Fe XV	0.89	0.80	0.87	0.87
53	305.83	60 ± 9	2.01 ± 0.39	...	...	...	0.84	0.79
54	306.32†	448 ± 15	1.93 ± 0.06	...	...	0.29	...	...
55	307.00†	24 ± 11	1.64 ± 0.90	...	...	...	...	0.97
56	307.79	227 ± 14	1.87 ± 0.14	Fe XV	0.75	0.76	...	0.76
57	308.34	181 ± 15	1.81 ± 0.22	...	...	...	...	...
58	308.58	250 ± 12	2.05 ± 0.21	Fe XI	0.55	0.54	0.58	0.55
59	309.14	194 ± 30	4.07 ± 0.38	...	...	...	0.21	0.23
60	309.29†	395 ± 38	1.87 ± 0.15	...	0.24	...	...	...
61	311.56	95 ± 28	1.60 ± 0.40	Fe XIII	0.55	...	0.56	0.58
62	311.78	121 ± 3*	2.16 ± 0.39	Mg VIII	0.77	0.74	0.78	0.77
	〃	87 ± 6*	〃	Ni XV	0.76	〃	〃	〃
63	312.20	402 ± 14	2.91 ± 0.16	Fe XIII	0.11	0.18	0.17	0.17
64	312.58	315 ± 32*	1.84 ± 0.08	Fe XV	0.56	0.57	0.55	0.57
	〃	319 ± 37*	〃	Co XVII	0.54	...	...	...
65	312.89	107 ± 8	2.68 ± 0.42	Fe XIII	0.87	...	0.87	0.90
66	313.76	288 ± 13	2.16 ± 0.10	Mg VIII	0.74	0.74	0.74	0.73
67	314.36	110 ± 11	1.77 ± 0.22	Si VIII	0.36	0.31	0.36	0.36
68	315.03	636 ± 18	1.98 ± 0.05	Mg VIII	0.02	0.02	0.02	0.02
69	316.19	359 ± 12	2.18 ± 0.08	Si VIII	0.22	0.19	0.22	0.21
70	317.04	170 ± 10	2.45 ± 0.17	Mg VIII	0.03	0.02	0.01	0.02
71	317.38	30 ± 15	1.89 ± 1.55	...	...	...	...	0.48
72	317.61	63 ± 16	1.94 ± 0.67	Fe XV	0.60	0.61	...	0.64

Table 3. (Contd.)

N	λ, Å	A, arb. units	σ, pixels	Ion	λ_C, Å	I	II	III
73	318.13	331 ± 14	1.99 ± 0.08	Fe XIII	0.13	0.12	0.12	0.13
74	319.04	288 ± 13	1.96 ± 0.15	Ni XV	0.06	0.03	0.02	0.03
	〃	〃	〃	Mg VII	0.02	〃	〃	〃
75	319.83	453 ± 14	2.48 ± 0.10	Si VIII	0.84	0.84	0.84	0.84
76	320.20	75 ± 12	1.71 ± 0.61	...	...	...	...	0.25
77	320.57	1828 ± 261	... ± ...	Ni XVIII	0.57	0.55	0.56	0.56
78	320.78	585 ± 258	2.59 ± 0.45	Fe XIII	0.81	0.80	0.80	0.81
79	321.50	... ± ...	... ± ...	Fe XIII	0.40	0.47	0.46	0.48
80	321.81	274 ± 13	2.10 ± 0.14	Fe XV	0.77	0.78	0.78	0.79
81	322.30	24 ± 11	1.20 ± 0.62	...	...	...	...	...
82	322.68	57 ± 10	1.84 ± 0.37	...	...	0.72	0.70	0.73
83	323.59†	557 ± 20	2.29 ± 0.10	...	...	0.57	...	...
84	323.86	62 ± 14	1.41 ± 0.46	...	...	0.85	...	...
85	324.91	133 ± 8	2.85 ± 0.23	Fe XV	0.98	0.97	...	0.98
86	325.40†	279 ± 14	2.72 ± 0.32	...	...	0.40	0.42	0.39
87	325.68†	156 ± 37	1.86 ± 0.59	...	...	...	...	0.78
88	325.91	62 ± 20	2.28 ± 1.03	...	...	...	...	...
89	326.35	129 ± 12	3.40 ± 0.49	...	...	0.36	0.35	0.32
90	326.78†	346 ± 22	2.33 ± 0.36	...	...	0.80	...	...
91	327.03	572 ± 58	1.84 ± 0.23	Fe XV	0.03	0.03	0.03	0.03
92	327.90	55 ± 12	1.94 ± 0.61	...	...	0.86	...	0.85
93	328.27	571 ± 20	2.58 ± 0.10	Cr XIII	0.27	0.26	0.26	0.26
94	328.74	40 ± 10	2.21 ± 0.77	...	...	...	...	0.75
95	329.43	31 ± 29	3.26 ± 5.00	...	...	...	...	...
96	329.70	60 ± 69	2.11 ± 3.96	...	...	...	...	...
97	329.92	59 ± 102	1.94 ± 2.53	...	...	0.92	...	0.92
98	330.22	158 ± 18	3.55 ± 0.86	...	...	0.17	...	0.22
99	330.75	48 ± 17	1.61 ± 0.84	...	...	...	...	...
100	331.07	73 ± 18	2.78 ± 1.25	...	...	0.03	0.07	0.99

Note. N is the line number; λ is the experimental wavelength; A is the peak line intensity with its error; σ is the line width with its error; Ion denotes the identified ion; λ_C is the fractional part of the wavelength of the identified line from the CHIANTI database; I is the fractional part of the line wavelength from the spectral catalog of a flare by Dere (1978); II is the fractional part of the line wavelength from the spectral catalog of an active region by Thomas and Neupert (1994); III is the fractional part of the line wavelength from the spectral catalog of an active region by Brosius *et al.* (2000); † denotes the lines that are clearly observable only in the flare spectra; * is the intensities of the blended lines estimated from the branching ratios (for a further explanation, see the text).

Table 4. Checking the Mg VIII identification using SPIRIT data

Ratio	1	2	3	4	Mean	Theory
311.77/315.02	0.32	0.33	0.33	0.29	0.32	0.19
σ	0.02	0.02	0.02	0.02	0.01	
317.03/313.74	0.68	0.63	0.68	0.66	0.67	0.71
σ	0.10	0.07	0.04	0.05	0.03	

Note: 1—The flare of December 28, 2001; 2—the active region observed at 14:38:11 on December 29, 2001; 3—the active region observed at 16:16:43 on December 29, 2001; 4—the active region observed at 04:52:44 on December 30, 2001; mean—the value obtained by averaging 1–4 values; theory—the theoretical ratio based on CHIANTI data.

Table 5. Checking the Al IX identification using SPIRIT data

Ratio	1	2	3	4	Mean	Theory
286.38/282.42	0.71	0.88	0.81	1.57	0.86	0.81
σ	0.25	0.25	0.21	0.49	0.13	

Note: 1—The flare of December 28, 2001; 2—the active region observed at 14:38:11 on December 29, 2001; 3—the active region observed at 16:16:43 on December 29, 2001; 4—the active region observed at 04:52:44 on December 30, 2001; mean—the value obtained by averaging 1–4 values; theory—the theoretical ratio based on CHIANTI data.

Table 6. Checking the Si VIII identification using SPIRIT data

Ratio	1	2	3	4	Mean	Theory
316.22/319.84	0.78	0.84	0.74	0.69	0.75	0.66
σ	0.04	0.04	0.03	0.03	0.02	
314.36/319.84	0.28	0.32	0.31	0.31	0.31	0.35
σ	0.03	0.02	0.02	0.03	0.01	

Note: 1—The flare of December 28, 2001; 2—the active region observed at 14:38:11 on December 29, 2001; 3—the active region observed at 16:16:43 on December 29, 2001; 4—the active region observed at 04:52:44 on December 30, 2001; mean—the value obtained by averaging 1–4 values; theory—the theoretical ratio based on the data of Brosius *et al.* (2000).

Al IX ($\log T = 6.0$). $2s^2 2p\ ^2P - 2s2p^2\ ^2P$.

$J_{low} - J_{up}$	λ, Å	Note
$1/2 - 1/2$	282.42	+
$3/2 - 1/2$	286.38	+b
$1/2 - 3/2$	280.14	+b
$3/2 - 3/2$	284.03	–

The Al IX 286.38 Å line is blended with the Fe XVII $2p^5 3p\ ^3D_1 - 2p^5 3d\ ^3F_2$ 286.42 Å line. The experimental line intensity ratio $I(286.38)/I(282.42)$ is equal to its theoretical value within 1σ (Table 5). Therefore, the contribution of the Fe XVII $2p^5 3p\ ^3D_1 - 2p^5 3d\ ^3F_2$ 286.42 Å line to the total intensity must be negligible. The Al IX 280.14 Å line is blended with the Fe XVII $2p^5 3p\ ^3P_2 - 2p^5 3d\ ^3D_3$ 280.14 Å line. The Al IX 284.03 Å line is blended with the Fe XV $3s^2\ ^1S_0 - 3s3p\ ^1P_1$ 284.16 Å line.

Si VIII ($\log T = 5.9$). $2s^2 2p^3\ ^4S - 2s2p^4\ ^4P$.

$J_{low} - J_{up}$	λ, Å	Note
$3/2 - 1/2$	314.36	+
$3/2 - 3/2$	316.22	+u
$3/2 - 5/2$	319.84	+

All multiplet component are observed. The intensity ratio of the multiplet lines depends weakly on the density (Brosius *et al.* 2000). The experimental ratio $I(316.22)/I(319.84)$ differs from its theoretical value by 4.5σ (Table 6); this could result from the blending of the 316.22 Å line with an unknown line (e.g., 316.1 Å) that is not observed separately in the published spectrum, but was observed in experiments (Thomas and Neupert 1994; Brosius *et al.* 2000). The experimental ratio $I(314.36)/I(319.84)$ differs from its theoretical value by 4σ (Table 6).

Si IX ($\log T = 6.1$). $2s^2 2p^2\ ^3P - 2s2p^3\ ^3P$.

$J_{low} - J_{up}$	λ, Å	Note
$1 - 0$	292.81	+b
$0 - 1$	290.69	+
$1 - 1$	292.86	+b
$2 - 1$	296.21	+b
$1 - 2$	292.76	+b
$2 - 2$	296.11	+b

Table 7. Checking the S XI identification with SPIRIT data

Ratio	1	2	3	4	Mean	Theory
285.59/281.40	1.00	0.54	0.58	0.74	0.61	0.49
σ	0.12	0.12	0.11	0.13	0.07	

Note: 1—The flare of December 28, 2001; 2—the active region observed at 14:38:11 on December 29, 2001; 3—the active region observed at 16:16:43 on December 29, 2001; 4—the active region observed at 04:52:44 on December 30, 2001; mean—the value obtained by averaging 2–4 values; theory—the theoretical ratio based on CHIANTI data.

Table 8. Checking the S XII identification with SPIRIT data

Ratio	1	2	3	4	Mean	Theory
288.42/299.78	–	8.34	8.83	8.70	8.61	9.26
σ	–	0.88	0.89	1.04	0.53	

Note: 1—The flare of December 28, 2001; 2—the active region observed at 14:38:11 on December 29, 2001; 3—the active region observed at 16:16:43 on December 29, 2001; 4—the active region observed at 04:52:44 on December 30, 2001; mean—the value obtained by averaging 2–4 values; theory—the theoretical ratio based on CHIANTI data.

All multiplet components are observed. The 292.86, 292.81, and 292.76 Å lines as well as the 296.11 and 296.21 Å lines are not resolved.

Si XI ($\log T = 6.2$). $2s^2\ ^1S_0 - 2s2p\ ^1P_1$.

The 303.33 Å line. Since this line is close to the resonance He II 303.8 Å line, only the peak intensity is given for it in Table 3.

S XI ($\log T = 6.3$). $2s^22p^2\ ^3P - 2s2p^3\ ^3D$.

$J_{\rm low} - J_{\rm up}$	λ, Å	Note
$0-1$	281.40	+
$1-1$	285.59	+u
$2-1$	291.57	+b
$1-2$	285.82	+
$2-2$	291.81	–
$2-3$	291.58	+b

All of the multiplet components, except for S XI 291.81 Å, are observed. The intensity of the S XI 291.81 Å line was determined from the intensity of the S XI 285.82 Å line and the branching ratio (CHIANTI):

$$I_{\rm S\,XI}(291.81) = 0.14 I_{\rm S\,XI}(285.82) = 25 \pm 2.$$

We see that the intensity of the S XI 291.81 Å line is much lower than that of the close Ni XVIII $3s\ ^2S_{1/2} - 3p\ ^2P_{3/2}$ 291.98 Å line, $I(291.98) = 4605 \pm 433$. Therefore, the S XI 291.81 Å line is not observed in the spectrum. The 281.40 Å line is wide, which may be due to the contribution from a close line, for example, Ni XXIII $2s^22p^2\ ^3P_1 - 2s^22p^2\ ^1S_0$ at 281.56 Å in the CHIANTI list. The intensity ratio $I(285.59)/I(281.40)$ differs from its theoretical value by 1.71σ (Table 7). The ratio for the flare differs from the ratios for the active regions, which may be due to the blending of the S XI 285.59 Å line in the flare with an unknown line. The S XI 291.57 Å and S XI 291.58 Å lines are not resolved. The intensities of S XI 291.57 Å and S XI 291.58 Å were determined from the intensity of the S XI 281.40 Å line and the branching ratio (CHIANTI):

$$I_{\rm S\,XI}(291.57) = 0.014 I_{\rm S\,XI}(281.40) = 1.7 \pm 0.1,$$

$$I_{\rm total}(291.58) = 290 \pm 13.$$

We see that the intensity of the S XI 291.57 Å $2s^22p^2\ ^3P_2 - 2s2p^3\ ^3D_1$ line is much lower than the total intensity of the lines and the measurement error of the latter. Therefore, the 291.58 Å line was identified as $2s^22p^2\ ^3P_2 - 2s2p^3\ ^3D_3$ 291.58 Å.

S XII ($\log T = 6.4$). $2s^22p\ ^2P - 2s2p^2\ ^2D$.

$J_{\rm low} - J_{\rm up}$	λ, Å	Note
$1/2 - 3/2$	288.42	+
$3/2 - 3/2$	299.78	+
$3/2 - 5/2$	299.54	+

All multiplet components are observed. The experimental ratio $I(288.42)/I(299.78)$ differs from its theoretical value by 1.23σ (Table 8). Table 8 gives no ratio for the published flare spectrum, because the 300.00 Å line strengthens significantly (Fig. 15), causing the measurement error in the parameters of the 299.78 Å line to increase greatly.

Ca XVIII ($\log T = 7.0$). $1s^22s\ ^2S - 1s^22p\ ^2P$.

$J_{\rm low} - J_{\rm up}$	λ, Å	Note
$1/2 - 1/2$	344.76	–l
$1/2 - 3/2$	302.19	+

The Ca XVIII 302.19 Å line is observed. This line in the images is observed only in hot regions: active regions, flares, and above-limb structures (Fig. 16). The contribution of the Fe XV $3s3p\ ^3P_0 - 3p^2\ ^3P_1$ 302.34 Å line to the total intensity does not exceed 10% and does not exceed the error in the

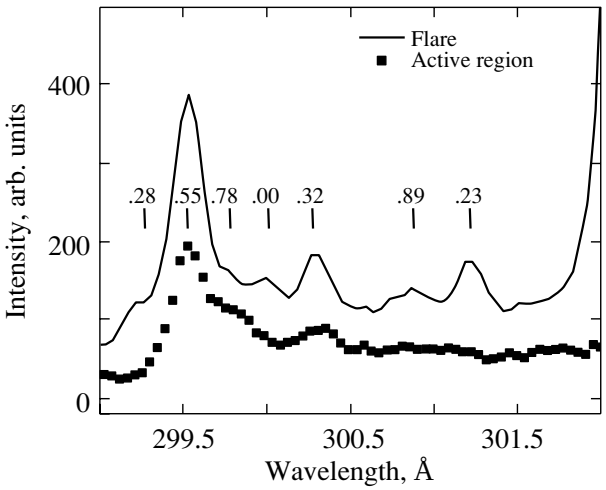

Fig. 15. Comparison of the S XII 299.78 Å line in the active region and in the flare. The vertical bars mark the observed lines for which the fractional part of the wavelength (to the second decimal place) is given.

Fig. 16. The pointlike region to the left of the bright central line corresponds to the flare image in the Ca XVIII 302.19 Å line.

intensity of the 302.19 Å line; an estimate of the contribution is given when discussing the Fe XV identification. Both Ca XVIII doublet lines were observed by Dere (1978); their intensity ratio is about 2, which confirms the identification.

Cr XIII ($\log T = 6.2$). $3s^2\ ^1S_0 - 3s3p\ ^1P_1$. The 328.27 Å line.

Cr XIV ($\log T = 6.4$). $2p^6 3p\ ^2P - 2p^6 3d\ ^2D$.

$J_{\rm low} - J_{\rm up}$	λ, Å	Note
$1/2 - 3/2$	289.75	+b
$3/2 - 3/2$	301.83	–
$3/2 - 5/2$	300.30	–u

Only the Cr XIV 289.75 Å line, blended with the Mn XIII $3s^2 3p\ ^2P_{3/2} - 3s3p^2\ ^2P_{1/2}$ 289.72 Å line, is observed. The Cr XIV 301.83 Å line is not observed. The maximum possible (in view of the blending) intensity of Cr XIV 301.83 Å was estimated from the intensity of the Cr XIV 289.75 Å line and the branching ratio (NIST):

$$I(301.83) = 0.18 I_{\rm CrXIV}(289.75) \leq 21 \pm 2.$$

We see that the Cr XIV 301.83 Å line is much weaker than the close Ca XVIII $1s^2 2s\ ^2S_{1/2} - 1s^2 2p\ ^2P_{3/2}$ 302.19 Å line. Therefore, it is not observed in the spectrum. The Cr XIV 300.30 Å line could correspond to the unidentified 300.32 Å line observed in the spectrum. However, as Keenan *et al.* (2003) showed, it follows from the SERTS measurements that the observed 300.32 Å line does not belong to CrXIV; therefore, the identification of this line is open to question.

Cr XXI ($\log T = 7.0$). $2s^2\ ^1S_0 - 2s2p\ ^3P_1$. The 293.11 Å line. A comparison of the line intensity in the active region and in the flare (Fig. 17) argues for the suggested identification.

Cr XXII ($\log T = 7.1$). $1s^2 2s\ ^2S - 1s^2 2p\ ^2P$.

$J_{\rm low} - J_{\rm up}$	λ, Å	Note
$1/2 - 1/2$	279.74	+
$1/2 - 3/2$	222.98	–l

The 279.74 Å line is observed. The intensity ratio of the Ca XVIII $1s^2 2s\ ^2S_{1/2} - 1s^2 2p\ ^2P_{3/2}$ 302.19 Å and Cr XXII 279.74 Å lines must roughly correspond to an abundance ratio of $10^{5.85-6.30} \approx 0.35$ (Allen 1973), because both lines belong to the same isoelectronic sequence. Since the $1s^2 2s\ ^2S_{1/2} - 1s^2 2p\ ^2P_{1/2}$ transition is observed for chromium, we obtain

$$\frac{2I_{\rm Cr\,XXII}(279.74)}{I_{\rm Ca\,XVIII}(302.19)} = 0.22 \pm 0.02.$$

The theoretical ratio exceeds the measured ratio by a factor of about 1.6. Probable causes of the difference is inaccuracy in the calibration of the spectral sensitivity of the instrument (given when describing the Fe XV identification), inaccuracy in the abundances, and the fact that the equality must be only approximate. A comparison of the line intensities in the active region and in the flare (Fig. 18) argues for the suggested identification. Dere (1978) observed both doublet lines.

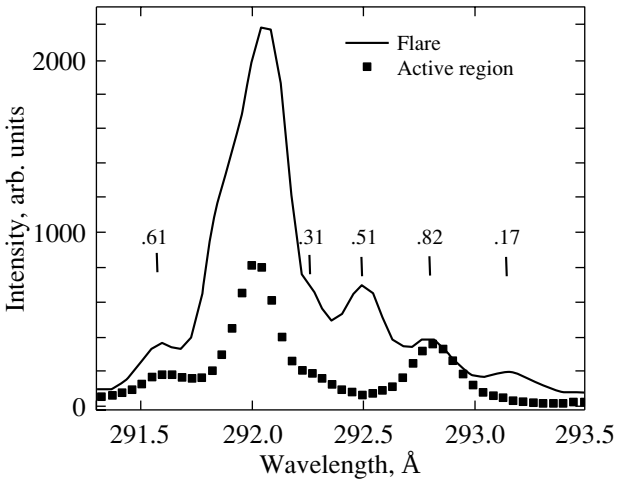

Fig. 17. Comparison of the Fe XXII 292.49 Å and Cr XXI 293.11 Å lines in the active region and in the flare. The vertical bars mark the observed lines for which the fractional part of the wavelength (to the second decimal place) is given.

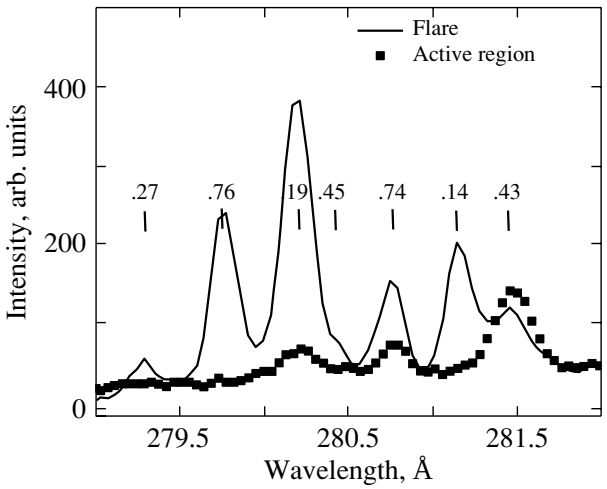

Fig. 18. Comparison of the Cr XXII 279.76 Å line in the active region and in the flare. The vertical bars mark the observed lines for which the fractional part of the wavelength (to the second decimal place) is given.

Mn XIII ($\log T = 6.2$). $3s^2 3p\ ^2P - 3s3p^2\ ^2P$.

$J_{\rm low} - J_{\rm up}$	λ, Å	Note
$1/2 - 1/2$	277.43	–l
$3/2 - 1/2$	289.72	+b
$1/2 - 3/2$	272.09	–
$3/2 - 3/2$	283.91	–

The Mn XIII 289.72 Å line is blended with the Cr XIV $2p^6 3p\ ^2P_{1/2} - 2p^6 3d\ ^2D_{3/2}$ 289.75 Å line.

Mn XIV ($\log T = 6.3$). $3s^2\ ^1S_0 - 3s3p\ ^1P_1$. The 304.85 Å line. Blended with the Fe XV $3s3p\ ^3P_2 - 3p^2\ ^3P_2$ 304.89 Å line. As we showed when describing the Fe XV identification, the Mn XIV 304.85 Å line contributes no more than 20%.

Fe XI ($\log T = 6.1$). $3s^2 3p^4\ ^1D_2 - 3s3p^5\ ^1P_1$. The 308.55 Å line.

Fe XII ($\log T = 6.2$). $3s^2 3p^3\ ^2D - 3s3p^4\ ^2P$.

$J_{\rm low} - J_{\rm up}$	λ, Å	Note
$3/2 - 1/2$	283.45	–
$3/2 - 3/2$	287.26	+
$5/2 - 3/2$	291.05	+

The Fe XII 283.45 Å line is not observed. This line may be obscured by the strong Fe XV 284.16 Å line. The experimental intensity ratio $I(287.26)/I(291.05)$ differs from its theoretical value by 3.58σ (Table 9). The large errors of these ratios stem from the fact that the Fe XII 287.26 Å line has a low intensity.

Fe XIII ($\log T = 6.2$). $3s^2 3p^2\ ^3P - 3s3p^3\ ^3P$.

$J_{\rm low} - J_{\rm up}$	λ, Å	Note
$1 - 0$	312.87	+
$0 - 1$	303.30	–
$1 - 1$	312.11	+u
$2 - 1$	321.40	+
$1 - 2$	311.55	+
$2 - 2$	320.81	+

All of the multiplet components, except for the 303.30 Å line blended with the SiXI 303.33 Å line, are observed. The experimental intensity ratio $I(312.11)/I(321.4)$ differs from its theoretical value by 5.33σ (Table 10). A probable cause of the difference is the blending of the 312.11 Å line with an unknown line. The experimental intensity ratio $I(320.809)/I(311.553)$ differs from its theoretical value by 2.5σ (Table 10).

$3s^2 3p^2\ ^1D_2 - 3s3p^3\ ^1D_2$. The 318.13 Å line.

Fe XIV ($\log T = 6.3$). $3s^2 3p\ ^2P - 3s3p^2\ ^2S$. Only the Fe XIV 289.15 Å line is observed.

$J_{\rm low} - J_{\rm up}$	λ, Å	Note
$1/2 - 1/2$	274.20	–l
$3/2 - 1/2$	289.15	+

Fe XV ($\log T = 6.4$). $3s^2\ ^1S_0 - 3s3p\ ^1P_1$. The 284.16 Å line. Since the image of the solar disk is very intense, only the peak intensity was determined for this line.

$3s3p\ ^3P - 3p^2\ ^1D$.

$J_{low} - J_{up}$	λ, Å	Note
$1-2$	312.57	+b
$2-2$	327.03	+

All multiplet components are observed. The Fe XV 312.57 Å line is blended with the Co XVII $3s\ ^2S_{1/2} - 3p\ ^2P_{3/2}$ 312.54 Å line, as confirmed by the difference between the experimental and theoretical intensity ratios $I(327.03)/I(312.57)$ by more than 10σ (Table 11). The difference between the experimental and theoretical ratios $I(327.03)/I(312.57)$ for the flare spectrum is larger than that for the spectra of the active regions (Table 11), because the blending line gives a larger contribution (the decimal logarithm of the temperature of the maximum abundance for Co XVII 6.7 against 6.4 for Fe XV (CHIANTI)). The intensity of the Fe XV 312.57 Å line was estimated from that of the FeX V 327.03 Å line and the branching ratio (CHIANTI):

$$I_{\mathrm{Fe\,XV}}(312.57) = 0.55 I_{\mathrm{Fe\,XV}}(327.03) = 315 \pm 32.$$

The ratio $I(327.03)/I(284.16)$ depends weakly on the temperature (less than 10%) and the density (no more than 20%), being about 0.01 (Brickhouse *et al.* 1995). The close match between the theoretical and experimental values in previous experiments (Table 12) confirms the identification of the Fe XV 327.03 Å line. In the SPIRIT experiment, the ratio differed from its theoretical value by 7.67σ, although it remained constant for the whole series of spectra (Table 11). This could be attributable to a calibration error or optical vignetting near 284.16 Å. It is also possible that the plasma is not optically thin in this line.

$3s3p\ ^3P - 3p^2\ ^3P$.

$J_{low} - J_{up}$	λ, Å	Note
$1-0$	317.60	+
$0-1$	302.34	–
$1-1$	307.75	+
$2-1$	321.77	+
$1-2$	292.28	+
$2-2$	304.89	+b

All of the multiplet components, except for the 302.34 Å line, are observed. The Fe XV 302.34 Å line must be a factor of 1.4 more intense than the Fe XV 307.75 Å line; i.e., its intensity must be about 318 ± 20, while the intensity of the 302.3 Å line (the experimental wavelength, identified as the Ca XVIII $1s^2 2s\ ^2S_{1/2} - 1s^2 2p\ ^2P_{3/2}$ 302.19 Å line) is 3212 ± 301. Thus, this iron line can contribute about 10%. The experimental intensity ratio $I(307.75)/I(321.77)$ differs from its theoretical value by 2.5σ (Table 11) and confirmed the identification. The Fe XV $3s3p\ ^3P_2 - 3p^2\ ^3P_2$ 304.89 Å line is blended with the Mn XIV $3s^2\ ^1S_0 - 3s3p\ ^1P_1$ 304.85 Å line. The Fe XV 292.28 Å line in the spectra of the active regions is clearly observed in the wing of the Ni XVIII $3s\ ^2S_{1/2} - 3p\ ^2P_{3/2}$ 291.98 Å line, and the line position, intensity, and width can be determined accurately. In the flare spectrum, an intense Fe XXII $2s^2 2p\ ^2P_{3/2} -$

Table 9. Checking the Fe XII identification with SPIRIT data

Ratio	1	2	3	4	Mean	Theory
291.05/287.26	5.68	7.68	10.03	5.47	6.15	8.48
σ	1.01	1.69	2.76	1.07	0.65	

Note: 1—The flare of December 28, 2001; 2—the active region observed at 14:38:11 on December 29, 2001; 3—the active region observed at 16:16:43 on December 29, 2001; 4—the active region observed at 04:52:44 on December 30, 2001; mean—the value obtained by averaging 1–4 values; theory—the theoretical ratio based on CHIANTI data.

Table 10. Checking the Fe XIII identification with SPIRIT data

Ratio	1	2	3	4	Mean	Theory
312.11/321.40	–	2.51	2.64	2.15	2.42	1.94
σ	–	0.19	0.17	0.16	0.09	
311.55/320.81	0.16	0.17	0.22	0.16	0.18	0.13
σ	0.09	0.03	0.04	0.03	0.02	

Note: 1—The flare of December 28, 2001; 2—the active region observed at 14:38:11 on December 29, 2001; 3—the active region observed at 16:16:43 on December 29, 2001; 4—the active region observed at 04:52:44 on December 30, 2001; mean—the value obtained by averaging 1–4 values; theory—the theoretical ratio based on CHIANTI data.

Table 11. Checking the Fe XV identification using SPIRIT data

Ratio	1	2	3	4	mean	Theory
327.03/312.57	0.89	1.37	1.15	1.29	1.22	1.81
σ	0.15	0.08	0.07	0.08	0.05	
327.03/284.16	0.041	0.034	0.030	0.033	0.033	0.01
σ	0.008	0.004	0.004	0.004	0.003	
307.75/321.77	0.83	0.74	0.75	0.81	0.79	0.69
σ	0.06	0.08	0.11	0.11	0.04	
292.28/304.89	–	0.34	0.26	0.27	0.28	0.35
σ	–	0.03	0.02	0.02	0.01	

Note: 1—The flare of December 28, 2001; 2—the active region observed at 14:38:11 on December 29, 2001; 3—the active region observed at 16:16:43 on December 29, 2001; 4—the active region observed at 04:52:44 on December 30, 2001; mean—the value obtained by averaging 1–4 values; theory—the theoretical ratio based on CHIANTI data.

$2s2p^2\ ^4P_{3/2}$ 292.49 Å line appears near the Fe XV 292.28 Å line; as a result, the parameters of Fe XV 292.28 Å can be determined only with a large error. Therefore, Table 11 gives the experimental ratios $I(292.28)/I(304.89)$ only for the active regions. The experimental intensity ratio $I(292.28)/I(304.89)$ differs from its theoretical value by 7σ due to the contribution of Mn XIV $3s^2\ ^1S_0 - 3s3p\ ^1P_1$ 304.85 Å noted above, which can estimated from this difference as 20%. The Fe XV $3s3p\ ^3P_1 - 3p^2\ ^3P_0$ 317.60 Å line is observed, but a significant error in its intensity, attributable to the presence of the unidentified 317.42 Å line and the Mg VIII $2s^22p\ ^2P_{3/2} - 2s2p^2\ ^2P_{1/2}$ 317.03 Å line near it, cannot be ruled out.

$3s3p\ ^1P_1 - 3p^2\ ^1S_0$. The 324.98 Å line.

Fe XVII ($\log T = 6.9$). $2p^53p\ ^3P - 2p^53d\ ^3D$.

$J_{low} - J_{up}$	λ, Å	Note
0 – 1	285.44	–
1 – 1	244.46	–l
2 – 1	...	...
1 – 2	275.54	–l
2 – 2	287.12	–
2 – 3	280.14	+b

Only the Fe XVII 280.14 Å line is observed; it is blended with the Al IX $2s^22p\ ^2P_{1/2} - 2s2p^2\ ^2P_{3/2}$ 280.14 Å line.

$2p^53p\ ^3D - 2p^53d\ ^3F$. The Fe XVII 286.42 Å line is blended with Al IX $2s^22p\ ^2P_{3/2} - 2s2p^2\ ^2P_{1/2}$ 286.38 Å; the Fe XVII line probably makes a minor contribution to the total intensity, as we see from the discussion of the Al IX identification. The Fe XVII 284.17 Å line is obscured by the Fe XV $3s^2\ ^1S_0 - 3s3p\ ^1P_1$ 284.16 Å line.

$J_{low} - J_{up}$	λ, Å	Note
1 – 2	286.42	+b
2 – 2	211.48	–l
3 – 2	217.47	–l
2 – 3	269.42	–l
3 – 3	279.21	–
3 – 4	284.17	–

Fe XXII ($\log T = 7.1$). $2s^22p\ ^2P - 2s2p^2\ ^4P$.

$J_{low} - J_{up}$	λ, Å	Note
1/2 – 1/2	247.20	–l
3/2 – 1/2	349.32	–l
1/2 – 3/2	217.32	–l
3/2 – 3/2	292.49	+
3/2 – 5/2	253.17	–l

The Fe XXII 292.49 Å line is observed. A comparison of the line intensities in the active region

Table 12. Checking the FeXV 327.03 Å identification in previous works

Ratio	1	2	3	4	5
327.03/284.16	0.012	0.090	0.010	0.009	0.006
σ	0.002	0.002	0.002	0.002	0.002

Note: 1—Active region (Thomas and Neupert *et al.* 1994), 2—active region (Brosius *et al.* 1996), 3—quiet Sun (Brosius *et al.* 1996), 4—active region (Brosius *et al.* 1996), 5—above-limb spectrum (Brosius *et al.* 1996).

and in the flare confirms the suggested identification (Fig. 17): this line is clearly observed only in the flare spectrum.

Co XVII ($\log T = 6.7$). $3s\ ^2S - 3p\ ^2P$.

$J_{\rm low} - J_{\rm up}$	λ, Å	Note
$1/2 - 1/2$	339.50	–l
$1/2 - 3/2$	312.54	+

The Co XVII 312.54 Å line is blended with Fe XV $3s3p\ ^3P_1 - 3p^2\ ^1D_2$ 312.57 Å. The intensity of Co XVII 312.54 Å was estimated from the equation

$$I_{\rm Co\,XVII}(312.54) = I_{\rm total}(312.57) - I_{\rm Fe\,XV}(312.57) = 319 \pm 37.$$

The second Co XVII 339.5 Å double line was observed in the spectra by Dere (1978) and Thomas and Neupert (1994).

Ni XV ($\log T = 6.4$). $3s^23p^2\ ^3P - 3s3p^3\ ^3D$.

$J_{\rm low} - J_{\rm up}$	λ, Å	Note
$0 - 1$	298.15	+
$1 - 1$	312.03	–
$2 - 1$	324.65	–
$1 - 2$	311.76	+
$2 - 2$	324.35	–
$2 - 3$	319.06	+

The Ni XV 319.06 Å line is blended with Mg VII $2s^22p^2\ ^1D - 2s2p^3\ ^1D$ 319.02 Å. The Ni XV 312.03 Å line must be a factor of 5.76 weaker than the Ni XV 298.15 Å line (NIST), as the intensity of this line is low and much smaller (~3%) than that of the nearby strong Fe XIII 312.11 Å line:

$$I_{\rm Ni\,XV}(312.03) = 0.17 I_{\rm Ni\,XV}(298.15) = 13 \pm 11,$$

$$I_{\rm Fe\,XIII}(312.11) = 402 \pm 14.$$

Table 13. Checking the Ni XVIII identification using SPIRIT data

Ratio	1	2	3	4	Mean	Theory
291.98/320.57	2.51	2.09	1.98	2.29	2.24	2.00
σ	0.25	0.20	0.37	0.22	0.12	

Note: 1—The flare of December 28, 2001; 2—the active region observed at 14:38:11 on December 29, 2001; 3—the active region observed at 16:16:43 on December 29, 2001; 4—the active region observed at 04:52:44 on December 30, 2001; mean—the value obtained by averaging 1–4 values; theory—the theoretical ratio based on the data by Neupert and Kastner (1983).

The Ni XV 324.65 Å line is a factor of 95 weaker than the Ni XV 298.15 Å line (NIST); as we see, the line intensity $I_{\rm Ni\,XV}(324.65)$ is very low:

$$I_{\rm Ni\,XV}(324.65) = 0.011 I_{\rm Ni\,XV}(298.15) = 0.79 \pm 0.65.$$

The Ni XV 311.76 Å line is blended with the Mg VIII 311.77 Å line and contributes up to 40% to the total intensity; the equation yields 87 ± 6. The Ni XV 324.35 Å line must be weaker than the Ni XV 311.76 Å line by a factor of 95.23 (NIST):

$$I_{\rm Ni\,XV}(324.35) = 0.011 I_{\rm Ni\,XV}(311.76) = 0.96 \pm 0.07.$$

Thus, the Ni XV 324.35 Å line is very weak and is not observed in the spectrum. Note that the 324.35 and 324.65 Å lines were not observed in previous experiments either, probably because of their extremely low intensity (Behring *et al.* 1976; Dere 1978; Thomas and Neupert 1994; Brosius *et al.* 2000). Recently, Brooks *et al.* (1999) reported the observation of the extremely weak unidentified 324.32 and 324.64 Å lines in the spectrum of the quiet Sun. It may well be that they correspond to the nickel lines, but the published intensities were measured with errors of 100 and 71%, respectively. Thus, the spectrum presented here exhibits three lines, Ni XV 298.15, 311.76, and 319.06 Å.

Ni XVI ($\log T = 6.4$). $3s^23p\ ^2P - 3s3p^2\ ^2D$.

$J_{\rm low} - J_{\rm up}$	λ, Å	Note
$1/2 - 3/2$	288.17	+
$3/2 - 3/2$	313.23	–
$3/2 - 5/2$	309.18	+bu

The intensity of the Ni XVI 313.23 Å line can be estimated from that of the Ni XVI 288.17 Å line, because they share a common level:

$$I_{\rm Ni\,XVI}(313.23) = 0.03 I_{\rm Ni\,XVI}(288.17) = 10 \pm 1.$$

The intensity of the Ni XVI 313.23 Å line is at the noise level. The 309.18 Å line may be blended, as suggested by the large line width.

Ni XVIII ($\log T = 6.7$). $3s\ ^2S - 3p\ ^2P$.

$J_{low} - J_{up}$	λ, Å	Note
$1/2 - 1/2$	320.57	+
$1/2 - 3/2$	291.98	+

All multiplet components are observed. The experimental intensity ratio $I(291.98)/I(320.57)$ differs from its theoretical value by 2σ (Table 13).

CONCLUSIONS

We have presented a catalog of 100 lines in the wavelength range 280–330 Å detected by the RES-C spectroheliograph in the SPIRIT experiment aboard CORONAS-F in flares and active regions. We used the spectra for the X3.4 flare of December 28, 2001, and the active region NOAA 9765. Based on the spectral image reduction, analysis of the relative line intensities, and CHIANTI data, we calibrated the wavelengths and intensities of the instrument. The accuracy of determining the wavelengths is 40 mÅ, the spectral resolution is 0.1 Å, and the calibration accuracy of the relative intensities is 20%. Among the 100 presented lines, 15 are observed only in flares. We identified 54 lines and noted clear blends. For the December 28, 2001, flare, we gave the relative line intensities.

ACKNOWLEDGMENTS

We wish to thank I.I. Sobel'man and O.I. Bugaenko for their help. This work was supported in part by the NATO (grant PST.CLG.979372), the Russian Foundation for Basic Research (project nos. 03-02-16053, 02-02-16613, 02-02-17272) and the following programs of the Russian Academy of Sciences: Nonstationary Processes in Astronomy, Solar Wind (N16), and Optical Spectroscopy and Frequency Standards.

REFERENCES

1. C. W. Allen, *Astrophysical Quantities*, 3rd ed. (Athlone Press, London, 1973; Mir, Moscow, 1977).
2. W. E. Behring, L. Cohen, and U. Feldman, Astrophys. J. **175**, 493 (1972).
3. W. E. Behring, L. Cohen, U. Feldman, and G. A. Dosheck, Astrophys. J. **203**, 521 (1976).
4. S. Brandt, *Statistical and Computational Methods in Data Analysis* (North-Holland, Amsterdam, 1976; Mir, "OOO Izdatel'stvo AST," Moscow, 2003).
5. N. S. Brickhouse, J. C. Raymond, and B. W. Smith, Astrophys. J., Suppl. Ser. **97**, 551 (1995).
6. D. H. Brooks, G. A. Fishbacher, A. Fludra, *et al.*, Astron. Astrophys. **347**, 277 (1999).
7. J. W. Brosius, J. M. Davila, and R. J. Thomas, Astrophys. J., Suppl. Ser. **106**, 143 (1996).
8. J. W. Brosius, J. M. Davila, and R. J. Thomas, Astrophys. J., Suppl. Ser. **119**, 255 (1998).
9. J. W. Brosius, R. J. Thomas, and J. M. Davila, Astrophys. J. **543**, 1016 (2000).
10. CHIANTI, http://www.solar.nrl.navy.mil/chianti.html.
11. K. P. Dere, Astrophys. J. **221**, 1062 (1978).
12. G. A. Doschek, *Extreme Ultraviolet Astronomy*, Ed. by R. F. Malina and S. Bowyer (Pergamon Press, 1991).
13. C. Jordan, Astron. Astrophys. **34**, 69 (1974).
14. C. Jordan, *Progress in Atomic Spectroscopy*, Ed. by W. Hanle and H. Kleinpoppen (Plenum, New York, 1979), Part B.
15. F. P. Keenan, A. C. Katsiyannis, J. W. Brosius, *et al.*, Mon. Not. R. Astron. Soc. **342**, 513 (2003).
16. S. V. Kuzin, I. A. Zhitnik, A. A. Pertsov, *et al.*, J. X-Ray Sci. Technol. **7**, 233 (1997).
17. J. Lang, H. E. Mason, and R. W. McWhirter, Solar Phys. **129**, 31 (1990).
18. M. Malinovsky and L. Heroux, Astrophys. J. **181**, 1009 (1973).
19. A. V. Mitrofanov and S. Yu. Zuev, *Spectral Properties of Thin-Film X-ray Filters Based of Track Membranes Surface* (2002).
20. W. M. Neupert and S. O. Kastner, Astron. Astrophys. **128**, 181 (1983).
21. NIST, http://www.physics.nist.gov/cgibin/AtData/lines_form.
22. V. N. Oraevskiĭ and I. I. Sobel'man, Pis'ma Astron. Zh. **28**, 457 (2002) [Astron. Lett. **28**, 401 (2002)].
23. H. W. Press, S. A. Teukolsky, W. T. Vetterling, and B. P. Flanery, *Numerical Recipes in Fortran 77. The Art of Scientific Computing* (Univ. Cambridge, 2001).
24. I. I. Sobel'man, I. A. Zhitnik, A. P. Ignat'ev, *et al.*, Pis'ma Astron. Zh. **22**, 604 (1996) [Astron. Lett. **22**, 539 (1996)].
25. R. J. Thomas and W. M. Neupert, Astrophys. J., Suppl. Ser. **91**, 461 (1994).
26. I. A. Zhitnik, O. I. Bougaenko, V. A. Slemzin, *et al.*, ESA SP-506 **2**, 915 (2002).
27. I. A. Zhitnik, S. V. Kuzin, V. N. Oraevskiĭ, *et al.*, Pis'ma Astron. Zh. **24**, 943 (1998) [Astron. Lett. **24**, 819 (1998)].
28. I. A. Zhitnik, S. V. Kuzin, A. M. Urnov, *et al.*, Mon. Not. R. Astron. Soc. **308**, 228 (1999).

Translated by V. Astakhov

Astronomy Letters, Vol. 31, No. 1, 2005, pp. 57–63. Translated from Pis'ma v Astronomicheskiĭ Zhurnal, Vol. 31, No. 1, 2005, pp. 59–65.

Energy Spectrum of the Time Profiles for Weak Solar Soft X-ray Bursts

I. K. Mirzoeva*

Space Research Institute, Russian Academy of Sciences, ul. Profsoyuznaya 84/32, Moscow, 117997 Russia

Received April 29, 2004

Abstract—We analyze the time profiles for weak solar soft X-ray bursts over the period 1995–1999 within the framework of the Interball–Tail Probe project. We have revealed a tendency for the peak of the energy spectrum of the time profiles for weak solar soft X-ray bursts to shift and their correlation with the thermal background. © *2005 Pleiades Publishing, Inc.*

Key words: *Sun*.

INTRODUCTION

Studies of low-intensity solar X-ray bursts can provide valuable information about the microstructure of solar active regions. Within the framework of the Interball—Tail Probe project, the solar soft X-ray radiation was measured using the RF-15I-2 X-ray detector (Farnik *et al.* 1995; Likin *et al.* 1998).

Recall that low-intensity solar events are all events with peak X-ray fluxes $<10^{-6}$ W m^{-2}, i.e., class B, A, and 0 events with peak fluxes $<10^{-8}$ W m^{-2} (Mirzoeva and Likin 2002, 2004). Such series of weak X-ray bursts were recorded from September through December 1995 by the RF-15I-2 X-ray detector in the energy range 2–15 keV.

Using data obtained from August 1995 through December 1999, we analyze class A and class 0 bursts. The separation of the energy range of the RF-15I-2 detector into subranges, 2–3, 3–5, 5–8, and 10–15 keV, allowed us to determine the peculiarities of the time profiles for weak bursts in narrower energy bands.

ANALYSIS OF THE EXPERIMENTAL DATA

For weak solar soft X-ray bursts recorded from August 1995 through December 1999, we found the following peculiarities: in years close to the solar minimum or, more specifically, in 1995 and 1996, most of the class A and 0 bursts were recorded in the 2–3 and 3–5 keV energy bands, while the number of such bursts in the 5–8 and 10–15 keV energy bands was insignificant (less than 10% of the total number of bursts). Below, we give several typical examples of the time profiles for weak solar soft X-ray bursts for this period.

Series of class A bursts are seen in the 2–3 and 3–5 keV energy bands from 14 h 46 min December 11 until 11 h 32 min December 12, 1995. The 5–8 and 10–15 keV channels for this period contain only a thermal background (Fig. 1). Series of class 0 bursts and one class A burst were recorded in the same energy bands from 0 h 0 min until 12 h 48 min December 15, 1995. As in the previous case, the 5–8 and 10–15 keV channels for this period contain only a thermal background (Fig. 2). Series of weak class A bursts and series of class B bursts (with X-ray fluxes from 10^{-7} to 10^{-6} W m^{-2}) were recorded in the 2–3 and 3–5 keV energy bands from 7 h 01 min May 7 until 0 h 34 min May 8, 1996. The same series of class B bursts were recorded in the 5–8 and 10–15 keV bands, while virtually no class A bursts were observed in these energy bands (Fig. 3).

A shift in the maximum of the number of weak X-ray bursts from the 2–5 to the 3–8 keV band was observed in similar measurements performed in 1997. Meanwhile, very few or no X-ray bursts were observed at energies >8 keV. For instance, weak class A bursts were recorded in the 3–5 and 5–8 keV energy bands from 20 h 01 min June 5 until 12 h 02 min June 6, 1997. The 2–3 and 10–15 keV channels for the same period contain only a thermal background (Fig. 4).

*E-mail: ikir@ares.iki.rssi.ru

1063-7737/05/3101-0057$26.00

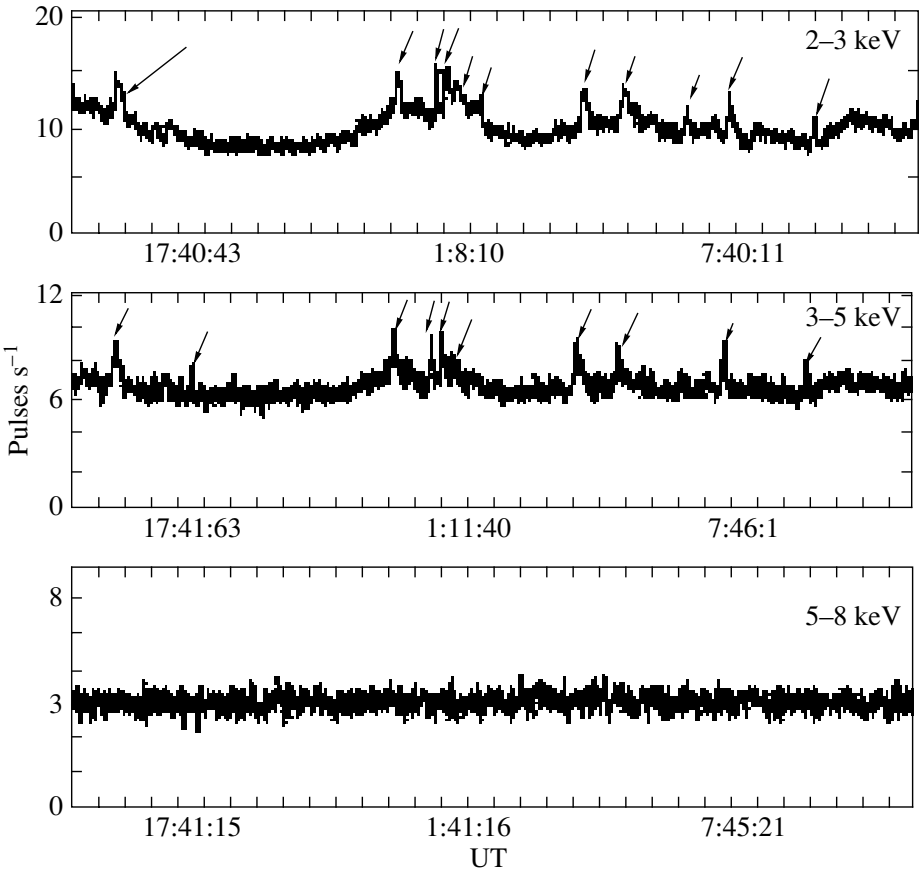

Fig. 1. Weak solar soft X-ray bursts recorded in the 2–3 and 3–5 keV energy bands from 14 h 46 min December 11 until 11 h 32 min December 12, 1995. Class A bursts are marked by the arrows.

We may assume that the peak of the distribution of weak X-ray solar bursts would shift further toward the energies 10–15 keV. Indeed, this assumption was confirmed by the observation of weak bursts in 1998 and 1999.

Beginning from the second half of 1998, the picture gradually changed: the number of weak bursts increased in the 5–8 and 10–15 keV energy bands (especially in the 10–15 keV band); i.e., bursts were observed more commonly at relatively high energies. For instance, from 6 h 36 min until 21 h 24 min July 17, 1998, class A bursts were recorded more commonly in the 5–8 and 10–15 keV bands (Fig. 5).

The year 1999 was one close to the maximum of the current solar cycle. In this period, much more strong class C and M solar soft X-ray bursts were observed in all energy bands. This severely hampered the detection of low-intensity solar events. However, on several days when there were few strong bursts, we were able to record the periods suitable for an analysis when weak bursts were detected only in the 10–15 keV energy band, while there were no weak bursts in the remaining energy bands. Thus, for example, more class A and B bursts were recorded in the 10–15 keV band from 23 h 40 min November 24 until 3 h 53 min November 25, 1999. In the 2–8 keV band, we

Thermal background (pulses s^{-1})

Date	Energy band, keV			
	2–3	3–5	5–8	10–15
1995	7–30	6–10	3	15–27
1996	7–20	6–10	3	12–18
1997	6–13	12–70	5–160	9–30
January–June 1998	4–5	6–20	12–90	9–10
June–December 1998	3–4	5–6	5–20	10–50
1999	3–6	4–9	3–10	9–60

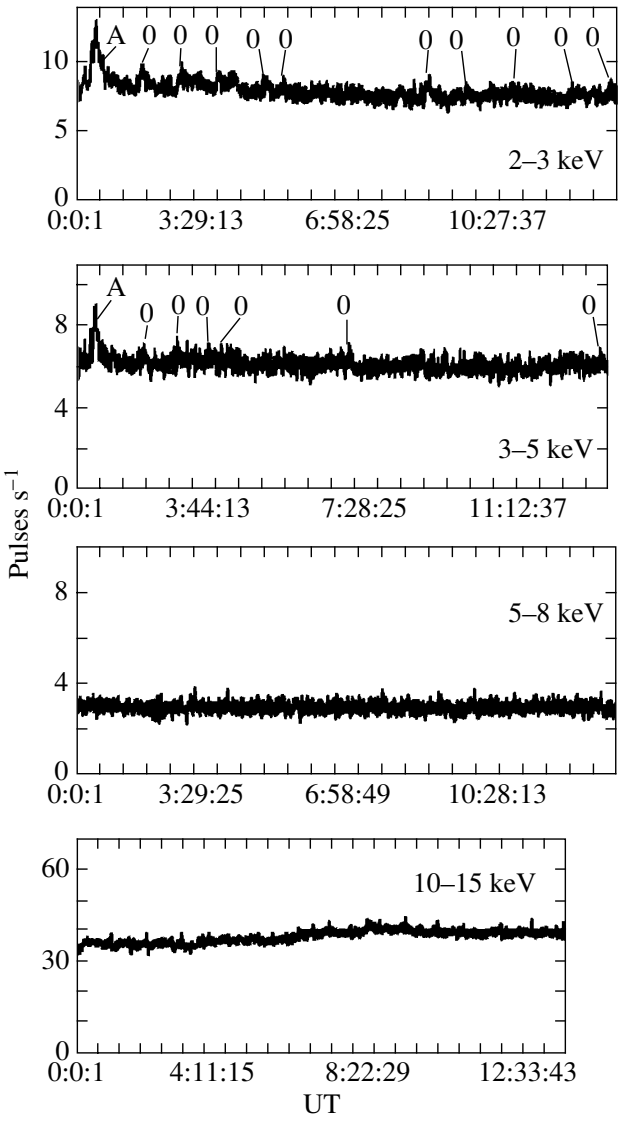

Fig. 2. Weak solar soft X-ray bursts recorded in the 2–3 and 3–5 keV energy bands from 0 h 0 min until 12 h 48 min December 15, 1995. Class 0 bursts and a class A burst are marked by the arrows.

recorded appreciably fewer such bursts (Fig. 6). This trend persisted throughout 1999.

Figure 7 shows the overall pattern of displacement of the energy spectrum of the time profiles for weak solar soft X-ray bursts in the period 1995–1999. The burst detection energy band in keV and the years of observation are along the vertical and horizontal axes, respectively.

Weak bursts have a significant effect on the background X-ray radiation that is mainly thermal in origin. Thus, during each year of the current solar cycle, the thermal background level was stabilized in the energy bands where few or no weak bursts were observed. At the same time, we recorded a larger spread in thermal background values in the energy bands where more weak bursts were detected. The table gives the spread in mean thermal background values in various energy bands for the period from 1995 until 1999.

In 1995 and 1996, weak bursts were recorded more commonly in the 2–3 and 3–5 keV energy bands. The minimum and maximum thermal background values in these energy bands differed by factors of 4.2 and 1.6, respectively. At the same time, the thermal background in the 5–8 keV band was almost constant, while the spread in thermal background values in the 10–15 keV band decreased from a factor of 1.8 to a factor of 1.5 from 1995 until 1996. In 1997, more

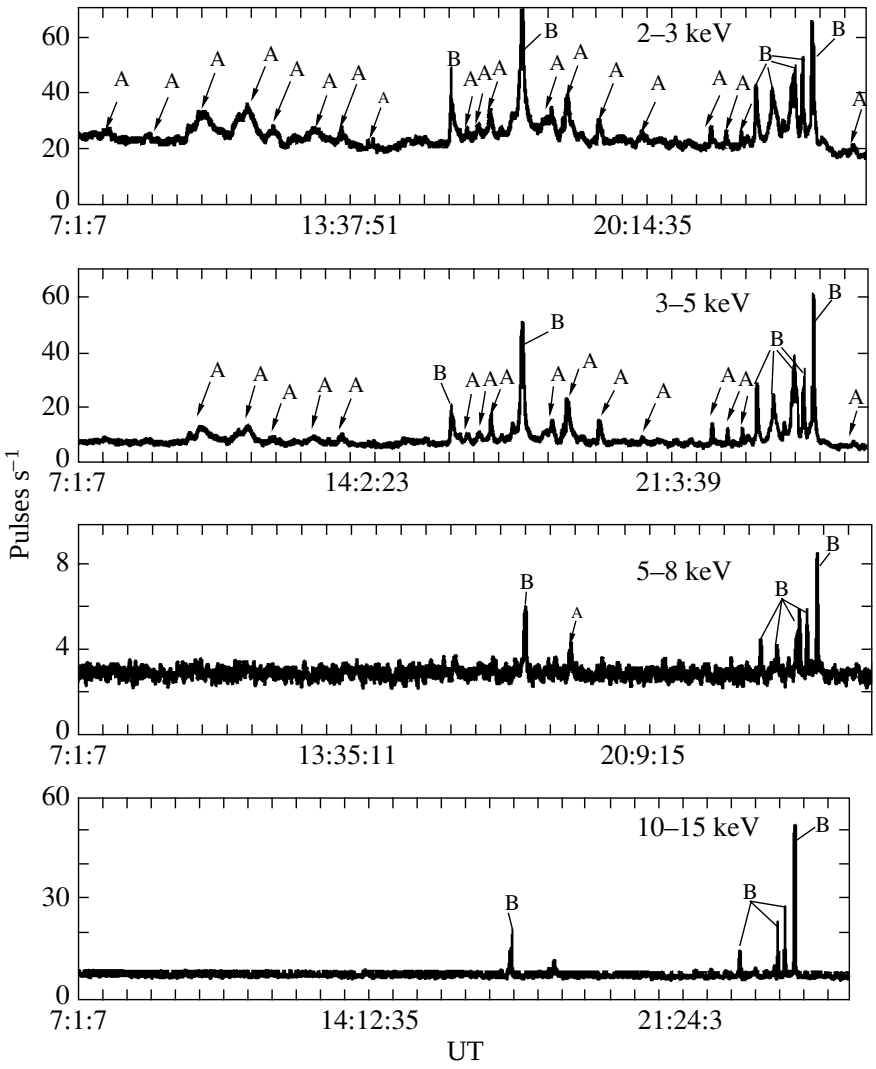

Fig. 3. Weak solar soft X-ray bursts recorded in the 2–3 and 3–5 keV energy bands from 7 h 01 min May 7 until 0 h 34 min May 8, 1996. Class A and B bursts are marked by the arrows.

weak bursts were recorded in the 3–5 and 5–8 keV energy bands. The minimum and maximum thermal background values in these energy bands differed by factors of 6 and 32, respectively, while in the 2–3 and 10–15 keV energy bands where few weak bursts were observed in 1997, the thermal background values differed by factors of only 2 and 3, respectively. In the period January–June 1998, weak bursts were recorded more commonly in the 3–5 and 5–8 keV energy bands, as before. The spread in thermal background values in this part of the energy spectrum decreased slightly: the corresponding values differed by factors of 3 and 8, but this is still larger than the background spread in the 2–3 and 10–15 keV energy bands where there were few weak bursts: here, the values differed by a factor of 1.1. In the period June–December 1998, the energy spectrum of the detected weak bursts shifted toward the energies 5–8 and 10–15 keV. Accordingly, in these energy bands, the spread in thermal background values increased by factors of 4 and 5. In contrast, in the 2–3 and 3–5 keV bands, the background was stabilized, and its spread was much smaller (factors of 1.3 and 1.2, respectively). In 1999, weak bursts were recorded more commonly in the 10–15 keV band. Accordingly, in this energy band, the spread in thermal background values is largest for 1999, a factor of 6.7. In contrast, in the energy bands with a smaller number of weak bursts (2–3, 3–5, and 5–8 keV), the spread in thermal background values was smaller (factors of 2, 2.3, and 3.3, respectively).

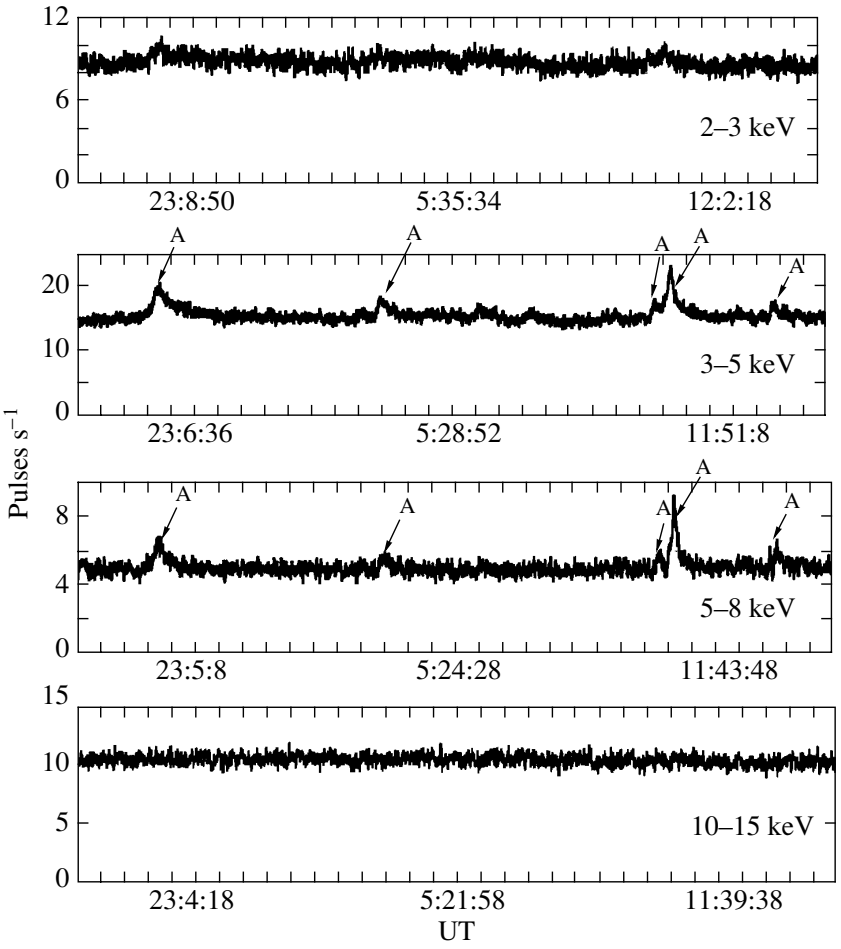

Fig. 4. Weak solar soft X-ray bursts recorded in the 3–5 and 5–8 keV energy bands from 20 h 01 min June 5 until 12 h 02 min June 6, 1997. Class A bursts are marked by the arrows.

CONCLUSIONS

(1) The number of weak solar soft X-ray bursts in various energy bands from 2–3 to 10–15 keV depended on the observing period in the solar cycle.

(2) Depending on the period in the solar cycle, weak bursts were recorded more commonly in the following energy bands:

1995—2–3, 3–5 keV;

1996—2–3, 3–5 keV;

1997—3–5, 5–8 keV;

January–June 1998—3–5, 5–8 keV;

June–December 1998—5–8, 10–15 keV;

1999—10–15 keV.

(3) The observations of the time profiles for weak solar soft X-ray bursts, carried out from 1995 until 1999, lead us to the following conclusions about the peculiarities of the physical processes in solar active regions in relatively narrow energy bands in separate periods of the solar cycle:

(i) The mean energy of weak bursts increases with growing solar activity;

(ii) We found a correlation between the number of weak bursts and the spread in thermal background values: a larger spread in thermal background values is observed in the periods and energy bands where class A and 0 bursts were recorded more commonly.

(4) The correlation between the intensity of the background X-ray radiation and weak X-ray bursts can probably be explained by the absence of a sharp boundary between the thermal background and the X-ray burst proper generated by the particle acceleration during a flare in an active region. An X-ray flare can be imagined as a superposition of the thermal and nonthermal X-ray components (Krucker *et al.* 2002) or as a superposition of a number of elementary energy release events (Pisarenko and Likin 1995),

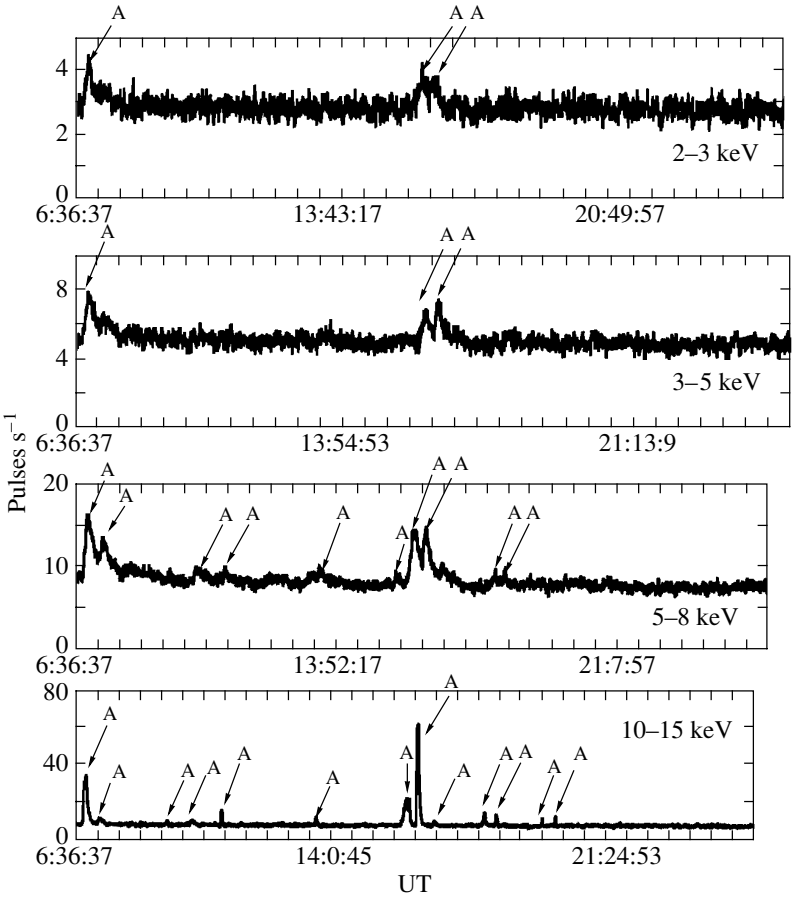

Fig. 5. Weak solar soft X-ray bursts recorded in the 5–8 and 10–15 keV energy bands from 6 h 36 min until 21 h 24 min July 17, 1998. Class A bursts are marked by the arrows.

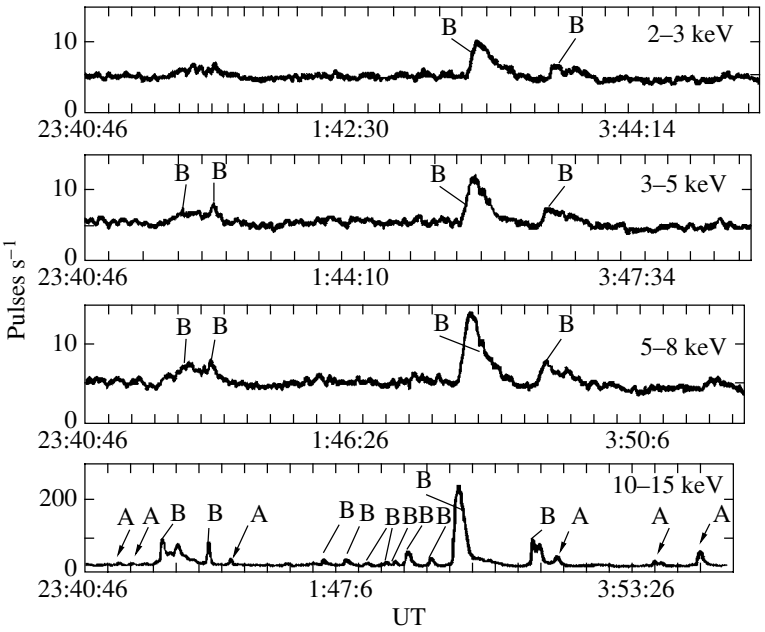

Fig. 6. Weak solar soft X-ray bursts recorded in the 10–15 keV energy band from 23 h 40 min November 24 until 3 h 53 min November 25, 1999. Class A and B bursts are marked by the arrows.

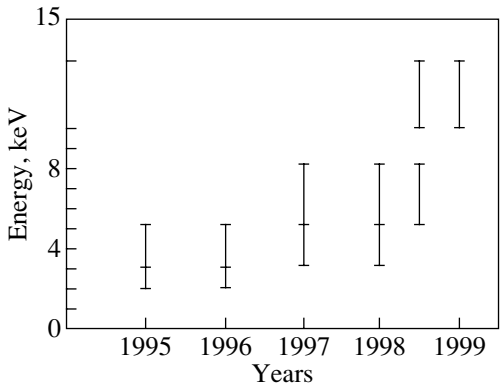

Fig. 7. Overall pattern of displacement of the energy spectrum of the time profiles for weak solar soft X-ray bursts in the period 1995–1999.

each of which can be either thermal or nonthermal in origin. In any case, we are dealing with the transfer of energy in the flare–background system.

REFERENCES

1. F. Farnik, J. Sylwester, and O. Likin, *Interball Mission and Payload* (Russia, 1995), p. 256.
2. S. Krucker, S. Christe, R. P. Lin, *et al.*, Solar Phys. **210**, 445 (2002).
3. O. B. Likin, N. F. Pisarenko, F. Farnik, *et al.,* Kosm. Issled. **36**, 305 (1998).
4. I. K. Mirzoeva and O. B. Likin, Preprint No. 2046, IKI RAN (Inst. Cosm. Res., Russ. Acad. Sci., Moscow, 2002).
5. I. K. Mirzoeva and O. B. Likin, Pis'ma Astron. Zh. **30**, 216 (2004).
6. N. F. Pisarenko and O. B. Likin, Izv. Ross. Akad. Nauk **59**, 37 (1995).

Translated by G. Rudnitskii

Astronomy Letters, Vol. 31, No. 1, 2005, pp. 64–72. Translated from Pis'ma v Astronomicheskiĭ Zhurnal, Vol. 31, No. 1, 2005, pp. 66–75.

A Numerical–Analytical Method for Studying the Orbital Evolution of Distant Planetary Satellites

M. A. Vashkov'yak*

Keldysh Institute of Applied Mathematics, Russian Academy of Sciences, Miusskaya pl. 4, Moscow, 125047 Russia

Received May 31, 2004

Abstract—We describe an approximate numerical–analytical method for calculating the perturbations of the elements of distant satellite orbits. The model for the motion of a distant satellite includes the solar attraction and the eccentricity and ecliptic inclination of the orbit of the central planet. In addition, we take into account the variations in planetary orbital elements with time due to secular perturbations. Our work is based on Zeipel's method for constructing the canonical transformations that relate osculating satellite orbital elements to the mean ones. The corresponding transformation of the Hamiltonian is used to construct an evolution system of equations for mean elements. The numerical solution of this system free from rapidly oscillating functions and the inverse transformation from the mean to osculating elements allows the evolution of distant satellite orbits to be studied on long time scales on the order of several hundred or thousand satellite orbital periods. © *2005 Pleiades Publishing, Inc.*

Key words: *celestial mechanics.*

INTRODUCTION. FORMULATION OF THE PROBLEM

Astronomical discoveries in recent years have shown that, apart from systems of close (inner) satellites and rings, all giant planets also have different numbers of distant (outer) satellites. The orbital evolution of distant satellites is determined mainly by the solar attraction that perturbs their Keplerian elliptical orbits. The satellite version of the restricted three-body (Sun–planet–satellite) problem, which is alternatively called Hill's problem, serves as a good model for studying the evolution of such distant orbits. Using its approximate solution by numerical, analytical, or combined (numerical–analytical) methods, we can analyze the variations in satellite orbital elements on time scales much longer than both the revolution periods of the satellites around the planet and the orbital periods of the planets themselves. In general, the analytical methods are based on the transformations of the orbital elements that eliminate the fast variables, the mean longitudes of the satellite and the perturbing body (Sun), from the new (transformed) perturbing function and that allow the evolution system of equations to be solved and (or) studied qualitatively. This system, averaged over the two fast variables, was probably first studied for the satellite version of the restricted elliptical three-body problem (Lidov 1961) and, almost simultaneously, for the more general (asteroid) version of the restricted circular problem (Kozai 1962). More rigorous equations that describe the orbital evolution of a distant planetary satellite were derived by Zeipel's method to the third power of the ratio of the mean motions of the perturbing body and the satellite, $\delta = n_1/n$. Integrating these equations in the Weierstrass (Kovalevsky 1964, 1966) and Jacobi (Orlov 1965a, 1965b) elliptic functions yielded a solution that improved the solution of Hill's double-averaged problem.

With the discoveries of increasingly distant satellites, in particular, Neptune's satellite S/2003 N1, having an orbital semimajor axis of about 0.33 AU, the need for further improving the system of evolution equations has arisen.

The goal of this paper is to construct the canonical transformations of Zeipel's method by including the next approximations of the perturbation theory, i.e., to the fourth power of δ inclusive. We use the results obtained by Orlov (1965a, 1965b, 1969, 1970a, 1970b, 1972). Unfortunately, typos in some of these publications necessitated independent cumbersome, but standard calculations. In addition, we suggest an alternative choice of the additive term in the defining function of the canonical transformation that allows certain simplifications to be made. For coherence, we provide the basic relations of Zeipel's method that are also given in the above papers.

*E-mail: vashkov@keldysh.ru

Let us consider the satellite version of the restricted elliptical three-body problem that models the motion of a distant satellite perturbed by the Sun. As the variables, we will use both the Keplerian and Delone orbital elements that are related by the standard formulas

$$L = \sqrt{\mu a}, \quad G = L\sqrt{1-e^2}, \quad H = G\cos i, \quad (1)$$
$$l = M, \quad g = \omega, \quad h = \Omega.$$

Here, μ is the product of the gravitational constant by the mass of the planet, and the following standard notation is used for the Keplerian orbital elements of the satellite: a is the semimajor axis, e is the eccentricity, i is the inclination, M is the mean anomaly, ω is the argument of the pericenter, and Ω is the longitude of the ascending node. The angular variables refer to the planetocentric ecliptic coordinate system of a certain standard epoch.

The variations in Delone elements are described by the canonical system of differential equations

$$\frac{dL}{dt} = \frac{\partial F}{\partial l}, \quad \frac{dG}{dt} = \frac{\partial F}{\partial g}, \quad \frac{dH}{dt} = \frac{\partial F}{\partial h}, \quad (2)$$
$$\frac{dl}{dt} = -\frac{\partial F}{\partial L}, \quad \frac{dg}{dt} = -\frac{\partial F}{\partial G}, \quad \frac{dh}{dt} = -\frac{\partial F}{\partial H}.$$

Here, the Hamiltonian F of the problem is the sum of the unperturbed Hamiltonian F_0 and the perturbing function F_1:

$$F = F_0(L) + F_1(L, l, G, g, H, h, t), \quad (3)$$

where $F_0 = \mu^2/2L^2$ and $-\partial F_0/\partial L = \mu^2/L^3 = n$ is the mean motion of the satellite.

The explicit dependence of the function F_1 on time t is related to the heliocentric motion of the planet (or the planetocentric motion of the perturbing body, the Sun). The planets actually move in nearly circular orbits slightly inclined to the plane of the ecliptic, the principal coordinate plane. The proposed method includes not only the deviations of the planetary motions from the plane and circular ones, but also the variations in eccentricity e_1, inclination i_1, longitude of the pericenter π_1, and ascending node Ω_1 of the planetary orbit in accordance with the Lagrange–Brauer–Wurkom theory of secular perturbations. The corresponding principal terms $\sim\delta^2 e_1$, $\delta^2 e_1^2$, $\delta^2 \sin i_1$, $\delta^2 \sin^2 i_1$, and $\delta^2 e_1 a/a_1$ were included in the perturbing function F_1. For simplicity, we will present the canonical transformation procedure only for $e_1 = i_1 = 0$ and additionally describe the modifications of the formulas needed to incorporate the variations in eccentricity and inclination.

Under these simplified assumptions, the perturbing function of Hill's problem is defined by

$$F_1 = \frac{\mu_1}{2a_1^3}\left[\frac{3}{2}(x^2+y^2) - r^2 + \frac{3}{2}(x^2-y^2)\cos 2\lambda_1 + 3xy\sin 2\lambda_1\right]. \quad (4)$$

The rectangular coordinates x and y of the satellite and its radius vector r in the planetocentric ecliptic coordinate system are related to the Keplerian orbital elements by the standard formulas for unperturbed motion, while the Keplerian and Delone elements are related by formulas (1). The coordinates x, y, and r depend on the slowly varying satellite orbital elements and on the fast variable l. In formula (4), μ_1 is the product of the gravitational constant by the mass of the perturbing body (the Sun), a_1 is the radius of the circular orbit of the planet, and λ_1 is its mean ecliptic longitude defined by

$$\lambda_1(t) = \lambda_{10} + n_1(t - t_0), \quad (5)$$

where $n_1 = \dfrac{\sqrt{\mu_1+\mu}}{a_1^{3/2}}$ is the mean motion of the planet, t_0 is the initial time, and $\lambda_{10} = \lambda_1(t_0)$. It is probably impossible to obtain an exact analytical solution of Eqs. (2), while the presence of the variables l and λ_1 in the function F_1 that vary with the frequencies n and $n\delta$, respectively, severely complicates the numerical integration of these equations.

The main problem solved by Zeipel's method is finding the canonical transformations of the orbital elements that would sequentially eliminated the variables l and λ_1 from the transformed Hamiltonian. The transformed canonical equations whose right-hand sides contain no rapidly oscillating functions of time could then be numerically integrated with much greater efficiency or could be approximately solved analytically. The idea of an analytical transformation of the canonical equations followed by their numerical integration could be found in many studies that were initiated more than thirty years ago (see, e.g., Lidov 1978).

Clearly, the ratio $|F_1|/F_0$ in (3) is small and is determined by

$$\varepsilon \sim \frac{\mu_1 a^3}{\mu a_1^3} = \frac{n_1^2\gamma}{n^2} = \gamma\delta^2,$$

where $\gamma = (1+\mu/\mu_1)^{-1}$, $\delta = n_1/n$.

For Neptune's satellite S/2003 N1, the most distant planetary satellite known to date, ε is about 0.025 and $\delta \sim \sqrt{\varepsilon} \approx 0.16$. In this case, in addition to the first approximation of the perturbation theory, the next several approximations should also be included to accurately describe the orbital evolution.

BASIC RELATIONS OF ZEIPEL's METHOD

The following presentation has much in common with that of Orlov (1965a), but differs by methodological details.

At the first stage, we perform such a canonical transformation of the variables (L, l, G, g, H, h) to the variables (L', l', G', g', H', h') using the defining function $S(L', l, G', g, H', h, t)$, so that the new Hamiltonian F^* does not contain the fast variable l, i.e., $F^* = F^*(L', -, G', g', H', h', \lambda_1(t))$. The new (with a prime) and initial variables are related by the canonical transformation formulas

$$L = \frac{\partial S}{\partial l}, \quad G = \frac{\partial S}{\partial g}, \quad H = \frac{\partial S}{\partial h}, \tag{6}$$
$$l' = \frac{\partial S}{\partial L'}, \quad g' = \frac{\partial S}{\partial G'}, \quad h' = \frac{\partial S}{\partial H'}.$$

The functions F^* and S are assumed to be representable as a power series of ε:

$$F^* = F_0^* + F_1^* + F_2^* + \ldots, \tag{7}$$
$$S = S_0 + S_1 + S_2 + \ldots,$$

where $|F_k^*/F_0^*| \sim \varepsilon^k$, $|S_k/S_0| \sim \varepsilon^k$, $k = 0, 1, 2$.

According to Zeipel's method, a chain of sequentially solvable equations is obtained for the functions F_k^* and S_k. These equations for $k = 0, 1, 2$ are

$$F_0^*(L') = F_0(L'), \quad S_0 = L'l + G'g + H'h, \tag{8}$$
$$F_1^*(L', l, G', g, H', h, \lambda_1(t)) - \frac{\partial F_0}{\partial L'}\frac{\partial S_1}{\partial l} + \frac{\partial S_1}{\partial t}$$
$$= F_1(L', l, G', g, H', h, \lambda_1(t)),$$
$$F_2^*(L', l, G', g, H', h, \lambda_1(t)) - \frac{\partial F_0}{\partial L'}\frac{\partial S_2}{\partial l} + \frac{\partial S_2}{\partial t}$$
$$= \frac{1}{2}\frac{\partial^2 F_0^*}{\partial L'^2}\left(\frac{\partial S_1}{\partial l}\right)^2 - \frac{\partial F_1^*}{\partial l}\frac{\partial S_1}{\partial L'} - \frac{\partial F_1^*}{\partial g}\frac{\partial S_1}{\partial G'}$$
$$- \frac{\partial F_1^*}{\partial h}\frac{\partial S_1}{\partial H'} + \frac{\partial F_1}{\partial L'}\frac{\partial S_1}{\partial l} + \frac{\partial F_1}{\partial G'}\frac{\partial S_1}{\partial g} + \frac{\partial F_1}{\partial H'}\frac{\partial S_1}{\partial h}.$$

The condition for the function F_1^* to be independent of l will be satisfied if it is defined as

$$F_1^* = \frac{1}{2\pi}\int_0^{2\pi} F_1 dl. \tag{9}$$

The function S_1 can then be derived from the equation

$$\frac{\mu^2}{L'^3}\frac{\partial S_1}{\partial l} + \frac{\partial S_1}{\partial t} = F_1 - F_1^*. \tag{10}$$

Since the change of variables (6) is chosen to be close to the identical one and since the functions S_k for $k \geq 1$ are assumed to be 2π-periodic in mean anomaly l, the short-period variations in orbital elements (or the function S) can be determined with a lower accuracy than the function F^*. Below, we set $S_2 = 0$. Given that F_1^* does not depend on l and imposing the additional condition $\int_0^{2\pi} S_1 dl = 0$ on the function S_1, which allows the appearance of secular terms in the next approximations to be avoided, we obtain

$$F_2^*(L', -, G', g, H', h, \lambda_1(t)) \tag{11}$$
$$= \frac{1}{2\pi}\int_0^{2\pi}\left[\frac{3\mu^2}{2L'^4}\left(\frac{\partial S_1}{\partial l}\right)^2 + \frac{\partial F_1}{\partial L'}\frac{\partial S_1}{\partial l}\right.$$
$$\left. + \frac{\partial F_1}{\partial G'}\frac{\partial S_1}{\partial g} + \frac{\partial F_1}{\partial H'}\frac{\partial S_1}{\partial h}\right] dl.$$

Since the variable h appears in the functions F_1, S_1, and, hence, F^* only via the combination

$$\eta = h - \lambda_1(t) \tag{12}$$

for the subsequent transformations, it is convenient to consider the quantity $\eta' = h' - \lambda_1(t)$ as a new canonical variable. We then represent the new Hamiltonian

$$\Phi = F^*(L', -, G', g', H', \eta') + n_1 H', \tag{13}$$

as a power series of the parameter δ:

$$\Phi = \Phi_0 + \Phi_1 + \Phi_2 + \Phi_3 + \Phi_4, \tag{14}$$

where $|\Phi_k/\Phi_0| \sim \delta^k = (n_1/n)^k$,

$$\Phi_0 = F_0^* = \frac{\mu^2}{2L'^2}, \quad \Phi_1 = n_1 H', \tag{15}$$
$$\Phi_2 = F_1^*(L', -, G', g', H', \eta'),$$
$$\Phi_3 = 0, \quad \Phi_4 = F_2^*(L', -, G', g', H', \eta').$$

At the second stage, we construct the canonical transformation that eliminates η' from the new (transformed) Hamiltonian. The variables (L', l', G', g', H', η') can be transformed to the variables $(L'', l'', G'', g'', H'', \eta'')$ using the defining function $s(L'', l', G'', g', H'', \eta')$ in such a way that the new Hamiltonian Φ^* will contain neither l'' nor η'', i.e.,

$$\Phi^* = \Phi^*(L'', -, G'', g'', H'', -). \tag{16}$$

Under the assumption of $e_1 = \sin i_1 = 0$, the canonical equations with Hamiltonian (16) have the three first integrals

$$L'' = \text{const}, \quad H'' = \text{const}, \quad \Phi^* = \text{const}. \tag{17}$$

The new (with two primes) and old (with one prime) variables are related by canonical transformation formulas similar to (6):

$$L' = \frac{\partial s}{\partial l'}, \quad G' = \frac{\partial s}{\partial g'}, \quad H' = \frac{\partial s}{\partial \eta'}, \tag{18}$$
$$l'' = \frac{\partial s}{\partial L''}, \quad g'' = \frac{\partial s}{\partial G''}, \quad \eta'' = \frac{\partial s}{\partial H''}.$$

The fundamental difference between the second and first stages is that twice as many approximations are required to achieve an accuracy of $\varepsilon^2 \approx \delta^4$. This is because the new Hamiltonian Φ^* and the transformation function s are representable as power series of $\delta \approx \sqrt{\varepsilon}$ (in contrast to the functions F^* and S (7)), i.e.,

$$\Phi^* = \Phi_0^* + \Phi_1^* + \Phi_2^* + \Phi_3^* + \Phi_4^* + \ldots, \quad (19)$$
$$|\Phi_k^*/\Phi_0^*| \sim \delta^k,$$
$$s = s_0 + s_1 + s_2 + s_3 + s_4 + \ldots, \quad |s_k/s_0| \sim \delta^k.$$

A chain of equations that slightly differs from (8) even for $k \le 2$ is obtained for the functions Φ_k^* and s_k:

$$\Phi_0^*(L'') = \Phi_0(L'') = \frac{\mu^2}{2L''^2}, \quad (20)$$
$$s_0 = L''l' + G''g' + H''\eta',$$
$$\Phi_1^*(H'') = \Phi_1(H'') = n_1 H'',$$
$$\Phi_2^*(L'', -, G'', g', H'', -)$$
$$= n_1\frac{\partial s_1}{\partial \eta'} + \Phi_2(L'', -, G'', g', H'', \eta').$$

The condition for the function Φ_2^* to be independent of η' will be satisfied if it is defined as

$$\Phi_2^* = \frac{1}{2\pi}\int_0^{2\pi}\Phi_2 d\eta'. \quad (21)$$

The function s_1 is then defined by

$$s_1 = -\frac{1}{n_1}\int(\Phi_2 - \Phi_2^*)d\eta' \quad (22)$$

and by the conditions

$$s_1(\eta' + 2\pi) = s_1(\eta'), \quad \int_0^{2\pi} s_1 d\eta' = 0, \quad (23)$$

similar to those for the function S_1.

The next approximation for δ yields expressions for

$$\Phi_3^* = \frac{1}{2\pi}\int_0^{2\pi}\left[\frac{\partial\Phi_2}{\partial G''}\frac{\partial s_1}{\partial g'} + \frac{\partial\Phi_2}{\partial H''}\frac{\partial s_1}{\partial \eta'}\right]d\eta' \quad (24)$$

and for the 2π-periodic (in η') function

$$s_2 = -\frac{1}{n_1}\int\left\{\left[\frac{\partial\Phi_2}{\partial G''}\frac{\partial s_1}{\partial g'}\right.\right. \quad (25)$$
$$\left.\left. + \frac{\partial\Phi_2}{\partial H''}\frac{\partial s_1}{\partial \eta'} - \frac{\partial\Phi_2^*}{\partial g'}\frac{\partial s_1}{\partial G''}\right] - \Phi_3^*\right\}d\eta'.$$

Finally, given conditions (23), the following expression is derived for Φ_4^*:

$$\Phi_4^* = \frac{1}{2\pi}\int_0^{2\pi}\left[\frac{\partial\Phi_2}{\partial G''}\frac{\partial s_2}{\partial g'} + \frac{\partial\Phi_2}{\partial H''}\frac{\partial s_2}{\partial \eta'}\right. \quad (26)$$
$$+ \frac{1}{2}\frac{\partial^2\Phi_2}{\partial G''^2}\left(\frac{\partial s_1}{\partial g'}\right)^2 + \frac{1}{2}\frac{\partial^2\Phi_2}{\partial H''^2}\left(\frac{\partial s_1}{\partial \eta'}\right)^2$$
$$\left. + \frac{\partial^2\Phi_2}{\partial G''\partial H''}\frac{\partial s_1}{\partial g'}\frac{\partial s_1}{\partial \eta'} - \frac{1}{2}\frac{\partial^2\Phi_2^*}{\partial g'^2}\left(\frac{\partial s_1}{\partial G''}\right)^2 + \Phi_4\right]d\eta';$$

below, we disregard the periodic function s_3.

DESCRIPTION OF THE PROCEDURE FOR CONSTRUCTING THE CANONICAL TRANSFORMATIONS

Calculating the Functions F_1^* and S_1

In the problem under consideration, it is convenient to go from the mean anomaly l to the eccentric anomaly E to perform the necessary analytical transformations and to use the following relations in calculating the integrals and the derivatives:

$$\frac{\partial E}{\partial l} = \frac{1}{1 - e\cos E}, \quad \frac{\partial E}{\partial e} = \frac{\sin E}{1 - e\cos E}. \quad (27)$$

In addition, we will need the formulas for the derivatives of the Keplerian elements with respect to the Delone elements

$$\frac{\partial a}{\partial L} = \frac{2L}{\mu}, \quad \frac{\partial e}{\partial L} = \frac{1 - e^2}{eL}, \quad \frac{\partial e}{\partial G} = -\frac{\sqrt{1 - e^2}}{eL}, \quad (28)$$
$$\frac{\partial i}{\partial G} = \frac{ctgi}{G}, \quad \frac{\partial i}{\partial H} = -\frac{1}{G\sin i},$$

and the expressions for the derivative of some complex function of the Keplerian elements, $\varphi(a, e(L, G), i(G, H), E(e(L, G), l), g, h)$,

$$\frac{\partial\varphi}{\partial L} = \frac{\partial\varphi}{\partial a}\frac{\partial a}{\partial L} + \frac{\partial\varphi}{\partial e}\frac{\partial e}{\partial L} + \frac{\partial\varphi}{\partial E}\frac{\partial E}{\partial e}\frac{\partial e}{\partial L}, \quad (29)$$
$$\frac{\partial\varphi}{\partial G} = \frac{\partial\varphi}{\partial e}\frac{\partial e}{\partial G} + \frac{\partial\varphi}{\partial i}\frac{\partial i}{\partial G} + \frac{\partial\varphi}{\partial E}\frac{\partial E}{\partial e}\frac{\partial e}{\partial G},$$
$$\frac{\partial\varphi}{\partial H} = \frac{\partial\varphi}{\partial i}\frac{\partial i}{\partial H}, \quad \frac{\partial\varphi}{\partial l} = \frac{\partial\varphi}{\partial E}\frac{\partial E}{\partial l};$$

$\frac{\partial\varphi}{\partial g}$ and $\frac{\partial\varphi}{\partial h}$ are calculated from the explicit arguments. All of the following expressions required for the transformations are given as functions of a, e, i, E, g, and h, implying the dependences

$$a = \frac{L^2}{\mu}, \quad e = \sqrt{1 - \frac{G^2}{L^2}},$$

$$\cos i = \frac{H}{G}, \quad E - e\sin E = l.$$

The initial expression (4) for the perturbing function F_1 takes the form

$$F_1 = \frac{\mu_1 a^2}{2a_1^3}\sum_{j=0}^{3} A_j(i,g,\eta)D_j(e,E), \qquad (30)$$

where

$$D_0 = -1 + 2e\cos E - e^2\cos^2 E, \qquad (31)$$
$$D_1 = \frac{3}{4}(\cos^2 E - 2e\cos E + e^2),$$
$$D_2 = \frac{3}{4}(1-e^2)\sin^2 E,$$
$$D_3 = -\frac{3}{2}\sqrt{1-e^2}(\cos E - e)\sin E,$$
$$A_0 = 1, \quad A_j = A_j^{(0)} + A_j^{(1)}\cos 2\eta + \bar{A}_j^{(1)}\sin 2\eta,$$
$$j = 1,2,3;$$
$$A_1^{(0)} = 2 - \sin^2 i + \sin^2 i\cos 2g,$$
$$A_2^{(0)} = 2 - \sin^2 i - \sin^2 i\cos 2g,$$
$$A_3^{(0)} = \sin^2 i\sin 2g,$$
$$A_1^{(1)} = \sin^2 i + (2-\sin^2 i)\cos 2g,$$
$$A_2^{(1)} = \sin^2 i - (2-\sin^2 i)\cos 2g,$$
$$A_3^{(1)} = (2-\sin^2 i)\sin 2g,$$
$$\bar{A}_1^{(1)} = -2\cos i\sin 2g, \quad \bar{A}_2^{(1)} = 2\cos i\sin 2g,$$
$$\bar{A}_3^{(1)} = 2\cos i\cos 2g.$$

Calculating the function F_1^* using formula (9) yields the expression

$$F_1^* = \frac{3\mu_1 a'^2}{8a_1^3}\left\{\frac{2}{3} + e'^2 - \sin^2 i' \right. \qquad (32)$$
$$+ \frac{1}{2}e'^2\sin^2 i'(5\cos 2g' - 3) + \frac{1}{2}[(2+3e'^2)\sin^2 i'$$
$$+ 5e'^2(2-\sin^2 i')\cos 2g']\cos 2\eta'$$
$$\left. - 5e'^2\cos i'\sin 2g'\sin 2\eta'\right\},$$

in which a', e', and i' must be expressed in terms of L', G', and H'.

After the difference $F_1 - F_1^*$ has been set up, the right-hand side of Eq. (10) becomes a known function of the eccentric anomaly E and the time t, which appears via λ_1, and the equation itself may be written as

$$\frac{\partial S_1}{\partial l} - \frac{n_1}{n'}\frac{\partial S_1}{\partial \eta} = \frac{1}{n'}(F_1 - F_1^*), \qquad (33)$$

where $n' = \mu^2/L'^3$. To solve this equation, it would be appropriate to use the method that was described by Lidov (1978) and that represents the function S_1 as a power series of the parameter $\delta \approx n_1/n'$, i.e.,

$$S_1 = S_1^{(0)} + S_1^{(1)} + \ldots, \qquad (34)$$

where $S_1^{(r)}$ has an order $\delta^{r>0}$ relative to $S_1^{(0)}$. The following system of sequentially solvable equations is then obtained for $S_1^{(r)}$:

$$\frac{\partial S_1^{(0)}}{\partial l} = \frac{1}{n'}(F_1 - F_1^*), \quad r = 0, \qquad (35)$$
$$\frac{\partial S_1^{(r)}}{\partial l} = \delta\frac{\partial S_1^{(r-1)}}{\partial \eta}, \quad r > 0$$

at $S_1^{(r)}(l+2\pi) = S_1^{(r)}(l)$, $\int_0^{2\pi} S_1^{(r)} dl = 0$, $r = 0,1,2,\ldots$.

Here, the above method was used for $r = 0, 1$. Since the function $S_1^{(0)}$ itself has an order $\varepsilon \sim \delta^2$, the terms of the order of $\delta^4 \sim \varepsilon^2$ or higher, i.e., of the same order as S_2, S_3, …, were discarded in the resulting function S. Below, we provide explicit expressions for the functions $S_1^{(0)}$ and $S_1^{(1)}$:

$$S_1^{(0)} = \frac{\mu_1 a'^2}{2a_1^3 n'}\left\{\frac{1}{16}[A_1A_4 + (1-e'^2)A_2A_5] \right. \qquad (36)$$
$$\left. - \frac{3}{2}\sqrt{1-e'^2}A_3A_6 + A_7\right\},$$

where A_j for $j = 1,2,3$ can be determined from formulas (31) by substituting i' for i, while for $j = 4,5,6,7$,

$$A_4 = 3e'(4e'^2 - 9)\sin E \qquad (37)$$
$$+ 3(1+2e'^2)\sin 2E - e'\sin 3E,$$
$$A_5 = 3e'\sin E - 3\sin 2E + e'\sin 3E,$$
$$A_6 = \frac{5}{8}e'^2 + \frac{5}{4}e'\cos E$$
$$- \frac{1}{4}(1+e'^2)\cos 2E + \frac{1}{12}e'\cos 3E,$$
$$A_7 = e'\left(2 - \frac{3}{4}e'^2\right)\sin E$$
$$- \frac{3}{4}e'^2\sin 2E + \frac{1}{12}e'^3\sin 3E,$$

$$S_1^{(1)} = \frac{\mu_1 a'^2 n_1}{a_1^3 n'^2} \qquad (38)$$
$$\times\left\{\frac{1}{16}[B_1B_4 + (1-e'^2)B_2B_5] - \frac{3}{2}\sqrt{1-e'^2}B_3B_6\right\},$$

where

$$B_1 = A_1^{(1)}\sin 2\eta - \bar{A}_1^{(1)}\cos 2\eta, \qquad (39)$$
$$B_2 = A_2^{(1)}\sin 2\eta - \bar{A}_2^{(1)}\cos 2\eta,$$

$$B_3 = -A_3^{(1)}\sin 2\eta + \bar{A}_3^{(1)}\cos 2\eta,$$

$$B_4 = -\frac{57}{4}e'^2 + \frac{9}{2}e'^4 + \frac{3}{2}e'(6e'^2 - 19)\cos E + \frac{1}{2}(3 + 20e'^2 - 6e'^4)\cos 2E - \frac{1}{6}e'(5 + 6e'^2)\cos 3E + \frac{1}{8}e'^2\cos 4E,$$

$$B_5 = \frac{9}{4}e'^2 + \frac{9}{2}e'\cos E - \frac{1}{2}(3 + 2e'^2)\cos 2E + \frac{5}{6}e'\cos 3E - \frac{1}{8}e'^2\cos 4E,$$

$$B_6 = \frac{1}{8}e'(11 - 4e'^2)\sin E - \frac{1}{24}(3 + 11e'^2)\sin 2E - \frac{1}{72}e'(1 + 3e'^2)\sin 3E + \frac{1}{96}e'^2\sin 4E.$$

The coefficients $A_1^{(1)}, \ldots, \bar{A}_3^{(1)}$ are defined by formulas (31) where i' should be substituted for i. Note that an expression for the function $S_1^{(0)}$ was derived by Orlov (1965a), while the function $S_1^{(1)}$ supplements it with terms of the order of δ^3 or $\varepsilon^{3/2}$.

Since the transformation function S in Zeipel's method depends on both the old and new (primed) elements, we must in practice solve Eqs. (6) that define the canonical change of variables by using an iterative procedure. This is absolutely necessary for constructing the second approximation in ε, i.e., for calculating the function F_2^*. Since this expression is cumbersome and only intermediate, it is not provided here and will be used to calculate integral (26).

Calculating the Functions Φ_2^*, s_1, Φ_3^*, s_2, Φ_4^*

According to formulas (21), (22), (24), and (25), the functions Φ_2^*, s_1, Φ_3^*, and s_2 are defined by

$$\Phi_2^* = \frac{3\mu_1 a''^2}{8a_1^3}\left[\frac{2}{3} + e''^2 - \sin^2 i'' + \frac{1}{2}e''^2\sin^2 i''(5\cos 2g'' - 3)\right], \quad (40)$$

$$s_1 = -\frac{3\mu_1 a''^2}{32a_1^3 n_1}\{[(2 + 3e''^2)\sin^2 i'' + 5e''^2(2 - \sin^2 i'')\cos 2g']\sin 2\eta' + 10e''^2\cos i''\sin 2g'\cos 2\eta'\} + \Delta s_1, \quad (41)$$

$$\Phi_3^* = \frac{9\mu_1^2 a''^{7/2}}{128a_1^6 n_1\sqrt{\mu}}\sqrt{1 - e''^2}\cos i''\{50e''^2 + \sin^2 i''[2 + e''^2(15\cos 2g'' - 17)]\} \quad (42)$$

(the function Φ_2^* (40) is the Hamiltonian of Hill's double-averaged problem obtained by Lidov (1961), while the function Φ_3^* (42) was obtained by Orlov (1965a) and supplements the Hamiltonian with a term of the order δ^3),

$$s_2 = \frac{9\mu_1^2 a''^{7/2}}{512a_1^6 n_1^2\sqrt{\mu}\sqrt{1 - e''^2}} \quad (43)$$
$$\times\left\{40e''^2(1 - e''^2)(2\sin^2 i'' - 1)\sin 2g'\cos 2\eta'\right.$$
$$- 2\cos i''(1 - e''^2)[2(17e''^2 - 2)\sin^2 i'' + 10e''^2(2 - 3\sin^2 i'')\cos 2g']\sin 2\eta'$$
$$+ e''^2\left[\sin^2 i''\left(-15 + 15e''^2 + \frac{25}{2}\sin^2 i''\right)\sin 2g'\right.$$
$$+\left\langle 50e''^2 - 50 + \frac{25}{4}\sin^2 i''(8 - 6e''^2 - \sin^2 i'')\right\rangle$$
$$\times\left.\sin 4g'\right]\cos 4\eta' - \cos i''\left[\frac{1}{2}(2 + 3e''^2)^2\sin^2 i'' + 15e''^2(1 - e''^2)\sin^2 i''\cos 2g' + \frac{25}{2}e''^2\langle 4 - 4e''^2 + (e''^2 - 2)\sin^2 i''\rangle\cos 4g'\right]\sin 4\eta'\left.\right\} + \Delta s_2.$$

Here, the elements a'', e'', and i'' are related to the elements L'', G'', and H'' by the first three formulas in (1).

As regards the functions s_1 and s_2, they are generally determined to the additive terms Δs_1 and Δs_2 that do not depend on η'. To satisfy the second of conditions (23) in formula (41), these terms were set equal to zero. As regards the function s_2, the corresponding additive terms can be chosen in such a way as to simplify the expression for Φ_4^*, when possible. Based on the form of s_2 given by formula (43), we will seek Δs_2 in the form

$$\Delta s_2 = \frac{\mu_1^2 a''^{7/2}}{a_1^6 n_1^2\sqrt{\mu}}[A(G'', H'')\sin 2g' + B(G'', H'')\sin 4g']. \quad (44)$$

The η'-independent terms should then be added to expression (26) written for $\Delta s_2 = 0$:

$$\Delta\Phi_4^* = -\frac{\partial\Phi_2^*}{\partial g'}\frac{\partial\Delta s_2}{\partial G''} + \frac{1}{2\pi}\frac{\partial\Delta s_2}{\partial g'}\int_0^{2\pi}\frac{\partial\Phi_2}{\partial G''}d\eta'. \quad (45)$$

The form of the coefficients A and B in formula (44) is determined by the conditions that simplify the function Φ_4^* or, more specifically, by the absence of terms proportional to $\cos 6g$ and $\gamma\cos 4g$ in it. Since,

according to (17), $H'' = \text{const}$, the following linear inhomogeneous differential equation is obtained for $A(G'')$:

$$\frac{\partial A}{\partial G''} + f(G'')A = \varphi(G'')$$

with the known functions f and φ. The equation that defines $B(G'')$ has a similar form, but with different functions f and φ. Once A and B have been determined from these equations, the function Δs_2 takes the form

$$\Delta s_2 = \frac{225\mu_1^2 a''^{7/2} e''^2 \sin^2 i''}{2048 a_1^6 n_1^2 \sqrt{\mu(1-e''^2)}}[2(2e''^2 - \sin^2 i'')\sin 2g' + \sin^2 i'' \sin 4g']. \quad (46)$$

Substituting the derivatives $\partial\Delta s_2/\partial G''$ and $\partial\Delta s_2/\partial g'$ in the expression for $\Delta\Phi_4^*$ (45), adding it to (26), and setting (with the accuracy admissible in this fourth approximation) $\gamma = 1$, we obtain

$$\Phi_4^* = \frac{\mu_1^2 a''^5}{\mu a_1^6}\left\{-\frac{49}{64} + \frac{4167}{256}e''^2 - \frac{10773}{1024}e''^4 + \left(\frac{177}{256} - \frac{8469}{512}e''^2 + \frac{14183}{2048}e''^4\right)\sin^2 i'' + \left(\frac{9}{1024} + \frac{15759}{2048}e''^2 - \frac{26019}{4096}e''^4\right)\sin^4 i'' + \left[\frac{549}{64} - \frac{10935}{2048}e''^2 + \left(-\frac{15795}{2048} + \frac{12105}{2048}e''^2\right)\sin^2 i''\right] e''^2 \sin^2 i'' \times \cos 2g'' + \frac{1845}{4096}e''^4 \sin^4 i'' \cos 4g''\right\}. \quad (47)$$

Allowance for the Eccentricity and Ecliptic Inclination of the Orbit of the Sun (the Central Planet)

It follows from the theory of the secular perturbations of planetary orbits that the maximum orbital eccentricities of the giant planets e_1 can reach about 0.01 (for Neptune) and 0.08 (for Saturn). The maximum orbital inclination to the ecliptic i_1 can reach about 2°.0 (for Jupiter) and 2°.7 (for Neptune). The periods of the variations in these elements, as well as in the longitudes of the perihelia and the ascending nodes of the planetary orbits, are about 50 000 for Jupiter and Saturn, 450 000 for Uranus, and 1.9 Myr for Neptune.

The influence of i_1 is taken into account within the framework of the procedure described above. The formulas derived by A.A. Orlov are generalized to the case of low (but finite) inclinations i_1, which vary with time, just as Ω_1 does. To allow for the influence of e_1, the canonical system with the transformed Hamiltonian F^* is formally supplemented with the pair of functions

$$\frac{dK'}{dt} = \frac{\partial\Phi'}{\partial\chi'}, \quad \frac{d\chi'}{dt} = -\frac{\partial\Phi'}{\partial K'} = n_1$$

for the new canonically conjugate variables K' and χ'. The new Hamiltonian Φ' of the expanded system of equations is defined by

$$\Phi' = F^* - n_1 K'.$$

The details of the subsequent transformations can be found in the paper by Orlov (1969).

Allowance for the influence of e_1 and i_1 on the evolution of a satellite orbit results in a modification of the functions S, Φ^*, and s. With the adopted degree of accuracy, it will suffice to modify only formulas (36) for $S_1^{(0)}$, (40) for Φ_2^*, and (41) for s_1.

The new expression for $S_1^{(0)}$ is

$$S_1^{(0)} = \frac{\mu_1 a'^2}{2r_1^3 n'}\left\{T_0\left[\left(-2 + \frac{3}{4}e'^2\right)e'\sin E + \frac{3}{4}e'^2\sin 2E - \frac{1}{12}e'^3\sin 3E\right] + T_1\left[\left(-\frac{5}{2} + \frac{5}{4}e'^2\right)e'\sin E + \left(\frac{1}{2} + \frac{1}{4}e'^2\right)e'^2\sin 2E + \left(-\frac{1}{6} + \frac{1}{12}e'^2\right)e'\sin 3E\right] + T_2\sqrt{1-e'^2}\left[\frac{5}{4}e'^2 + \frac{5}{2}e'\cos E - \left(\frac{1}{2} + \frac{1}{2}e'^2\right)\cos 2E + \frac{1}{6}e'\cos 3E\right]\right\}, \quad (48)$$

where

$$T_0 = -1 + \frac{3}{4}\alpha_1^2(1 + \cos^2 i' + \sin^2 i'\cos 2h) + \frac{3}{4}\beta_1^2(1 + \cos^2 i' - \sin^2 i'\cos 2h) + \frac{3}{2}\gamma_1^2\sin^2 i' + \frac{3}{2}\alpha_1\beta_1\sin^2 i'\sin 2h - 3\gamma_1\sin i'\cos i'(\alpha_1\sin h - \beta_1\cos h), \quad (49)$$

$$T_1 = \frac{3}{2}\alpha_1^2\{[\sin^2 i' + (1+\cos^2 i')\cos 2h]\cos 2q - 2\cos i'\sin 2g\sin 2h\} + \frac{3}{2}\beta_1^2\{[\sin^2 i' - (1+\cos^2 i')\cos 2h]\cos 2q + 2\cos i'\sin 2g\sin 2h\} - \frac{3}{4}\gamma_1^2\sin^2 i'\cos 2g + \frac{3}{2}\alpha_1\beta_1[(1+\cos^2 i')\cos 2g$$

$$\times \sin 2h + 2\cos i' \sin 2g \cos 2h]$$
$$+ 3\gamma_1 \sin i'[\alpha_1(\cos i' \cos 2g \sin h + \sin 2g \cos h)$$
$$- \beta_1(\cos i' \cos 2g \cos h - \sin 2g \sin h)],$$
$$T_2 = -\frac{3}{2}\alpha_1^2\{[\sin^2 i' + (1+\cos^2 i')\cos 2h]\sin 2g$$
$$+ 2\cos i' \cos 2g \sin 2h\} - \frac{3}{2}\beta_1^2\{[\sin^2 i'$$
$$- (1+\cos^2 i')\cos 2h]\sin 2g - 2\cos i' \cos 2g \sin 2h\}$$
$$+ \frac{3}{4}\gamma_1^2 \sin^2 i' \sin 2g - \frac{3}{2}\alpha_1\beta_1[(1+\cos^2 i')\sin 2g$$
$$\times \sin 2h - 2\cos i' \cos 2g \cos 2h]$$
$$- 3\gamma_1 \sin i'[\alpha_1(\cos i' \sin 2g \sin h - \cos 2g \cos h)$$
$$- \beta_1(\cos i' \sin 2g \cos h + \cos 2g \sin h)],$$
$$\alpha_1 = \cos u_1 \cos\Omega_1 - \sin u_1 \sin\Omega_1 \cos i_1,$$
$$\beta_1 = \cos u_1 \sin\Omega_1 + \sin u_1 \cos\Omega_1 \cos i_1,$$
$$\gamma_1 = \sin u_1 \sin i_1, \quad r_1 = \frac{a_1(1-e_1^2)}{1+e_1\cos\theta_1},$$
$$u_1 = \theta_1 + \omega_1.$$

In formulas (49), θ_1 is the true anomaly of the planet, and ω_1 is the argument of the perihelion of the planetary orbit changed by 180°.

The new expression for Φ_2^* is

$$\Phi_2^* = \frac{3\mu_1 a''^2}{16 a_1^3 (1-e_1^2)^{3/2}}\left[\frac{4}{3} + W^{(0)}\right. \tag{50}$$
$$\left. + W^{(1)}\sin 2i_1 + W^{(2)}\sin^2 i_1 + e_1 W^{(3)}\right].$$

The formulas for $W^{(0)}$, $W^{(1)}$, $W^{(2)}$, and $W^{(3)}$ were obtained previously by Lidov (1961), Orlov (1972), and Vashlov'yak and Teslenko (1998):

$$W^{(0)} = 2e''^2 + (5e''^2\cos 2g'' - 2 - 3e''^2)\sin^2 i'', \tag{51}$$
$$W^{(1)} = -[5e''^2 \sin 2g'' \sin(\Omega_1 - \Omega'')$$
$$+ (5e''^2\cos 2g'' - 2 - 3e''^2)$$
$$\times \cos i'' \cos(\Omega_1 - \Omega'']\sin i'',$$
$$W^{(2)} = -2 - 3e''^2 - \frac{1}{2}[3 + \cos 2(\Omega_1 - \Omega'')]$$
$$\times (5e''^2\cos 2g'' - 2 - 3e''^2)\sin^2 i''$$
$$+ 5e''^2[\cos 2g'' \cos 2(\Omega_1 - \Omega'')$$
$$+ \sin 2g'' \cos i'' \sin 2(\Omega_1 - \Omega'')],$$
$$W^{(3)} = \frac{5a''e''}{16a_1(1-e_1^2)}\{(4+3e''^2)[(5\sin^2 i'' - 4)$$
$$\times \cos g'' \cos(\Omega'' - \pi_1)$$
$$+ (4 - 15\sin^2 i'')\cos i'' \sin g'' \sin(\Omega'' - \pi_1)]$$
$$+ 35e''^2 \sin^2 i''[\cos i'' \sin 3g'' \sin(\Omega'' - \pi_1)$$
$$- \cos 3g'' \cos(\Omega'' - \pi_1)]\},$$

where $\pi_1 = \Omega_1 + \omega_1 + 180°$ is the heliocentric longitude of the pericenter of the planetary orbit changed by 180°. The function $W^{(3)}$ describes the secular perturbations from the first parallactic term of the perturbing function $\sim(a/a_1)^3$.

For the function s_1, we obtain a more complex expression to replace (41):

$$s_1 = \frac{3\mu_1 a''^2}{16 a_1^3 n_1 (1-e_1^2)^{3/2}}\left\{\left(1 + \frac{3}{2}e''^2\right)\left[\sum_{j=1}^{3} P_j J_j\right.\right. \tag{52}$$
$$\left. + \frac{1}{8}e_1^2(P_2 \sin 2\omega_1 - P_3 \cos 2\omega_1)\right]$$
$$+ \frac{5}{2}e_1^2\left[\sum_{j=1}^{3} Q_j J_j\right.$$
$$\left.\left. + \frac{1}{8}e_1^2(Q_2 \sin 2\omega_1 - Q_3 \cos 2\omega_1)\right]\right\}.$$

In this expression, $J_1 = \theta_1 - M_1 + e_1 \sin\theta_1$, M_1 is the mean anomaly of the planet,

$$J_2 = \frac{1}{2}\Big[e_1 \sin(u_1 + \omega_1)$$
$$+ \sin 2u_1 + \frac{e_1}{3}\sin(3u_1 - \omega_1)\Big],$$
$$J_3 = -\frac{1}{2}\Big[e_1 \cos(u_1 + \omega_1)$$
$$+ \cos 2u_1 + \frac{e_1}{3}\cos(3u_1 - \omega_1)\Big],$$
$$P_1 = \frac{4}{3} - 2\sin^2 i'' + \sin 2i_1 \sin 2i'' \cos(h' - \Omega_1)$$
$$+ \sin^2 i_1\{-2 + \sin^2 i''[3 + \cos 2(h' - \Omega_1)]\},$$
$$P_2 = 2\sin^2 i'' \cos 2(h' - \Omega_1)$$
$$- \sin 2i_1 \sin 2i'' \cos(h' - \Omega_1)$$
$$+ \sin^2 i_1\{2 - \sin^2 i''[3 + \cos 2(h' - \Omega_1)]\},$$
$$P_3 = 2\cos i_1 \sin^2 i'' \sin 2(h' - \Omega_1)$$
$$- 2\sin i_1 \sin 2i'' \sin(h' - \Omega_1),$$
$$Q_1 = \{[2\sin^2 i'' - \sin 2i_1 \sin 2i'' \cos(h' - \Omega_1)$$
$$+ \sin^2 i_1\langle -3\sin^2 i'' + (2 - \sin^2 i'')\cos 2(h' - \Omega_1)\rangle]$$
$$\times \cos 2g' + 2[\sin 2i_1 \sin i'' \sin(h' - \Omega_1)$$
$$- \sin^2 i_1 \cos i'' \sin 2(h' - \Omega_1)]\sin 2g'\},$$
$$Q_2 = \{[2(2 - \sin^2 i'')\cos 2(h' - \Omega_1)$$
$$+ \sin 2i_1 \sin 2i'' \cos(h' - \Omega_1) + \sin^2 i_1\langle 3\sin^2 i''$$
$$- (2 - \sin^2 i'')\cos 2(h' - \Omega_1)\rangle]\cos 2g'$$

$$+ 2[-2\cos i'' \sin 2(h' - \Omega_1)$$
$$- \sin 2i_1 \sin i'' \sin(h' - \Omega_1)$$
$$+ \sin^2 i_1 \cos i'' \sin 2(h' - \Omega_1)] \sin 2g'\},$$
$$Q_3 = \{2[\cos i_1 (2 - \sin^2 i'') \sin 2(h' - \Omega_1)$$
$$+ \sin i_1 \sin 2i'' \sin(h' - \Omega_1)] \cos 2g'$$
$$+ 4[\cos i_1 \cos i'' \cos 2(h' - \Omega_1)$$
$$+ \sin i_1 \sin i'' \cos(h' - \Omega_1)] \sin 2g'\}.$$

A BRIEF DESCRIPTION OF THE SEQUENCE OF CALCULATIONS AND METHODOLOGICAL PECULIARITIES

The main problem solved by the numerical–analytical method in question is to calculate the perturbed elements of a distant satellite orbit for the current time t. As the initial elements, we take the osculating Keplerian elements for a fixed initial time or epoch t_0. These orbital elements for recently discovered distant satellites are given in MPECs (Minor Planets Electronic Circulars) and are accessible via the Internet; their numerical values are gradually improved as new observations are accumulated. It is also clear that new planetary satellites, both near and distant, will be discovered in the future.

We can calculate the initial Delone osculating elements using formulas (1) and the initial mean Delone elements L_0'', l_0'', G_0'', g_0'', H_0'', η_0'' by iteratively and sequentially solving Eqs. (6) and (18). Since the evolution system is numerically integrated in the physically more meaningful Keplerian elements, the initial mean Keplerian elements a_0'', e_0'', i_0'', ω_0'', Ω_0'', M_0'' can be calculated using the formulas that are the inverse of (1), while all of the functions Φ_j^* in formulas (19), (20), (43), (47), (49) are expressed in terms of the mean Keplerian elements. Numerically integrating the evolution equations with the total perturbing function Φ^* for an arbitrary epoch t yields the mean elements $a''(t)$, $e''(t)$, $i''(t)$, $\omega''(t)$, $\Omega''(t)$, $M''(t)$. The current mean Delone elements can be calculated using (1). Subsequently, the oscillating Delone elements $L(t)$, $l(t)$, $G(t)$, $g(t)$, $H(t)$, $h(t)$ can be determined by iteratively solving first Eqs. (18) and then Eqs. (6). Finally, the osculating Keplerian elements for the current epoch t can be calculated using the formulas that are the inverse of (1).

With this brief description, we end the methodological part of our work. In our next article, we will use our method to study the orbital evolution of new distant satellites of the giant planets.

ACKNOWLEDGMENTS

The method was implemented in software mainly by N.M. Teslenko. I am grateful to him for his skillful help, which allowed inaccuracies in several derived formulas to be found and corrected and for the test calculations.

REFERENCES

1. J. Kovalevsky, Acad. Sci. **258** (18) (1964).
2. J. Kovalevsky, *IAU Symp. No. 25*, Ed. by G. I. Kontopoulos (Academ. Press, London, 1966), p. 326.
3. Y. Kozai, Astron. J. **67**, 591 (1962).
4. M. L. Lidov, Iskustvennye Sputniki Zemli **8**, 5 (1961).
5. M. L. Lidov, Tr. Inst. Teor. Atron. XVII **54** (1978).
6. A. A. Orlov, Byull. Inst. Teor. Atron. X **5** (118), 360 (1965a).
7. A. A. Orlov, *Proc. of XV Intern. Congress on Astronautics* (Gauthier-Villars, Paris, 1965b), Vol. 1.
8. A. A. Orlov, Vestn. Mosk. Univ., Fiz., Astron. **6**, 104 (1969).
9. A. A. Orlov, Byull. Inst. Teor. Atron. XII **2** (135), 195 (1970a).
10. A. A. Orlov, Byull. Inst. Teor. Atron. XII **3** (136), 302 (1970b).
11. A. A. Orlov, Tr. Gos. Astron. Inst. im P. K. Shternberga XLIII **2**, 30 (1972).
12. M. A. Vashkov'yak and N. M. Teslenko, Pis'ma Astron. Zh. **24**, 474 (1998) [Astron. Lett. **24**, 406 (1998)].

Translated by V. Astakhov

Astronomy Letters, Vol. 31, No. 1, 2005, pp. 7–14. Translated from Pis'ma v Astronomicheskiĭ Zhurnal, Vol. 31, No. 1, 2005, pp. 10–16.

The Luminosity Function of Low-Mass X-ray Binaries in Galaxies

K. A. Postnov* **and A. G. Kuranov****

Sternberg Astronomical Institute, Universitetskiĭ pr. 13, Moscow, 119992 Russia

Received June 8, 2004

Abstract—The X-ray luminosity function of low-mass binaries constructed from the observations of pointlike X-ray sources in galactic bulges can be explained in terms of the main evolutionary relations for the rate of mass transfer onto a compact object. The observed scatter of luminosities for individual low-mass X-ray sources in our Galaxy is shown to be satisfactorily described by a symmetric quasi-Lorentz curve with a dispersion proportional to the mean luminosity. Such a form of the mean luminosity function for individual sources does not affect the power-law pattern of the luminosity function for the entire population of sources that is expected for a power-law dependence of the mass transfer rate in a close binary on the mass of the Roche lobe–filling optical component. © *2005 Pleiades Publishing, Inc.*

Key words: *low-mass X-ray binaries, mass transfer, luminosity functions.*

INTRODUCTION

Measurements of the fluxes from pointlike X-ray sources in other galaxies by the Chandra and XMM-Newton space telescopes have initiated a new line of research on the processes of accretion onto compact stars in close binary systems. Simultaneous study of many sources from the same class at different evolutionary stages gives a deeper insight into their nature and the peculiarities of specific galaxies. Grimm *et al.* (2003) and Gilfanov (2004) have performed a comprehensive statistical analysis of the observed luminosity function for X-ray sources using Chandra and XMM data, constructed the individual X-ray luminosity functions (XLFs) for galaxies and the mean XLF, and discussed its astrophysical applications. We pointed out previously (Postnov 2003) that the universal power-law XLF, $dN/dL_X \sim L^{-1.6}$, derived by Grimm *et al.* (2003) over a wide luminosity range (10^{34}–10^{40} erg s^{-1}) can be naturally explained by the universal properties of the accretion from stellar wind in high-mass X-ray binaries (HMXBs) and by the power-law mass–luminosity and mass–radius relations for the donor components in these systems, early-type stars. The key point in our analysis was also the natural assumption about a power-law initial mass function of the stars (the Salpeter or Miller–Scalo laws). We also assumed that the rate of accretion onto the compact star, $\dot{M}_a$, is the main parameter that determines the X-ray luminosity of the system, $L_X \propto \dot{M}_a$.

New observational data allowed Gilfanov (2004) (see also Kim and Fabbiano 2004) to construct the XLF for low-mass X-ray sources. It turns out that the mean XLF for these sources also reduces to some universal form, which, however, is not described by a single power law as in case of HMXBs.

It is well known that variable and transient sources whose luminosities vary by several factors (or even much more, as in the case of X-ray novae) on various time scales are common among close X-ray binaries. The typical X-ray exposure times do not exceed several tens of kiloseconds, which in most cases is less than the time scale of noticeable luminosity variations in individual sources. Therefore, the question arises as to what determines the form of the mean XLF: the distribution of mean luminosities or the form of the luminosity function for individual sources.

In this paper, we show the following: (1) the observed scatter of X-ray luminosities for individual LMXBs in our Galaxy about the mean, as estimated from ASM/RXTE data, is generally described by a symmetric quasi-Lorentz distribution with a dispersion proportional to the mean flux; (2) this distribution of $\dot{M}_a$ does not affect the power-law form of the XLF determined theoretically by analyzing the mass transfer rates $\dot{M}_o$ in close binaries; (3) the average form of the XLF for LMXBs can be explained by evolutionary peculiarities of the mass transfer in LMXBs on the time scale of the removal of orbital angular momentum by gravitational radiation (the XLF part $\propto L_X^{-1}$, $L_X < 2 \times 10^{37}$ erg s^{-1}) and magnetic stellar wind (the XLF part $\propto L_X^{-2}$, $2 \times 10^{37} < L_X < 5 \times 10^{38}$ erg s^{-1}).

*E-mail: pk@sai.msu.ru
**E-mail: alex@xray.sai.msu.ru

1063-7737/05/3101-0007$26.00

Table 1. LMXBs with short orbital periods

No.	Source	$P(h)$	F_x	σ	$F_{\min}$	$F_{\max}$
1	V1333 Aql	18.97	2.31	7.85	−13.85	49.68
2	V821 Ara	14.86	6.80	13.51	−13.92	72.57
3	V1408 Aql	9.33	1.89	1.23	−17.07	6.95
4	LU TrA	9.14	1.01	1.06	−4.59	8.63
5	V691 CrA	5.57	1.18	1.33	−8.62	16.73
6	V926 Sco	4.65	12.89	3.38	−9.70	29.64
7	V2216 Oph	4.20	17.34	2.51	0.00	35.78
8	GR Mus	3.93	1.93	1.04	−6.02	23.36
9	V801 Ara	3.80	10.90	4.88	−5.63	34.92
10	1705−4402	1.31	11.67	8.85	−3.89	35.94

Note. The orbital period $P(h)$ (in hours), the mean flux F_X, the rms deviation of the flux σ, and the minimum ($F_{\min}$) and maximum ($F_{\max}$) fluxes for the entire observing period used in the statistics (1996–2003) are given for each source. The input data were taken from the ASM RXTE archive. The values of F_X and σ are in units of the ASM count rate.

POWER-LAW LUMINOSITY FUNCTIONS

First, let us show in the most general form how the power-law XLFs in accreting binary systems are obtained. The main assumption consists in the possibility of expressing the XLF of the source in terms of the mass transfer rate in the binary $\dot{M}_o$, which is a power-law function of the mass of the optical donor star M_o (Postnov 2003):

$$L_X \sim \dot{M}_a \sim \dot{M}_o \sim M_o^\alpha. \quad (1)$$

Below, for convenience, we consider the luminosity function per logarithmic interval, i.e., $dN/d\ln L_X$. In a stationary case, under assumption (1),

$$\frac{dN}{d\ln L_X} = \frac{dN}{d\ln M_o}\frac{d\ln M_o}{d\ln L_X} \propto L_X^{-\frac{\beta_{st}-1}{\alpha}}, \quad (2)$$

where the stationary mass function of the optical components is

$$f_{st}(M) \equiv \frac{dN}{dM_o dt} \sim M_o^{-\beta_{st}} \quad (3)$$

(e.g., $\beta_{st} = 2.35$ for the Salpeter distribution). Thus, we obtain the power-law XLF

$$\frac{dN}{d\ln L_X} \sim L_X^{-\Gamma},$$

in which the index

$$\Gamma = \frac{\beta_{st}-1}{\alpha}$$

depends only on the slope of the mass function and relation (1).

The Stationary Mass Function of the Optical Components

Two cases should be distinguished: young HMXBs, in which the mass of the optical component has changed only slightly since their formation, and old LMXBs, in which the mass of the optical star changes significantly during the mass transfer. In the former case, the mass function of the optical components differs only slightly from the initial function; therefore,

$$f_{st}(M) = f_o(M) \propto M^{-\beta}, \qquad \beta_{st} = \beta. \quad (4)$$

In the latter case, the stationary stellar mass distribution can be found from the solution of the one-dimensional kinetic equation with a stationary source $f_o(M)$

$$\frac{\partial}{\partial M}\left[f(M)\dot{M}\right] \propto f_o(M). \quad (5)$$

For $\dot{M} < 0$, we obtain

$$f_{st}(M) = \frac{\int_M^{M_{\max}} \dot{f}_0(M')dM'}{\dot{M}}, \quad (6)$$

where $M_{\max}$ is the upper limit for the stellar mass. Since the mass function has a power-law pattern, its exact value does not play a significant role.

Substituting the power-law mass function $f_o(M) \sim M^{-\beta}$ into (6) yields

$$f_{st}(M) \propto M^{-\beta+1-\alpha}, \quad (7)$$

i.e., the index in the stationary stellar mass distribution is

$$\beta_{st} = \beta - 1 + \alpha. \quad (8)$$

For instance, in the above case of HMXBs accreting from stellar wind, $\alpha \approx 2.5$ (Postnov 2003), and $\Gamma = 0.54$–0.6 (the observed value is ~ 0.6) for $\beta = 2.35$–2.5.

INFLUENCE OF THE LUMINOSITY FUNCTION FOR INDIVIDUAL SOURCES ON THE FORM OF THE LUMINOSITY FUNCTION FOR A POPULATION

Before considering the more complex case of LMXBs, let us discuss the influence of the individual XLF for a source on the form of the total XLF for the entire population. Let the rate of accretion onto the compact object and, hence, the X-ray luminosity L_X change in accordance with the distribution $F(x)$ (in

this case, the mean mass transfer rate $\dot{M}_0$ can either also change or remain constant). Denote the X-ray luminosity corresponding to the mean accretion rate by L_0 and assume that the mean accretion rate reflects the mass transfer rate in the system determined by its evolutionary status. It is easy to see that the observed XLF is expressed by the convolution

$$dN/dL_X = \frac{\int_{L_{min}}^{L_{max}} (dN/dL_0)F(L_X - L_0)dL_0}{\int_{L_{min}}^{L_{max}} F(L_X - L_0)dL_0}. \quad (9)$$

We will use the class of power-law XLFs, i.e., assume that $dN/d\ln L_0 \sim L_0^{-\Gamma}$. If the function $F(x-y)$ is factorized as

$$F(x-y) = F_1(y)F_2(x/y-1), \quad (10)$$

then the power-law luminosity function for the population of sources, $dN/d\ln x \sim x^{-\Gamma}$, does not change its power-law pattern when $F_1(y)$ is also a power-law function for any form of the function F_2 (all of the required integration properties are assumed). To prove this, it will suffice to go to a new variable, $t = x/y - 1$, in the integrals of (9) and to let $L_{min} \to 0$, $L_{max} \to \infty$.

To determine the form of the function $F(L_X - L_0)$ for LMXBs, we use ASM RXTE data. Let us first consider LMXBs with known orbital periods shorter than 20 h and mean fluxes higher than 1 count s^{-1} (Table 1). Orbital periods shorter than 20 h correspond to a low mass of a Roche lobe–filling star ($\sim 2M_\odot$ for main sequence stars of normal chemical composition). In this case, mass is transferred through the removal of orbital angular momentum by magnetic stellar wind or (for systems with periods shorter than several hours) by gravitational radiation (see below). For each source, Table 1 gives the mean fluxes F_X (averaged over several years of observations, $\sim 10^3$–10^4 points for each source) and the rms deviation σ from F_X. The values of F_X and σ are in units of the ASM detector count rate (for comparison, the flux from the Crab Nebula is 75 ASM counts s^{-1}). Figure 1 shows the individual normalized XLFs for the sources from Table 1 and the corresponding orbital periods. Figure 2 shows the mean XLF for these systems (histogram) and its quasi-Lorentz fit $F(x-y) = \frac{a}{(x-y)^2+by^2}$ ($a, b = \text{const}$), which obviously satisfies condition (10). As the errors in each bin, we took the dispersion

$$\sigma_i = \sqrt{\sum_{j=1}^{n_i}(x_j - \bar{x})/n_i},$$

where n_i is the number of points in bin i, and $\bar{x}$ is the mean value. The formal significance level of the fit according to the χ^2 test for 17 degrees of freedom is $P(\chi^2_{17} \geq 8.3)$ is ≈ 0.96.

Since, as we see from Table 1, almost all of the fluxes from the sources with known orbital periods are, on average, weak for ASM, the form of the individual XLF (particularly its left wing) can be determined with large errors. Therefore, for an additional check, we considered a sample of bright low-mass X-ray sources whose orbital periods can be arbitrary or unknown (Table 2). The XLF of X-ray sources determined by nonstationary disk accretion onto a compact star does not depend significantly on the orbital period (the outer disk radius a is $\propto P^{2/3}$), but is determined to a greater extent by the mass of the compact star and its nature (a neutron star or a black hole). In our case, most of the sources contain neutron stars with approximately equal masses. The individual XLFs for the bright low-mass galactic sources from Table 2 are shown in Fig. 3. The mean XLF for these sources is shown in Fig. 4 (histogram). It is well fitted by a Lorentz curve (the significance level is $P(\chi^2_{17} \geq 8.8) \approx 0.94$).

In Fig. 5, the dispersion of the observed XLF for the bright sources from Table 2 is plotted against the mean luminosity. The proportionality of the dispersion to the mean flux is preserved when the flux changes by more than an order of magnitude.

THE X-RAY LUMINOSITY FUNCTION OF LMXBs

An analysis of the observations of pointlike sources in the bulges of galaxies reveals a power-law XLF for LMXBs (Gilfanov 2004; Kim and Fabbiano 2004) $dN/d\ln L_X \sim L_X^{-\Gamma}$ with the index

$$\Gamma \sim \begin{cases} \sim 0, & L_X < 2\times 10^{37}\ \text{erg s}^{-1} \\ -0.9\ldots -1.1, & 2\times 10^{37} < L_X < 5\times 10^{38}\ \text{erg s}^{-1} \\ -5, & L_X > 5\times 10^{38}\ \text{erg s}^{-1}. \end{cases} \quad (11)$$

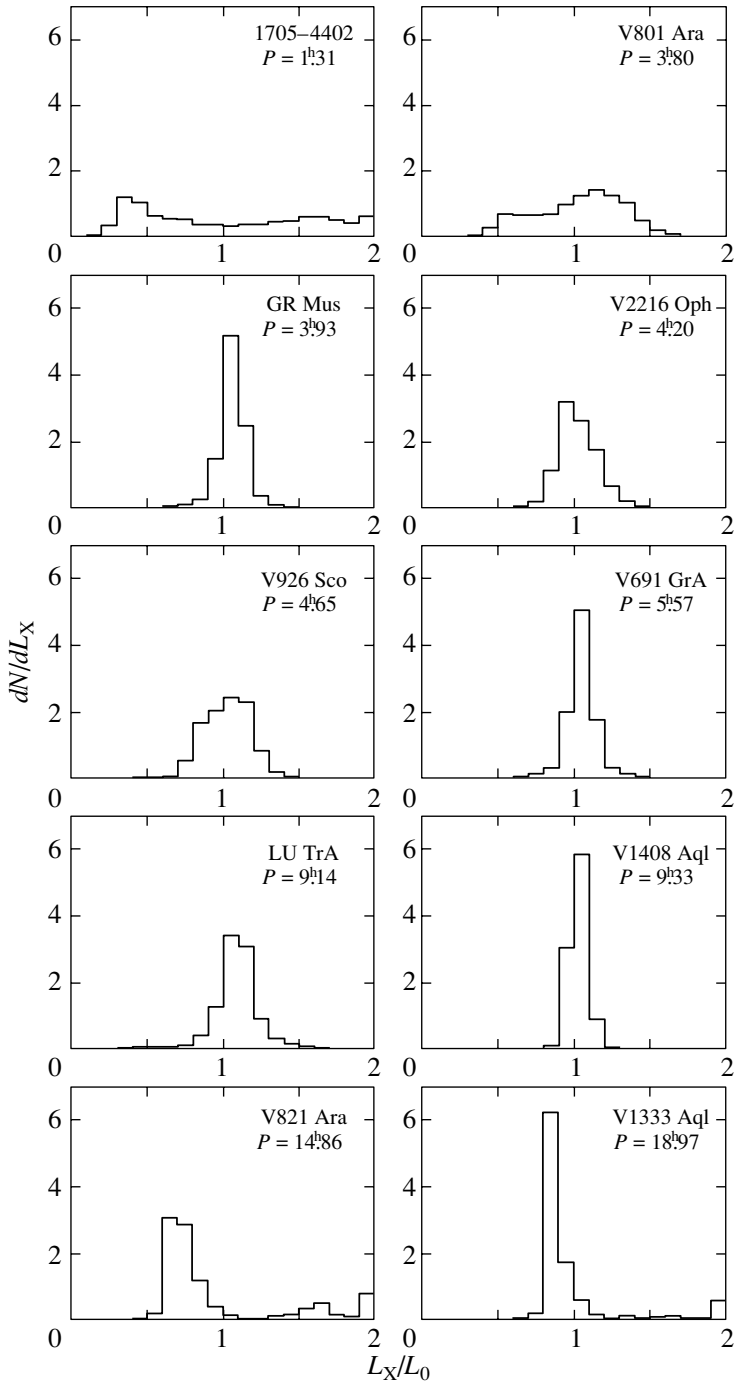

Fig. 1. XLF for LMXBs from Table 1 (with known orbital periods shorter than 20 h based on ASM RXTE data). The luminosity of each source is in units of the mean luminosity L_0. All distributions were normalized in such a way that $\int \frac{dN}{dL_X} dL_X = 1$.

Let us show that the power-law form of the XLF for systems with orbital periods shorter than ~20 h can be produced by the main evolutionary factors that determine the mass transfer rate in LMXBs: magnetized stellar wind (MSW) and gravitational radiation (GR).

Magnetized Stellar Wind

Denote the masses of the optical and compact stars by M_o and M_X respectively, the mass ratio of the components by $q = M_o/M_X$, and the semimajor axis of the binary system by a (the orbit is assumed to be circular). The time scale of the removal of orbital

angular momentum by MSW is commonly calculated using an empirical Skumanich law for the spindown of solar-type main sequence stars (for more details, see the discussion by Masevich and Tutukov (1988) and van den Heuvel (1992)) is

$$\tau_{\rm msw} \sim \frac{a^5 M_{\rm X}}{(M_{\rm X}+M_{\rm o})^2 M_{\rm o}^4}. \quad (12)$$

Since the mass transfer in LMXBs takes place when the optical star fills its Roche lobe, we can write

$$R_{\rm o} = a f(q), \quad (13)$$

where

$$f(q) \approx \left(\frac{q}{1+q}\right)^{1/3}, \qquad q < 0.5.$$

Then,

$$L_0 \sim \dot{M}_{\rm o} \sim \frac{M_{\rm o}}{\tau_{\rm msw}} \sim \frac{M_{\rm o}^5 M_{\rm X}(1+q)^2 f(q)^5}{R_{\rm o}^5}.$$

Given $R_{\rm o} \sim M_{\rm o}^{0.9...1}$ for late-type main sequence stars, we obtain

$$L_{\rm X} \sim M_{\rm o}^{2.17...2.67}, \qquad \alpha \approx 2.17 \ldots 2.67.$$

Substituting this value into (8) yields $\beta_{\rm st} \approx 3.52 \ldots 4$ for the Salpeter initial mass function and, finally,

$$\frac{dN}{d\ln L_0} \sim L_0^{-1.6...-1.13}, \quad \Gamma_{\rm msw} \sim 1.6 \ldots 1.13. \quad (14)$$

Gravitational Radiation

In the dipole approximation, the time scale of change in the orbital parameters of a binary system due to GR is

$$\tau_{\rm gr} \sim \frac{a^4}{(M_{\rm X}+M_{\rm o})M_{\rm o}M_{\rm X}}. \quad (15)$$

Using the condition for the Roche lobe filling $a = R_{\rm o}/f(q)$, we obtain

$$L_0 \sim \dot{M}_{\rm o} \sim \frac{M_{\rm o}}{\tau_{\rm gr}} \sim \frac{M_{\rm o}^2 M_{\rm X}^2 (1+q) f(q)^4}{R_{\rm o}^4}.$$

For $R_0 \sim M_{\rm o}^{0.9}$, we find that

$$L_0 \sim M_{\rm o}^{-0.27...-0.3}, \qquad \alpha \approx -0.27 \ldots -0.3.$$

Substituting, as in the case of MSW, this value into (8) yields $\beta_{\rm st} \approx 1.05 \ldots 1.08$ and, finally, we obtain

$$\frac{dN}{d\ln L_0} \sim L_0^{-0.16...0.3}, \qquad \Gamma_{\rm gr} \sim 0.16 \ldots 0.3. \quad (16)$$

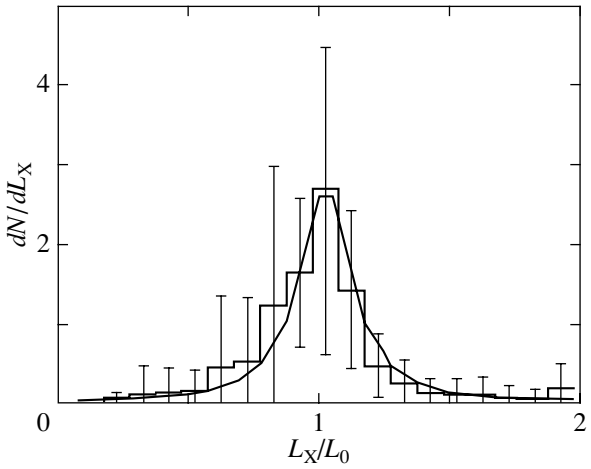

Fig. 2. Mean XLF for low-mass X-ray sources (histogram). The solid line indicates a Lorentz fit. The significance level $P(\chi^2_{17} \geq 8.3)$ is ≈ 0.96.

A Break in the Mean XLF for LMXBs

The break in the mean XLF for LMXBs is observed at a luminosity of $\sim 2 \times 10^{37}$ erg s^{-1}, which corresponds to a rate of accretion onto a neutron star $\dot{M} \sim 10^{-9} M_\odot$/year. In our interpretation, the break corresponds to the passage from the MSW transfer time scale to the GR scale. We determine the stellar

Table 2. Bright LMXBs

No.	Source	$F_{\rm X}$	σ
1	Cyg X2	37.22	8.32
2	Sco X1	880.995	114.68
3	GX 9+9	17.22	2.42
4	GX 9+1	39.24	4.57
5	GX 5−1	70.75	9.53
6	GX 3+1	22.34	5.99
7	GX 17+2	44.86	5.33
8	GX 13+1	22.45	2.93
9	GX 340+0	29.39	4.34
10	GX 349+2	51.40	12.19
11	V926 Sco	12.89	3.38
12	V2216 Oph	17.34	2.51
13	V801 Ara	10.90	4.88
14	1705−4402	11.67	8.85

Note. The mean flux $F_{\rm X}$ and the rms deviation σ in units of the ASM count rate are given for each source.

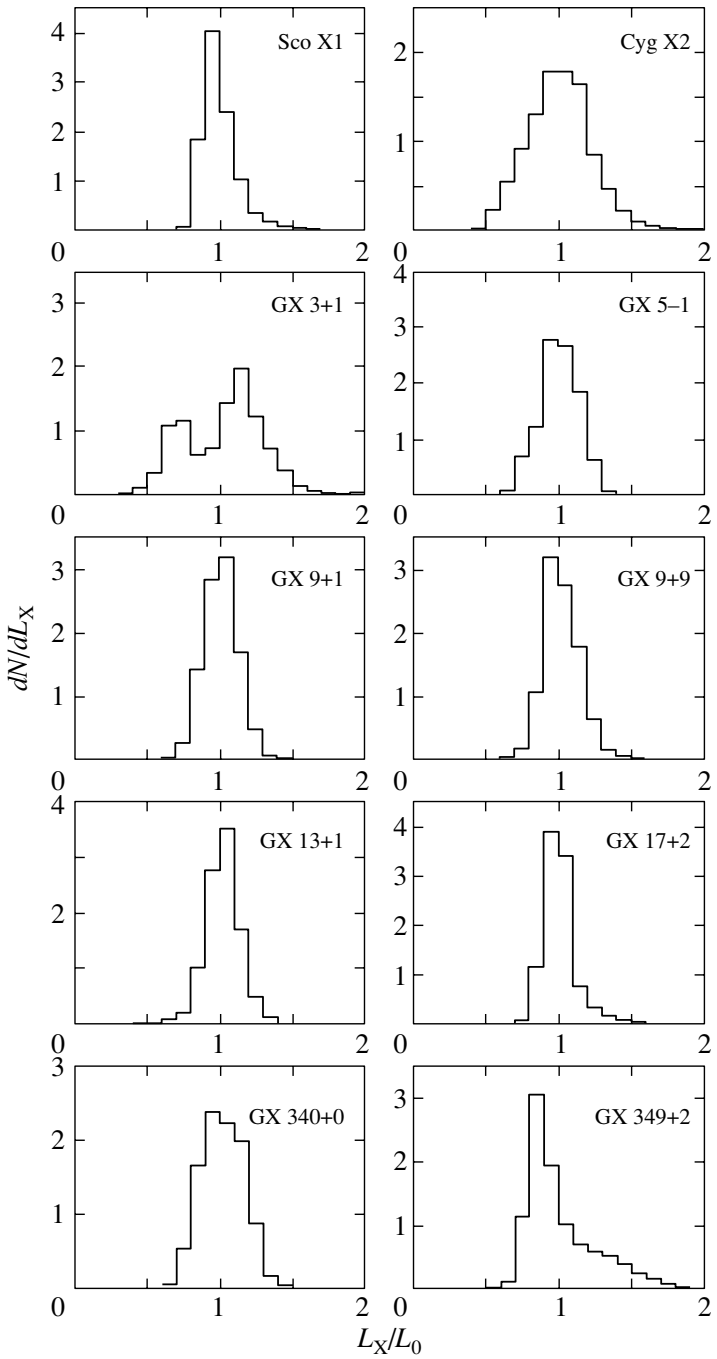

Fig. 3. Same as Fig. 1 for bright LMXBs from Table 2.

mass from the condition $\tau_{\rm msw} = \tau_{\rm gr}$:

$$M_{\rm o} \approx 0.4 M_\odot,$$

which is close to the universally accepted value of $\sim 0.3 M_\odot$ (Spruit and Ritter 1983). At such masses of the optical stars, the transfer rate is

$$\dot{M}(0.4 M_\odot) \sim 3 \times 10^{-10} M_\odot \ {\rm yr}^{-1}$$

(see, e.g., Rappaport *et al.* (1984) and more recent evolution calculations), which is generally consistent with our hypothesis.

DISCUSSION AND CONCLUSIONS

The above analysis leads us to conclude that the observed XLF for LMXBs can generally be explained by the accretion of matter onto a neutron star with

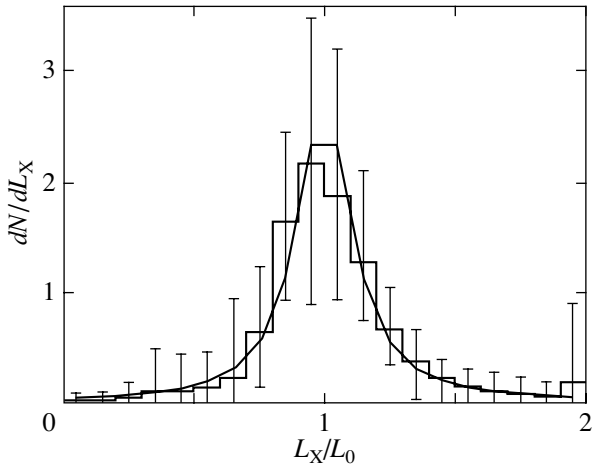

Fig. 4. Mean XLF for 14 low-mass bright X-ray sources from Table 2 (histogram). The solid line indicates a Lorentz fit. The significance level $P(\chi^2_{17} \geq 8.8)$ is ≈ 0.94.

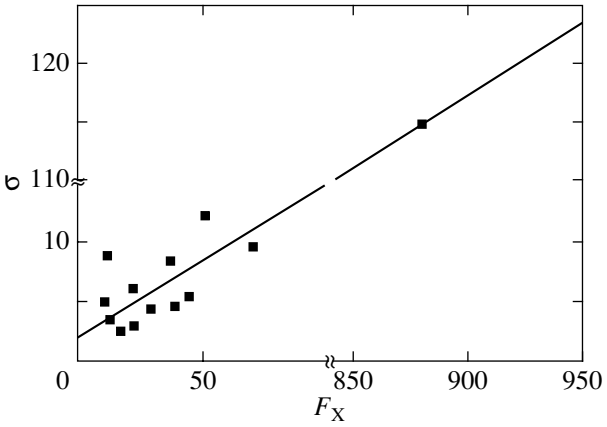

Fig. 5. Dispersion of the X-ray flux σ versus mean flux F_X for 14 bright LMXBs based on ASM RXTE. The solid line represents a linear fit.

the Roche lobe filling driven by the removal of angular momentum through gravitational radiation (up to $L_X \sim 2 \times 10^{37}$ erg s^{-1}) and magnetic stellar wind ($L_X > 2 \times 10^{37}$ erg s^{-1}). These mechanisms, which determine the mass transfer rate in systems with orbital periods shorter than 15–20 h, lead to different power-law dependences of $\dot{M}_o$ on the mass of the optical component M_o; this is a necessary condition for obtaining a power-law luminosity function for the population of sources. For low-mass systems with long orbital periods, the Roche lobe is filled by a subgiant star. Based on an analysis of the mass transfer in such systems (Yungelson and Livio 1998), it can be shown that a power-law dependence of the mass transfer rate on the mass of the optical star is also obtained in systems with subgiants. In addition, a considerable fraction of LMXBs reside in globular clusters or were born in globular clusters through tidal captures of stars. The evolution of such systems is more complex. This necessitates using different approaches to analyzing the XLF for low-mass sources. It seems that the population synthesis method can be more accurate for a quantitative description of the XLF.

The contribution from ultracompact close binaries that are dynamically formed in globular clusters (of X 1820–30 type) to the XLF for low-mass close binaries was considered by Bildsten and Deloye (2004). In such close binaries, the Roche lobe is filled by a degenerate, low-mass white dwarf with an inverse mass–radius relation, and mass is transferred through GR. An analysis indicates (Bildsten and Deloye 2004) that the XLF for the population of such systems can also account for the observed XLF slope in the range of X-ray luminosities $6 \times 10^{37} < L_X < 5 \times 10^{38}$ erg s^{-1}.

Our analysis shows that the mean X-ray luminosity function for individual sources as obtained from ASM RXTE data is satisfactorily described by a symmetric quasi-Lorentz distribution with a dispersion proportional to the mean luminosity. This pattern of the mean individual XLF does not affect the power-law form of the XLF for the entire population of sources, which is determined by the dependence of the mean X-ray luminosity of each source on the mass of the optical Roche-lobe-filling donor star.

We emphasize that precisely the possibility of representing the mean XLF for low-mass sources by a single law preserves the power-law form of the distribution that is derived from the analysis of the evolutionary peculiarities of the mass transfer in LMXBs. The slopes of the XLFs for individual galaxies (Kim and Fabbiano 2004) slightly differ; the power-law pattern of the XLF is obtained by averaging over many galaxies. This reflects the individual peculiarities of the evolution and the XLF of sources in different galaxies.

ACKNOWLEDGMENTS

We wish to thank M.R. Gilfanov and A.A. Vikhlinin for their useful discussions and L.R. Yungelson for his helpful remarks. This work was supported in part by the Russian Foundation for Basic Research (projects no. 04-02-16720 and 03-02-16110). We used data retrieved from the High Energy Astrophysics Archive (HEASARC) of the Goddard Space Flight Center (GSFC).

REFERENCES

1. L. Bildsten and C. J. Deloye, astro-ph/0404234 (2004).
2. H.-J. Grimm, M. R. Gilfanov, and R. A. Sunyaev, Mon. Not. R. Astron. Soc. **339**, 793 (2003).
3. M. R. Gulfanov, Mon. Not. R. Astron. Soc. **349**, 146 (2004).
4. E. P. J. van den Heuvel, *Interacting Binaries* (Springer-Verlag, Berlin, 1992).
5. D.-W. Kim and G. Fabbiano, submitted to Astrophys. J. (2004); astro-ph/0312104.
6. A. G. Masevich and A. V. Tutukov, *Stellar Evolution. Theory and Observations* (Nauka, Moscow, 1988) [in Russian].
7. K. A. Postnov, Pis'ma Astron. Zh. **29**, 424 (2003) [Astron. Lett. **29**, 372 (2003)].
8. S. A. Rappaport, F. Verbunt, and P. C. Joss, Astrophys. J. **275**, 713 (1983).
9. H. C. Spruit and H. Ritter, Astron. Astrophys. **124**, 267 (1983).
10. L. R. Yungelson and M. Livio, Astrophys. J. **497**, 168 (1998).

Translated by G. Rudnitskiĭ